



Deliverable 8.11: Identification and analysis of potential accident scenarios in an interim storage and/or packaging facility and assessment of fuel performance

Work Package 8

The project leading to this application has received funding from the European Union's Horizon 2020 research and innovation programme under grant agreement No 847593.



EURAD Deliverable 8.11 – Identification and analysis of potential accident scenarios in an interim storage and/or packaging facility and assessment of fuel performance.

Document information

Project Acronym	EURAD
Project Title	European Joint Programme on Radioactive Waste Management
Project Type	European Joint Programme (EJP)
EC grant agreement No.	847593
Project starting / end date	1st June 2019 – 30 May 2024
Work Package No.	8
Work Package Title	Spent Fuel Characterization and Evolution until Disposal
Work Package Acronym	SFC
Deliverable No.	8.11
Deliverable Title	Identification and analysis of potential accident scenarios in an interim storage and/or packaging facility and assessment of fuel performance.
Lead Beneficiary	Nagra
Contractual Delivery Date	May 2024
Actual Delivery Date	12th June 2024
Type	Report
Dissemination level	PU
Authors	Efstathios Vlassopoulos (Nagra), Alifieris Olympios (Nagra), Michail Hadjigeorgiou (Nagra), Michele Bellotti (Nagra), Pauline Fouquet-Metivier (CEA), Stéphane Reboul (CEA), Doris Drouan (CEA), Thierry Blay (CEA), Isabelle Zacharie-Aubrun (CEA), Catherine Sabathier-Devals (CEA), Luis Enrique Herranz Puebla (CIEMAT), Francisco Feria Marquez (CIEMAT), Carlos Aguado Basabe (CIEMAT), Carlos Pérez Goicoechea (IDOM), Celia González Lavid (IDOM), Iñaki Gorrochategui Sánchez (IDOM)

To be cited as:

E. Vlassopoulos, C. A. Basabe, M. Bellotti, T. Blay, D. Drouan, P. Fouquet-Metivier, C. P. Goicoechea, M. Hadjigeorgiou, C. G. Lavid, F. F. Marquez, A. Olympios, L. E. H. Puebla, S. Reboul, C. Sabathier-Devals, I. G. Sánchez, I. Zacharie-Aubrun (2024): Identification and analysis of potential accident scenarios in an interim storage and/or packaging facility and assessment of fuel performance. Final version as of 12.06.2024 of deliverable D8.11 of the HORIZON 2020 project EURAD. EC Grant agreement no: 847593.

Disclaimer

All information in this document is provided "as is" and no guarantee or warranty is given that the information is fit for any particular purpose. The user, therefore, uses the information at its sole risk and liability. For the avoidance of all doubts, the European Commission has no liability in respect of this document, which is merely representing the authors' view.

Acknowledgement

This document is a deliverable of the European Joint Programme on Radioactive Waste Management (EURAD). EURAD has received funding from the European Union's Horizon 2020 research and innovation programme under grant agreement No 847593.

Status of deliverable		
	By	Date
Delivered (Lead Beneficiary)	Nagra	31/05/2024
Verified (WP Leader)	SKB	31/05/2024
Approved (PMO)	P. Carbol	11/06/2024
Submitted to EC (Coordinator)	Andra	

Executive Summary

This report, titled "Identification and Analysis of Potential Accident Scenarios in an Interim Storage and/or Packaging Facility and Assessment of Fuel Performance," is a deliverable of the European Joint Programme on Radioactive Waste Management (EURAD) under Work Package (WP) 8 (Spent Fuel Characterisation and Evolution until Disposal). The work aims to enhance methodologies and understanding for the safe handling, storage, and disposal of radioactive waste. The studies build upon the relevant work and progress made within Tasks 2 and 3 of WP 8, related to fuel properties characterisation and related uncertainty analysis, as well as on the behaviour of nuclear fuel and cladding after discharge from reactor. Various data generated either through numerical or experimental investigations are used to better characterise the fuel/cladding properties and the end-of-life conditions, but also their evolution during dry storage conditions.

The analysis within this report identifies and evaluates various potential accident scenarios in interim storage and packaging facilities. The findings indicate that the most critical accident scenario is the dry storage system (DSS) tip-over, which poses significant risks to both the DSS and the spent nuclear fuel (SNF). The mechanical and thermal effects on fuel performance were assessed, revealing that cladding failure and structural deformation are primary concerns in severe accidents.

Finite Element Analysis (FEA) studies on Pressurized Water Reactor (PWR) spent fuel assemblies were conducted to model the mechanical performance under accident scenarios. The transition from small-scale rod models to full-scale spent fuel assembly models demonstrated the need for computationally efficient models to accurately predict fuel rod failure criteria.

Furthermore, a probabilistic methodology integrating FRAPCON-xt, HYDCLAD, and DAKOTA was developed to estimate the likelihood of fuel rod failure. Monte Carlo simulations highlighted the robust performance of SNF storage and transport systems and identified further research needs in modelling irradiation damage recovery. Additionally, oxidation tests at 200°C on irradiated fuel sections showed cladding rupture due to internal stress without the formation of U_3O_8 , suggesting gas release and swelling as failure mechanisms.

This work is integral to the broader objective of ensuring the safety and regulatory compliance of SNF storage solutions. By identifying and analysing potential accident scenarios, the findings contribute to the development of more resilient storage and packaging systems. The methodologies and models developed herein can be applied to assess and mitigate risks associated with SNF management, ultimately enhancing the safety protocols. This aligns with EURAD's mission to improve radioactive waste management strategies, ensuring long-term environmental protection and public safety.

Table of content

Executive Summary	4
Table of content	5
List of figures	8
List of Tables	12
Glossary.....	13
1. Introduction	14
2. Identification and risk assessment of accident scenarios	16
2.1 Introduction and background	16
2.2 Objective	16
2.3 Scope	16
2.4 Methodology.....	17
2.4.1 Impact on the DSS.....	17
2.4.2 Impact on the fuel	19
2.5 Accident analysis	20
2.5.1 Dry Storage System Tip-Over.....	20
2.5.2 Dry Storage System Drop	23
2.5.3 Fire.....	27
2.5.4 Explosion (External Overpressure).....	29
2.5.5 Lightning	30
2.5.6 Object Impact.....	30
2.5.7 Flooding	35
2.5.8 Burial under Debris	36
2.5.9 Extreme Temperature Changes	37
2.5.10 Supplemental Cooling System Failure	38
2.5.11 Blockage of Air Inlets	39
2.6 Summary of accidents and results.....	41
2.7 References.....	43
3. Study of the mechanical performance of PWR SFA in accident scenarios with Finite Element Analysis	44
3.1 From small scale rodlet models to full scale spent fuel assemblies	44
3.1.1 Abstract.....	44
3.1.2 Introduction	44
3.1.3 Modelling approaches and optimal simplified model selection.....	45

3.1.4	Derivation of failure criteria	49
3.1.5	Transition to larger scale assemblies	51
3.1.6	Full-scale model – Challenges and analysis results	60
3.1.7	Conclusion and outlook	65
3.2	References	66
4.	Development of a stochastic approach to determine probability of fuel rod cladding failure under accident scenarios	67
4.1	Introduction	67
4.2	Methodology	67
4.2.1	Approach	67
4.2.2	Cladding mechanical properties	68
4.2.3	Failure criteria	71
4.2.4	Statistical analysis	72
4.3	Application	73
4.3.1	Base Case	73
4.3.2	Scoping calculations	74
4.4	Final remarks	77
4.5	References	78
5.	Oxidation under air at 200 °C of irradiated fuel sections at high burn-up: destructive examinations (metallography, SEM, TEM) of UOX section with Zy-4 cladding ruptured after 13,630 hours of heating 80	
5.1	Introduction	80
5.2	Principles of the experiment and sample description	81
5.2.1	Principles of the experiment	81
5.2.2	Kinetic results and visual observations	81
5.2.3	Characteristics of the section of interest	82
5.3	Optical observations	83
5.3.1	Cladding	83
5.3.2	Fuel	84
5.4	SEM observations	86
5.4.1	2D	86
5.4.2	3D	89
5.4.3	Samples preparation for TEM analyses	96
5.5	TEM observations	97
5.5.1	Lamella 1 (restructured area)	97

5.5.2	Lamella 2 (non-restructured area)	99
5.5.3	Comparison between restructured and non-restructured areas	102
5.6	Conclusion	102
5.7	References	104
6.	Conclusions	105
6.1	Key findings	105
6.2	Recommendations and future work	105

List of figures

Figure 1 – MPC + Overpack / Bare Fuel Cask DSS examples from NUREG -2214 (NRC, 2019).....	17
Figure 2 – Accident Severity Chart.....	42
Figure 3 – The three different 1D models evaluated to determine which best corresponds to the mechanical data of three-point bending tests and has lower computational requirements. a) Model with annular cylindrical cross-section elements and cladding geometrical properties, b) Model with cylindrical cross-section elements and diameter equal to the cladding outer diameter, c) Model with annular cylindrical cross-section elements representing the cladding and cylindrical cross section elements representing the pellets placed inside the cladding.	45
Figure 4 – Example of a MOP produced during the optimisation process. The error of each simulation is plotted against the most important parameters of the optimisation process (in this case σ_0 and R_{inf}). The best fit of each parameter corresponds to the simulation with the lowest error value.	47
Figure 5 – Comparison between experimental force-displacement curves and best-fit curves of the 1D beam models, as derived from the optimisation process. a) Annular cylinder model, b) Cylinder model, c) Combined model.	48
Figure 6 – Comparison of normalised stress (left) and strain (right) values at yield and at failure for different BU values.	50
Figure 7 – Overview of basic components of a PWR fuel assembly. Original received from Encyclopaedia Britannica, Inc. [6].	52
Figure 8 – Shape of spacer grid springs and dimples on an actual cladding (left: 3D view, right: lengthwise cross-section).	53
Figure 9 – Spring and dimple configuration of developed FEMs.	53
Figure 10 – Force-displacement curves describing the behaviour of springs (left side) and dimples (right side). This data is based on the report of Adkins et al. [7] and is used in the current FEM.	53
Figure 11 – Assembly consisting of four beams with an annular cylinder cross-section and a 2x2 spacer grid modelled using shell elements.	54
Figure 12 – FEM of a 5x5 spacer grid consisting of beam elements with a rectangular profile and 25 fuel rods consisting of beam elements with an annular cylinder profile. On the left side is the model with cross-sections visible whereas on the right side is the same model with cross-sections turned-off....	55
Figure 13 – Full and half-symmetric 3x3 model. The model contains all the basic components of a fuel assembly.....	56
Figure 14 – Force-displacement behaviour of the model in the case of linear spring definition (black points - “BC” curve) and non-linear spring definition (red points – “Snippet” curve).	57
Figure 15 – FEM of a 15x15 spent-fuel sub-assembly. The model consists of 205 fuel rods, 20 guide tubes, 4 spacer grids and 1 top and bottom end piece respectively.	58
Figure 16 – Deformed shape of 15x15 FEM of a spent-fuel sub-assembly under two different bending loads applied at the top end piece. On the right-hand side an obstacle (zero displacement constraint) is positioned at 1/3rd of the distance between the first and second spacer grids. The un-deformed shape of the model can also be seen in each case. The colour scale corresponds to the displacement of each model component.	59

Figure 17 – Deformed shape of fuel rods of a 15x15 FEM of a spent-fuel sub-assembly under two different bending loads applied at the top end piece. On the right-hand side an obstacle (zero displacement constraint) is positioned at 1/3rd of the distance between the first and second spacer grids whereas in the left-hand side there is no obstacle. The colour scale refers to the principal total strain, although strain results are preliminary. The maximum strain location is depicted using a red label. ... 59

Figure 18 – Full-scale FEM of a PWR spent fuel assembly. The model consists of 8 spacer grids 205 fuel rods, 20 guide tubes and 1 top and bottom end piece respectively. 60

Figure 19 – Comparison between the deformed and un-deformed shape of the full-scale model. The colour scale corresponds to the displacement on the different components of the assembly. Red corresponds to higher displacement values whereas dark blue to lower. 61

Figure 20 – Number of fuel rods that have exceeded their yield stress value based on the applied displacement. 62

Figure 21 – 15x15 grid showing the principal plastic strain of each beam of the full-scale model for the loading scenario described in section 5.2. The values of the plastic strain are normalised using the maximum observed plastic strain on fuel rods. Therefore, the guide tubes, which exceed this maximum strain value, appear as completely black in the current representation. The layout of the assembly matches that of Figure 20. 63

Figure 22 – Shear force and bending moment diagram along the length of the beam at position (1, 1), at the last converged time step of the simulation. The right vertical axis corresponds to the bending moment whereas the left vertical axis corresponds to the shear force. The 0 position of the rod is specified at the side of the fuel assembly where no loading is applied. 64

Figure 23 – Side view of the full-scale model showing the developed stress on fuel rods and spacer grids at the maximum modelled displacement. Blue colour corresponds to lower stresses whereas red colour corresponds higher stresses. The guide tubes and top nozzle are hidden but their effects have nevertheless been considered in these results. 64

Figure 24 – General diagram of the methodology. 68

Figure 25 – Yield stresses vs. burnup (at EOL and room temperature). 70

Figure 26 – Comparison of the strain limits between FRAPCON and data provided from the project. 70

Figure 27 – Failure criteria. 71

Figure 28 – Statistical approach scheme. 72

Figure 29 – Variability in lineal power history [15]. 73

Figure 30 – Cladding hoop stress at dry storage onset (left) and yield stress at the moment of the accident (right); red lines represent the ductile-to-brittle threshold set (left) and the accident maximum stress applied (right). 74

Figure 31 – Cladding hoop stresses at the dry storage onset. Predictions with FRAPCON-xt (MASSIH) and FRAPCON-xt* (calibrated FRAPFGR). 75

Figure 32 – Yield stress at the accident. Predictions with FRAPCON-xt*, and with no annealing and full annealing. 76

Figure 33 – Model-to-data comparison for fast neutron fluence (left) and yield stress (right) evolution with irradiation damage annealing at 360 °C. Data from [20]. 76

Figure 34 – Yield stresses obtained with FRAPCON-xt* at room temperature and with the interpolation of the experimental results with the burnup. 77

<i>Figure 35 – (a) Oven used for long term oxidation cells, consisting of 12 cylindrical cells in a copper block and (b) example of a container, both used in the hot cell.</i>	<i>81</i>
<i>Figure 36 – Weight gain of UOx sections as a function of time.</i>	<i>82</i>
<i>Figure 37 – Section of interest section after 8140 and 13630 h of oxidation test under air at 200 °C [5].</i>	<i>82</i>
<i>Figure 38 – Sample’s section after 13630 h of oxidation test at 200 °C under air, with (d) and (e) the cladding section and fragments selected for observations.</i>	<i>83</i>
<i>Figure 39 – Optical observation of the cladding segment and positions of the detailed areas.</i>	<i>83</i>
<i>Figure 40 – Optical observations of the cladding (green and pink) and selected areas of crack (red), external zirconia (orange) and pellet/cladding interface (blue).</i>	<i>84</i>
<i>Figure 41 – Positions of the selected fragments and areas observed by optical microscopy.</i>	<i>85</i>
<i>Figure 42 – Detailed areas of Fragment (a) from 0.99R to 0.33R.</i>	<i>85</i>
<i>Figure 43 – SEM observations of different sections of the cladding segment.</i>	<i>86</i>
<i>Figure 44 – SEM observations of different areas of fuel/cladding interface.</i>	<i>87</i>
<i>Figure 45 – SEM observations of Fragment (c) at 0.96R, 0.83R, 0.58R, 0.40R and 0.23R.</i>	<i>88</i>
<i>Figure 46 – Images at 0.2R extracted from a 3D acquisition (step of 750 nm between each image, one image out of 50).</i>	<i>89</i>
<i>Figure 47 – SEM observation at 0.2R taken during a 3D acquisition, revealing the presence of precipitates, intragranular and intergranular bubbles and subdivided grains.</i>	<i>90</i>
<i>Figure 48 – 3D reconstruction of the (a) total porosity, (b) the intra- and (c) intergranular bubbles in the area studied at 0.2R.</i>	<i>91</i>
<i>Figure 49 – (a) Front view of an intragranular bubble, (b) top view, (c) series of images used for the 3D reconstruction (1 image every 15 nm) and (d) 3D reconstruction of the pore.</i>	<i>92</i>
<i>Figure 50 – (a) Front view of an intragranular bubble, series of images used for the 3D reconstruction (1 image every 15 nm) of the pore of interest, (b) top view and (c) 3D reconstruction of the pore.</i>	<i>93</i>
<i>Figure 51 – Images at 0.8R extracted from a 3D acquisition (step of 750 nm between each image, one image out of 50).</i>	<i>94</i>
<i>Figure 52 – SEM observation at 0.8R taken during a 3D acquisition, revealing the presence of precipitates, intragranular and intergranular bubbles and subdivided grains.</i>	<i>94</i>
<i>Figure 53 – 3D reconstruction of the (a) total porosity, (b) intra- and (c) intergranular bubbles in the area studied at 0.8R.</i>	<i>95</i>
<i>Figure 54 – Series of images and 3D reconstructions of one type of intragranular bubbles (sphere and dendrites, in blue) and precipitates of metal fission products (green).</i>	<i>96</i>
<i>Figure 55 – Series of images and 3D reconstructions of two other types of intragranular bubbles (draped flat bubble and interlinked chip bubble).</i>	<i>96</i>
<i>Figure 56 – TEM images of the two lamellae and positions of the grains and grain boundaries (yellow arrows). The pink rectangles correspond to the areas studied by diffraction.</i>	<i>97</i>
<i>Figure 57 – Examples of diffraction patterns obtained for the grain G1 of lamella 1 and resulting stereographic representation.</i>	<i>97</i>

Figure 58 – TEM images of bubbles (examples indicated by yellow arrows), bubbles network (green arrow) and grain boundary (red arrow), in over-focused on the left ($f = +1 \mu\text{m}$) and under-focused condition on the right ($f = -1 \mu\text{m}$). 98

Figure 59 – EDX maps of Mo, Pd, Rh, Ru, Tc, Xe and U in the grain G1 of the restructured area (in at.%). 99

Figure 60 – Examples of diffraction patterns obtained for the grains G1 (up) and G2 (bottom) and resulting stereographic representations. 100

Figure 61 – TEM images of bubbles (examples indicated by yellow arrows), bubbles network (green arrow) and grain boundary (red arrow), for grains G1 and G2 in over-focused and under-focused conditions..... 100

Figure 62 – EDX maps of Mo, Pd, Tc, Rh, Ru, U and O at the grain boundary in a non-restructured area (in at.%). 101

Figure 63 – EDX maps of Mo, Pd, Ru, Tc, Rh, O and U at cracks in a non-restructured area (in at.%). 102

List of Tables

<i>Table 1 – Severity scale from the DSS point of view</i>	19
<i>Table 2 – Severity scale from the SNF point of view</i>	20
<i>Table 3 – Design-Basis Tornado Characteristics from RG 1.76 (US NRC, January 2006)</i>	31
<i>Table 4 – Design-Basis Tornado Missile Characteristics and Maximum Horizontal Speeds from RG 1.76 (US NRC, January 2006)</i>	31
<i>Table 5 – Accident Severity Ranking</i>	41
<i>Table 6 – Best-fit values of the annular cylinder model parameters, as calculated from the optimisation process performed with OptiSlang.</i>	49
<i>Table 7 – Plastic strain at failure extracted for the different BU values corresponding to the material properties of Table 6, for the annular cylinder beam model.</i>	50

Glossary

ADR - European Agreement concerning the International Carriage of Dangerous Goods by Road

ANSI - American National Standards Institute

BU - Burnup

CC - Criticality Control

CF - Confinement

CIEMAT - Centro de Investigaciones Energéticas, Medioambientales y Tecnológicas

CRUD - Chalk River Unidentified Deposits

DSS - Dry Storage Systems

EOL - End-Of-Life

FEA - Finite Element Analysis

FRAPCON - Fuel Rod Analysis Program CONsumption

HT - Heat Transfer

IAEA - International Atomic Energy Agency

IDOM - Ingeniería y Dirección de Obras y Montajes

ISFSI - Independent Spent Fuel Storage Installation

MOP - Model of Performance

Nagra - National Cooperative for the Disposal of Radioactive Waste (Switzerland)

NRC - Nuclear Regulatory Commission

NUREG - Nuclear Regulatory Commission Regulations

PCT - Peak Cladding Temperature

PIRT - Phenomena Identification and Ranking Table

PWR - Pressurised Water Reactor

RG - Regulatory Guide

RS - Radiation Shielding

RT - Retrievability

SEM - Scanning Electron Microscopy

SNF - Spent Nuclear Fuel

SFA - Spent Fuel Assembly

SSC - Structures Systems and Components

SSG - Specific Safety Guide

TEM - Transmission Electron Microscopy

UOX - Uranium Oxide

Zy-4 - Zircaloy-4

1. Introduction

The management of radioactive waste is a critical component of the nuclear fuel cycle, requiring meticulous attention to safety and regulatory compliance. The European Joint Programme on Radioactive Waste Management (EURAD) aims to enhance methodologies and understanding for the safe handling, storage, and disposal of radioactive waste across Europe. This report, a deliverable from Work Package 8 (Spent Fuel Characterisation and Evolution until Disposal) of the EURAD project, focuses on the identification and analysis of potential accident scenarios in interim storage and packaging facilities, along with an assessment of fuel performance.

The primary objective of this deliverable is to identify and analyse potential accident scenarios that may occur in interim storage and packaging facilities for spent nuclear fuel (SNF). Evaluating these scenarios aims to understand their impacts on fuel performance and propose measures to mitigate associated risks. This work is essential for ensuring the safety of SNF storage solutions and maintaining regulatory compliance.

The scope of the work is divided in 3 areas:

- **Identification of accident scenarios:** identify possible accident scenarios in interim storage and packaging facilities.
- **Impact analysis:** analyse the impact of these scenarios on the performance of spent nuclear fuel.
- **Risk assessment methodology:** develop a methodology to assess and mitigate risks associated with these accident scenarios.

This report builds upon previous work conducted in the EURAD project, specifically within Sub-Task 4.1 related to “Accident scenario for fuel under dry interim storage conditions”. The particularity of this Sub-Task is that it builds upon the relevant work and progress made within Tasks 2 and 3, related to fuel properties characterisation and related uncertainty analysis, as well as on the behaviour of nuclear fuel and cladding after discharge. Various data generated either through numerical or experimental investigations are used to better characterise the fuel/cladding properties and the end-of-life (EOL) conditions, but also their evolution during dry storage conditions.

The report is structured into several key sections. Chapter 2 relates to the identification and risk assessment of accident scenarios. This study from IDOM builds upon previous work conducted in the EURAD project, specifically referencing methodologies developed in earlier progress reports during the project. The methodology includes a comprehensive review of potential initiating events and their consequences. Following, a detailed accident sequence analysis is performed to understand the progression and impact of each scenario. Finally, the evaluation of the effects on both the storage systems and the spent nuclear fuel is made, considering factors such as structural integrity, thermal behaviour, and criticality control.

One of the key findings from this study is that the most critical accident scenario in terms of impact both for the dry-storage cask, as well as on the spent fuel assemblies is the cask tip-over during either transport or handling. In that case, the spent fuel assemblies are subjected to flexural loading conditions that could potentially lead to possible fuel rod failure and therefore loss of their integrity. As a result, the following chapters try to analyse this type of loading conditions, by developing different methodologies to evaluate the state of the fuel rods after such type of accident scenarios, as well as the fuel rod failure probability. In the end, the final chapter provides a further insight into different phenomena associated with the fuel oxidation, as a result of cladding integrity loss.

In Chapter 3, the mechanical behaviour of Pressurised Water Reactor (PWR) spent fuel assemblies under different accident conditions is studied by Nagra using Finite Element Analysis (FEA). This section describes the transition from small-scale rodlet models to full-scale spent fuel assemblies and the need for computationally efficient models. Then, an evaluation on different modelling approaches is performed and an optimum approach is selected based on computational requirements and response under loading conditions. Thereafter, the rod failure criteria is discussed, where the rod plastic strain as function of burnup is selected as the indicator to investigate the rod structural integrity. Finally, the development of large-scale FE models is described in detail and an assessment of the structural response of a PWR spent fuel assembly is investigated under a postulated accident scenario resulting to flexural loading conditions on the fuel rods.

Chapter 4 is related to the work performed from CIEMAT and outlines a methodology to predict the probability of fuel rod failure in spent nuclear fuel (SNF) during accident scenarios. Integrating FRAPCON-xt, HYDCLAD, and DAKOTA, the approach provides fast and reliable estimates of fuel rod integrity through thermo-mechanical characterisation, cladding response modelling, and stochastic analysis. The methodology, tested on a PWR fuel rod under a hypothetical drop accident after 20 years of storage, shows significant safety margins with zero failure probability. Statistical analysis using Monte Carlo simulations considers variabilities in design, power history, storage, and accident conditions. The findings highlight robust performance and identify the need for further research in modelling irradiation damage recovery. The developed approach enhances the safety assessment of SNF storage and transport systems.

Finally, Chapter 5 investigates the behaviour of defective nuclear fuel rods in dry storage and off-normal conditions, specifically under air ingress scenarios. CEA conducted oxidation tests at 200°C on irradiated UO_x and MOX fuel sections with Zy-4 and M5 claddings over prolonged periods. Results show cladding rupture, suspected to originate from internal stress due to gas release and swelling, as no formation of U₃O₈ was evidenced. Detailed analyses, including metallography, SEM, and TEM, reveal the presence of radial and circumferential cracks and a non-continuous opening of the grain boundaries constituting a bubbles network, most likely contributing to cladding failure. The study enhances understanding of SNF behaviour under dry storage conditions and identifies the need for further research into initial rod conditions and irradiation history to fully elucidate failure mechanisms.

2. Identification and risk assessment of accident scenarios

2.1 Introduction and background

Licensing of spent fuel dry storage and transport systems imposes requirements on the designers of to ensure these systems are operated safely under a variety of scenarios: normal, off-normal and accident conditions.

Compliance with these requirements means that the so-called safety functions in the dry storage and transport systems must be guaranteed at all times. As these safety functions only apply to the systems themselves, designers focus their analyses primarily on them, and analyses of the fuel itself are usually left in the background.

Although fuel accident analyses are indeed carried out and some storage system designers do perform them to some extent, the relationships and interactions between the storage and transport system, as well as the consequences on the fuel during an accident are not clearly established. In addition, the fuel condition used in this analyses does not typically correspond to a real situation, since conservative assumptions are employed to account for degradation phenomena that alter the physical properties of the constituent materials (e.g. failure of a significant number of rods or even 100% of the rods). Therefore, for the analysis of accidents during interim storage, it is recommended to establish a clear understanding of the relationships between the postulated accidents for storage facilities and systems, and their effect on the spent fuel, while taking into consideration its condition.

This work attempts to offer an alternative view of accidents during spent fuel storage, trying to obtain the consequences and damage to the fuel in the event of an accident and to evaluate the severity of each one from the point of view not only of the storage system but also of the fuel.

To this end, firstly, a methodology applicable to any type of storage and transport system was developed in report IIT_002 (IDOM, November 2020) and then, the particular case of Spain has been analysed, which implies fuel and storage and transport systems commonly adopted in other European countries.

2.2 Objective

The purpose of this section is to qualify the severity of the accidents that might occur in the Dry Storage Systems (DSS) currently licensed in Spain, both from the DSS and the Spent Nuclear Fuel (SNF) point of view, according to the methodology presented in IIT_002 (IDOM, November 2020).

2.3 Scope

The scope of this part is limited to the DSS currently licensed in Spain, this is, Dual-Purpose Bare Fuel Casks and Multi-Purpose Canister (MPC) + Overpack systems, only in storage configuration and the fuel types allowed to be stored under the current licenses.

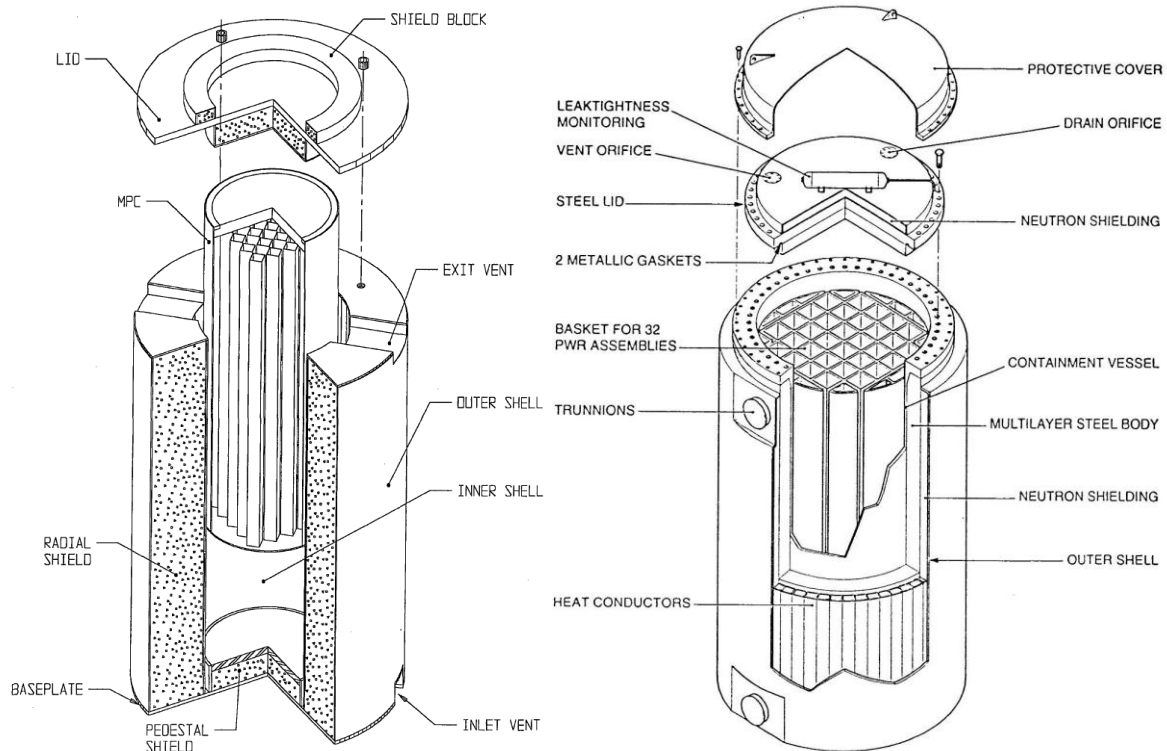


Figure 1 – MPC + Overpack / Bare Fuel Cask DSS examples from NUREG -2214 (NRC, 2019)

Although the DSS designs shown might not have common components, nor make use of the same auxiliary systems for their handling, in this section, an abstraction work has been made, with the aim of speaking generally of DSS.

For the identification of initiating events and postulated damages to the Storage System, the available information from the Storage System designers and licensees has been used, sticking exclusively to what has been postulated by them, typically following the guidance provided by the regulatory body on what type of accidents should be analysed. This is the case of the Standard Review Plans (SRP) like NUREG-2215 (US NRC, April 2020), in which a list of accidents to be evaluated is provided.

Subsequently, the additional contribution has been added by determining the possible modes of damage and effects on the SNF, from the Spanish perspective. Finally, it must be noted that beyond basis accidents have not been included in this analysis.

2.4 Methodology

2.4.1 Impact on the DSS

Accident Sequence Analysis

As explained in IIT_002 (IDOM, November 2020), the accident sequence analysis describes every step in the accident development chain, beginning with the initiating events, to finally obtain the ultimate consequences and damage to the DSS.

An initiating event is defined as any potential occurrence that could disrupt the normal operation of an installation, an Independent Spent Fuel Storage Installation (ISFSI) in this case. Therefore, an accident can be conceptually thought of as a combination of an initiating event, which triggers a series of system responses.

First, relationships between the lists of accidents and initiating events given in IIT_002 (IDOM, November 2020) are established, as it is shown in the analysis of each accident in section 0.

As indicated in the scope, the accidents and damages analysed are those postulated by the DSS designers, but this analysis could be extended to any other accident.

Impact on the DSS qualification

The first step to be carried out is to identify the types of damage to the DSS. After that, it becomes necessary to establish a scale for qualifying the impact of a given accident on the system itself.

For that purpose, the use of the DSS's Safety Functions is considered as a reference tool. Safety Functions are a series of conditions that must be maintained in order to ensure the radiological safety and avoid any harm to the people or the environment. They are required by regulation as per 10 CFR 72 (US NRC).

Because the DSS are designed so that in the event of "credible" accidents, postulated on the basis of a series of parameters (speeds, heights, depths, etc.), they will not lose their Safety Functions. The setback that arises is that, the DSS will not be severely damaged, so its Safety Functions will not only be maintained, but also is not supposed to be affected in any way. To deal with this, in the context of this document, the accident is treated in terms of its compromised Safety Functions, this is, the functions that are challenged during a given accident, taking into account which components of the DSS may be affected and what functions this components perform, and what are their associated Safety Functions.

As stated in to NUREG-2215 (US NRC, April 2020), the Safety Functions of the Structures, Systems and Components (SSC) in a DSS are: (1) Criticality, (2) Shielding, (3) Confinement, (4) Heat Transfer, (5) Structural Integrity and (6) Retrievability. As specified in the same reference, as a particularity, Retrievability shall only be applicable during normal and off-normal conditions, not applying to accident conditions. In this section, with aim to give a deeper insight into the implications of an accident, Retrievability of the fuel will also be considered, meaning by that the ability to recover fuel assemblies individually. Safety Functions are listed and briefly described with the following definitions.

- **Criticality Control (CC)**: The DSS should be designed to maintain spent nuclear fuel in a subcritical configuration during normal, off-normal and accident conditions. In this way even if the fuel remains in subcritical condition, any change in the DSS that will result in a variation of the effective neutron multiplication factor k_{eff} , will be considered a compromise to the CC.
- **Radiation Shielding (RS)**: The DSS should protect occupational workers and members of the public against direct radiation doses and minimise the dose from normal operations and from any off-normal or accident conditions. Any change in the DSS that will result in an increase of the radiation dose, even if it is localised, will be considered a compromise to the RS.
- **Thermal Evacuation / Heat Transfer (HT)**: Decay heat must be properly evacuated in order to maintain fuel, cladding and DSS temperatures under their allowable limits. Any change in the DSS that will result in an increase of the temperature of the DSS, its components and contents, close to their allowable limits, will be considered a compromise to the HT.
- **Confinement (CF)**: The DSS must prevent any radioactive material from being released outside its boundaries. Any change in the DSS that poses a risk to loss of containment will be considered a compromise to the CF.

- **Structural Support (SS):** Structural components should be designed to accommodate combined normal, off-normal, and accident loads while preserving recoverability and protecting the DSS or its contents from significant structural degradation, criticality, loss of shielding and loss of confinement. Any change in the DSS that will result in a change of the fuel configuration will be considered a compromise to the SS.
- **Retrievability (RT):** The DSS must ensure the capability to retrieve individual fuel assemblies. Any change in the DSS that will prevent or hinder fuel assemblies from being recovered will be considered as a compromise to the RT.

In this way, a scale from 0 to 6 is established, and the severity of a given accident is calculated as the sum of the compromised Safety Functions explained above. This is, after the analysis of the DSS components that may be damaged, their associated Safety Functions and the reasoning of whether these are compromised or not. No greater weight is given to one Safety Function than to another, so they all have the same weighting. Consequences may vary depending on the compromised Safety Function.

Severity Level	Description	
0	Negligible	No Safety Functions are compromised. No consequences are to be expected.
1	Limited severity	A single Safety Function is compromised.
2	Moderate severity	Two Safety Functions are compromised.
3	Considerable severity	Three Safety Functions are compromised.
4	High severity	Four Safety Functions are compromised.
5	Very high severity	Five Safety Functions are compromised.
6	Critical severity	All of the Safety Functions are compromised.

Table 1 – Severity scale from the DSS point of view

2.4.2 Impact on the fuel

Effects on the Fuel Analysis

The objective of this step is to analyse the kind of damage on the SNF assemblies (e.g., cladding breach, loss of geometrical configuration, overheating, etc.). The damage to the DSS can be conceptually thought of as the initiating event for the effects on the SNF.

The analyses included in the Safety Analysis Reports (SAR) typically focus on damages to the DSS, so the present step relies on previous knowledge and other sources of information, such as those referenced in IIT-003 (IDOM, August 2021) to look at the consequences on the fuel.

Impact on the Fuel Qualification

Each of the postulated accidents is assessed in terms of effects on the fuel, meaning as effect any circumstance that might change the initial fuel configuration. Using references like NUREG-2224 (US NRC, November 2020) and ISG-11 (US NRC, November 2003), it has been chosen to classify the effects in the following groups:

- Mechanical Effects (ME):
 - Cladding failure, either with breached (punctured) or damaged rods
 - Rod / assembly deformation without cladding failure
 - Changes to the assembly axial alignment without cladding failure
- Thermal Effects (TE):
 - Heating of the cladding
 - Repeated heating and cooling cycles
- Criticality Effects (CE):
 - Any immediate effect that will result in a variation of the effective neutron multiplication factor k_{eff}

It should be noted that these are immediate effects. Secondary effects (e.g., a change in the k_{eff} or ultimate cladding failure due to changes in fuel temperature) are acknowledged, but not considered.

In this way, for the qualification of the impact of an accident on the fuel, a scale from 0 to 3 is established, and the severity of a given accident is calculated as the sum of the effects shown above. This is, after the analysis of the modes of damage to the SNF and their association with the effects to the fuel. No greater weight is given to one effect than to another, so they all have the same weighting.

Severity Level	Description	
0	Negligible	No expected effects on the fuel.
1	Moderate severity	One type of effect on the fuel.
2	High severity	Two types of effects on the fuel.
3	Very high severity	All three types of effects on the fuel.

Table 2 – Severity scale from the SNF point of view

2.5 Accident analysis

2.5.1 Dry Storage System Tip-Over

The configuration of the analysed DSS during storage is vertical; however, a series of initiating events might cause them to violently tip-over on their side. Due to the accelerations that might occur during the

development of this accident (up to 97 g depending on the system type and the consulted analysis), it is considered a severe accident, and is recommended in NUREG-2215 (US NRC, April 2020) to be evaluated with high priority.

As explained in the methodology in section 2.4, the accident sequence analysis is performed, listing the initiating events and postulated damages, always according to the DSS designer.

Postulated cause(s)

- Tornado / hurricane winds
- Missiles generated by natural phenomena
- Flooding (due to flood water drag)
- Earthquake
- Lifting device failure (crane, transfer vehicle or lifting trunnion / anchor failure)

Postulated damage(s) to the DSS and related Safety Functions

- Overstress and deformation of certain structural components (e.g., shell, lids, bolting, support channels, etc.). (CF, SS, RT, HT)
- Overstress and deformation of basket plates. (CC, SS, HT, RT)
- Localised decrease in shielding material thickness (either concrete or polymeric, such as borated resins). (RS)
- General temperature increase due to horizontal reorientation, which could lead to component overheating, resulting in malfunction or damage. (HT)
- CRUD detachment. (No consequences to the Storage System from the safety point of view)

Accident analysis

All of the Safety Functions might be compromised during a DSS tip-over, making it an accident of high importance from the Storage System safety point of view.

Overstress in the structural components can lead to their deformation and depending on the magnitude of it, to the loss of one or more Safety Functions. As an example, sufficient deformation of the lid or bolts could lead to loss of tightness on the sealing gaskets of applicable Storage Systems, causing the sealing to be compromised and thus, the Safety Function of confinement to be compromised. Similarly, deformation of components like basket plates could cause changes in fuel configuration and disposition, in turn affecting the Safety Functions of Retrievability (RT), Criticality Control (CC) and Heat Transfer (HT).

The horizontal reorientation of the Storage System due to the drop does not correspond to the normal operating conditions for the analysed systems. This reorientation will result in a decrease in the rate of heat transfer from the fuel to the surroundings, increasing the temperature of the Storage System components and its contents. Depending on the consulted analysis, a detailed evaluation of the accident is carried out or, on the contrary, it is considered to be bounded by a more restrictive one, in which a maximum time for the vertical repositioning of the DSS is determined.

Lastly, Chalk River Unidentified Deposits (CRUD) detachment, which can occur as a result of deceleration and vibration experienced by the fuel assemblies during the drop, can cause it to settle and

accumulate at the bottom of the Storage System basket, potentially clogging the holes of the basket plates. It is demonstrated that the accumulation of CRUD will not affect heat dissipation since, for the designs in the scope, heat transfer relies either on thermal radiation or convection, being the Storage System is designed taking this hypothetical event into account.

Summary of compromised Safety Functions in the DSS: (CF, SS, RT, RS, HT, CC)

Severity of a Tip-Over from the DSS point of view	6
--	----------

Possible effects on the fuel

From the effects and damage to the Storage System, it is easy to imagine that there might also be a number of effects on the fuel, due the acceleration produced as a consequence of the tip-over, or the change in the configuration of both the DSS (horizontal reorientation), and the fuel assemblies (basket plate deformation):

- The fuel might suffer deformations and damages due to the accelerations induced on it (IDOM, August 2021), grid-to-rod fretting, etc. or, as mentioned above, it might be crushed and hit by violent contact with the components of the DSS (basket plates) or other fuel assemblies. Both these conditions induce mechanical loads on the fuel, which, depending on their magnitude and factors of the fuel itself (design, condition, fuel phenomena, etc.), might cause cladding breach and failure up to different extents explained in (IDOM, August 2021), (US NRC, November 2020), (EPRI, December 2021). In addition, deformation of the rods and changes in rod pitch might cause changes in the k_{eff} as well as thermal effects due to changes in heat transfer rate. (ME, TE, CE)
- The horizontal reorientation of the Storage System might lead to a decrease in the rate of heat transfer, increasing the temperature of the cask components and that of the fuel assemblies. If DSS is kept in the horizontal position for a sufficient period of time, the Peak Cladding Temperature (PCT) for short-term normal operating and accident conditions from ISG-11 (US NRC, November 2003), can be reached. (TE)
- The rearrangement of the fuel assemblies within the Storage System basket, both from the DSS horizontal reorientation and the deformation of the basket plates, regardless of whether the fuel assembly has been affected or it has been analysed as an off-normal condition, may cause a change in the k_{eff} , and thus affect the criticality control. (CE)
- The CRUD detachment is in principle, not considered to have any negative effects on the fuel. This is supported by the CRUD removal and ultrasonic fuel assembly cleaning operations that have sometimes been carried out to reduce contamination and operational risks during loading and unloading of storage and transportation systems (Kondoh & Fujita, 1994). (No consequences from the safety point of view)

Summary of effects on the SNF: (ME, TE, CE)

Severity of a Tip-Over from the SNF point of view	3
--	----------

2.5.2 Dry Storage System Drop

The drop of a DSS (with regard to the storage phase) might occur during the transfer operations from the spent fuel pool building to the Independent Spent Fuel Storage Installation (ISFSI) and vice versa, or during any handling operation (repositioning, inspections, etc.) due to a mechanical failure of the transfer or lifting devices. Lifting devices are designed so this kind of accidents won't happen; nevertheless, designers postulate this as a non-deterministic accident. As different transfer techniques and modalities are possible, a DSS drop might occur in vertical, horizontal or corner orientations, as stated in NUREG-2215 (US NRC, April 2020); each producing different effects on the Storage System and, by extension, also on the fuel. Regulations do not establish a limit to the height to which a DSS can be lifted; generally, license applicants establish the design basis in terms of the maximum height to which the DSS will be lifted outside the building or the maximum deceleration that the DSS should experience in a drop. In addition, the handling and transfer operations can be performed by means of auxiliary systems, such as transfer casks, cradle structures, etc., for which drop accidents might produce different effects.

In the same way as the tip-over, a drop accident can induce significant accelerations in the Storage System, which is why it is also routinely analysed by designers, following the regulator's recommendations.

2.5.2.1 Vertical Drop

A vertical drop is that in which the base of the DSS impacts against a sufficiently rigid, unyielding surface. The consulted analyses show that the vertical drop can induce accelerations up to 100 g for some Storage Systems if they are lifted up to a certain height, imposed by crane dimensions, ground clearance, etc. As explained earlier, other Storage System licensees make sure accelerations do not exceed design limits by keeping the lifting height below a certain height, or do not give credit to the drop through the use of lifting devices with redundant drop protection features and compliance with adequate standards and regulations (i.e., ANSI N14.6 (ANSI, June 1993), NUREG-0612 (US NRC, July 1980)). Last, in the context of this analysis, DSS tip-over is not considered after the drop.

Postulated cause(s)

- Lifting device failure (crane, transfer vehicle or lifting trunnion / anchor failure)

Postulated damage(s) to the DSS and related Safety Functions

- Overstress and deformation of basket plates. (CC, SS, HT, RT)
- Contact between inner lid and fuel assemblies. (No consequences to the Storage System from the safety point of view)
- CRUD detachment. (No consequences to the Storage System from the safety point of view)

Accident analysis

As can be seen from the list of damages to the DSS, the vertical drop has consequences mainly of a mechanical nature. Due to the intended functions of some components (e.g., the basket plates, which

ensure the correct positioning of the fuel assemblies), their deformation might also affect other Safety Functions, as explained in the effects on DSS derived from a tip-over accident.

The impact of the fuel assemblies against the inner lid of the Storage System is not expected to cause damage to the DSS and is therefore of no consequence from the DSS point of view.

Summary of compromised Safety Functions in the DSS: (CC, SS, RT, HT)

Severity of a Vertical Drop from the DSS point of view	4
---	----------

Possible effects on the fuel

- Mechanical damage, as explained in the effects on the fuel derived from the DSS tip-over accident. In this case, due to the vertical orientation of the DSS during the drop, the acceleration might produce fuel assembly buckling and individual rod buckling between spacers, among other effects thoroughly explained in (IDOM, August 2021). (ME, TE, CE)
- Fuel rearrangement, as explained in the effects on the fuel derived from the tip-over accident. (TE, CE)
- CRUD detachment, as explained in the effects on the fuel derived from the cask tip-over accident. (No consequences from the safety point of view)

Summary of effects on the SNF: (ME, TE, CE)

Severity of a Vertical Drop from the SNF point of view	3
---	----------

2.5.2.2 Horizontal Drop

A horizontal drop is that in which the DSS impacts on one of its sides, with the fuel assemblies parallel to the ground. In the same way as in the case of vertical drop, the consideration of this accident as postulable or not, and therefore its analysis and applicable parameters, depend on the Storage System and lifting / transfer devices used.

Depending on the Storage System, during the horizontal fall of the DSS, accelerations up to 103.8 g may develop, with the basket plates either parallel or oblique to the ground. In the consulted references, the analysis of horizontal drops is limited exclusively to the immediate effects following the drop, not considering later rolling, horizontal reorientation, etc.

Postulated cause(s)

- Lifting device failure (crane, transfer vehicle or lifting trunnion failure)

Postulated damage(s) to the DSS and related Safety Functions

- Damage to the water jacket outer shell and loss of the water of the transfer cask. (RS, HT)
- Overstress and deformation of basket plates. (CC, SS, RT, HT)
- CRUD detachment. (No consequences to the Storage System from the safety point of view)

Accident analysis

As mentioned in the introduction to the drop accident, the handling and transfer of the DSS may be done by means of auxiliary elements, such as transfer casks, etc. Therefore, and as it can be seen in the above list, these auxiliary elements may also be affected during the accident.

The damage of the water jacket shell and loss of water in it, though it has no consequences from a structural point of view, will affect the Safety Functions provided by the water, as it acts both as a means of decay heat extraction and as shielding against radiation.

Summary of compromised Safety Functions in the DSS: (SS, HT, CC, RS, RT)

Severity of a Horizontal Drop from the DSS point of view	5
---	----------

Possible effects on the fuel

- Mechanical damage, as explained in the effects on the fuel derived from the tip-over accident. In this case, due to the horizontal orientation of the DSS during the drop, the acceleration might produce fuel rod flexion between spacers, among other effects thoroughly explained in (IDOM, August 2021) . (ME, TE, CE)
- Fuel rearrangement, as explained in the effects on the fuel derived from the tip-over accident. (TE, CE)
- In a similar manner to the thermal effects on the fuel derived from the tip-over accident, the decrease in heat dissipation capacity derived from the loss of cooling water will consequently increase the temperature of the fuel assemblies. In the reviewed analyses, it is demonstrated that the PCT will remain under allowable limits for accident conditions (<400°C) from ISG-11 (US NRC, November 2003), which in principle ensures cladding integrity. (TE)
- CRUD detachment, as explained in the tip-over accident. (No consequences from the safety point of view)

Summary of effects on the SNF: (ME, TE, CE)

Severity of a Horizontal Drop from the SNF point of view	3
---	----------

2.5.2.3 Corner Drop

The last case of drop analysed in the reviewed documentation of the Storage Systems is the oblique or corner drop. The analyses are carried out choosing the angle at which the point of impact and the centre of gravity are vertically aligned, not considering later bouncing or impacts before settling.

In this case, the reviewed analyses show centre of gravity acceleration peak values up to 18 g, which is significantly lower than those obtained in previous cases.

Postulated cause(s)

- Lifting device failure (crane, transfer vehicle or lifting trunnion failure)

Postulated damage(s) to the DSS and related Safety Functions

- Overstress and deformation of inner shell. (CF, SS)
- Overstress and deformation of basket plates. (CC, SS, RT, HT)

Accident analysis

As can be seen from the list of postulated damages to the DSS and despite the fact that this type of drop is the one with the lowest induced acceleration, the corner drop is the only one that is considered it might compromise the confinement Safety Function; this is because stresses are concentrated in a smaller area.

Regardless of the type of fall analysed, the deformation of the basket plates is always postulable.

Summary of compromised Safety Functions in the DSS: (CF, SS, RT, HT, CC)

Severity of a Corner Drop from the DSS point of view	5
---	----------

Possible effects on the fuel

- Mechanical damage, as explained in the effects on the fuel derived from the tip-over accident. (ME, TE, CE)
- Rearrangement of the fuel assemblies within the Storage System basket, as explained in the effects on the fuel derived from the tip-over accident. (TE, CE)
- CRUD detachment, as explained in the effects on the fuel derived from the tip-over accident. (No consequences from the safety point of view)

Summary of effects on the SNF: (ME, TE, CE)

Severity of a Corner Drop from the SNF point of view	3
---	----------

2.5.2.4 Additional remarks on possible effects on the SNF in case of any drop accident

Normally, the drop accident is one of those that is analysed in greater depth. In addition, it is one of the few that some storage system designers analyse from the SNF point of view. IDOM IIT-003 (IDOM, August 2021) compiles some of these analyses and offers some conclusions regarding how these are carried out:

1. There is no reference methodology. There is little guidance and no strict regulation from regulatory bodies on how these analyses should be made, which results in a wide variety of methodologies and results.
2. There is no accident case definition. Accidents are specific to each of the analyses.
3. Input data affect the result. The input data that were identified from the review of the methodologies are:
 - Geometrical dimensions
 - Fuel rod length

- Length between supports
 - Cladding diameter
 - Fuel pellet diameter
 - Cladding thickness
 - Lateral restraints (gaps between rod and basket)
 - Irradiated material properties (allowable stress, Young modulus, Poisson ratio and tangent modulus). Result of un-irradiated material properties and neutron fluence received by the material.
 - Impact surface
 - Gas internal pressure
 - Weight (cladding and fuel)
 - Load duration
 - Lifting height
4. The assumptions taken during the calculation can significantly change the result of the analysis. Some input data, apart from differing in value from one analysis to another, can be both taken into account or discarded. The assumptions that were identified from the review of the methodologies are:
- Cladding weight consideration
 - Fuel weight consideration
 - Flexural rigidity of the fuel
 - Pellet-clad interaction
 - Boundary conditions in the rod supports (pin connection, resisting moment from adjacent spans, etc.)
 - Gas internal pressure consideration
 - Lateral restraints consideration
 - Consideration of irradiation in the material properties
 - Load duration considered

2.5.3 Fire

This accident is postulated to be caused mainly by a fire in the fuel tank of the transfer vehicle (crane, platform, truck, etc.), either during the movement or handling of the DSS or during the storage. The reviewed documentation of the analysed Storage Systems also indicate as a possible initiating event any fire inside or near the installation (forest or bush fires, other fuel sources, etc.), being those site-specific and therefore, requiring further evaluation by Storage System individual users.

It is noted that Storage System designers and licensees take, by indication of the regulator in NUREG-2215 (US NRC, April 2020), the parameters corresponding to a fire accident during transport (duration,

flame temperature, area, etc.), that can be found in 10 CFR 71 (US NRC) and ADR (ADR - European Agreement concerning the International Carriage of Dangerous Goods by Road), as no specific fire accident parameters in storage have been established.

Postulated cause(s)

- Transfer vehicle fire (fuel tank fire)
- Other causes (site specific)

Postulated damage(s) to the DSS and related Safety Functions

- Component overheating above allowable limits: outer lid seal. (No consequences from the safety point of view according to the reviewed documentation, as it is not considered to be related to CF)
- Loss of polymeric shielding material. (RS)
- Loss of coolant / shielding water in the water jacket. (HT, RS)

Accident analysis

The limited amount of flammable material results in a fire of short duration. Due to the large mass and the thermal inertia of the Storage System, high temperatures and pressures will not be reached. Nevertheless, exposed components made out of less resistant materials may reach their allowable limits.

Polymeric materials used as shielding material in some Storage Systems could, however, ignite and burn. Though unlikely, this situation is postulated, and is analysed as a non-mechanistic accident.

Lastly, for those Storage Systems or auxiliary devices that make use of active cooling systems, it is postulated that fire could cause boiling of the coolant/shielding water and the escape of the steam through safety systems such as pressure relief valves, with the consequential decrease of water level, affecting heat transfer and radiation shielding provided by it.

Summary of compromised Safety Functions in the DSS: (HT, RS)

Severity of a Fire from the DSS point of view	2
--	----------

Possible effects on the fuel

- Fuel temperature increase due to the decrease in heat dissipation capacity. According to the ISG-11 (US NRC, November 2003), keeping the PCT below a certain temperature (570 °C) during off-normal and accident conditions will ensure, in principle, its integrity. (TE)

Summary of effects on the SNF: (TE)

Severity of a Fire from the SNF point of view	1
--	----------

2.5.4 Explosion (External Overpressure)

An explosion within the boundaries of the storage area is not credible since there are no explosive materials within the site boundaries. Ignition of the fuel contained in the transfer vehicle (crane, platform, truck, etc.) fuel tank, on the other hand, is a credible cause of an explosion accident, but due to the limited amount of fuel available, the effects of an explosion would be minimal. Any off-site explosion on a nearby road, railway or industrial site is also considered credible, but should be treated as site-specific and therefore, would require a risk assessment and further evaluation by individual Storage System users. Both, the 10 CFR 72 (US NRC) and the Regulatory Guide 1.91 (US NRC, July 2011) are suggested as a guide for explosion evaluation in the reviewed documentation.

It is noted that Storage System designers and licensees take the parameters corresponding to an explosion accident during transport (140 kPa or 20 psi absolute), that can be found in 10 CFR 71 (US NRC), as no specific explosion parameters during storage have been found in any regulation.

Postulated cause(s)

- Transfer vehicle fuel tank explosion
- Off-site explosion (generic)

Postulated damage(s) to the DSS and related Safety Functions

- None

Accident analysis

It is found that any explosion that may occur in the proximity of a DSS results in an overpressure significantly lower than the overpressure produced during a flooding accident, and is therefore bounded by it. In any case, due to the high structural strength of the DSS, a large shock wave or overpressure is necessary to inflict any damage.

Summary of compromised Safety Functions in the DSS: (None)

Severity of an Explosion from the DSS point of view	0
--	----------

Possible effects on the fuel

- As seen in the previous section, none of the Safety Functions of the DSS are compromised during the external explosion accident, so damage to the DSS is unlikely. By extension, it is considered that there are no adverse effects on the fuel during this kind of accident. (No effects on the SNF)

Summary of effects on the SNF:
(None)

Severity of an Explosion from the SNF point of view	0
--	----------

2.5.5 Lightning

The Storage Systems under the scope can be placed in a sheltered environment, such as storage buildings, underground vaults etc., or out in the open, on pads or soil. In the latter case, it is credible that, during the course of a thunderstorm, they may be struck by lightning.

Postulated cause(s)

- Electrical storm

Postulated damage(s) to the DSS and related Safety Functions

- Localised increase of the temperature in the component hit by the lightning. (No consequences from the safety point of view)

Accident analysis

This accident has negligible consequences from a safety point of view. Though it is considered that lightning can induce high currents, they last a short period of time (less than a second) and therefore they carry a limited quantity of energy. In addition, thanks to the high electric conductivity of the DSS materials (mostly metal) the most part of the lightning energy will discharge to ground and not be deposited in the Storage System itself.

As described in the previous list, the only damage to the DSS occurs at the point of impact, resulting in a slight localised increase in the temperature of the component hit by the lightning.

Summary of compromised Safety Functions in the DSS: (None)

Severity of a Lightning from the DSS point of view	0
---	----------

Possible effects on the fuel

- The high electric conductivity of the materials of which the DSS is made of will cause the energy from the lightning to be driven and dissipated through the Storage System components and thus not affect the fuel assemblies. It can therefore be considered that the fuel will not be affected during the course of the accident. (No effects on the SNF)

Summary of effects on the SNF: (None)

Severity of a Lightning from the SNF point of view	0
---	----------

2.5.6 Object Impact

The impact of an object carried by the wind of a considerable magnitude is a postulated. Three cases are considered, as depending on the size, weight and nature of the object, the effects on the Storage System can vary significantly. In this way, the impact of a large projectile is analysed, as a vehicle blown by the wind from a tornado could be, which could cause damage to the DSS, as well as overturning it;

a medium-sized, rigid projectile, such as a piece of pipe or a log, with the capacity to penetrate the neutron shielding or even the containment barrier (shells, lids, etc.); and finally, a small projectile with penetration capability and sufficient size to slip through any inlet, ventilation hole, etc. the Storage System may have, especially in case of Storage Systems with overpack.

Regulatory Guide (RG) 1.76 (US NRC, January 2006) defines the design-basis tornado and tornado missiles for nuclear power plants in the contiguous United States of America but, due to the lack of any other location-specific guidance, is sometimes adopted by DSS licensees outside United States and *Table 3* summarise the design-basis tornado characteristics used in RG 1.76 (US NRC, January 2006).

Region	Maximum wind speed m/s (mph)	Translational speed m/s (mph)	Maximum rotational speed m/s (mph)
I	103 (230)	21 (46)	82 (184)
II	89 (200)	18 (40)	72 (160)
III	72 (160)	14 (32)	57 (128)

Table 3 – Design-Basis Tornado Characteristics from RG 1.76 (US NRC, January 2006)

Missile Type		Big Object	Medium Object	Small Object
Dimensions	<u>Region I & Region II</u>	5 m x 2 m x 1,3 m (16,4 ft x 6,6 ft x 4,3 ft)	0,168 m dia x 4,58 long (6,625 in. dia x 15 ft long)	2,54 cm dia (1 in. dia)
	<u>Region III</u>	4,5 m x 1,7 m x 1,5 m (14,9 ft x 5,6 ft x 4,9 ft)		
Mass	<u>Region I & Region II</u>	1810 kg (4000 lb)	130 kg (287 lb)	0,0669 kg (0,147 lb)
	<u>Region III</u>	1178 kg (2595 kg)		
Vh ^{max}	Region I	41 m/s (135 ft/s)	41 m/s (135 ft/s)	8 m/s (26 ft/s)
	Region II	34 m/s (112 ft/s)	34 m/s (112 ft/s)	7 m/s (23 ft/s)
	Region III	24 m/s (79 ft/s)	24 m/s (79 ft/s)	6 m/s (20 ft/s)

Note: The NRC considers the missiles listed in *Table 3 – Design-Basis Tornado Characteristics from RG 1.76*

to be capable of striking in all directions with horizontal velocities of Vh^{max} and vertical velocities equal to 67 percent of V^{max}.

Table 4 – Design-Basis Tornado Missile Characteristics and Maximum Horizontal Speeds from RG 1.76 (US NRC, January 2006)

Although other scenarios and the impact of various objects (aircraft strikes, etc.) are postulated in other references, such as SSG-15 (IAEA, 2012) from the International Atomic Energy Agency (IAEA), and are progressively acquiring interest and relevance, to date, they are not required by regulation nor included in Storage System accident analyses.

2.5.6.1 Big Object

In the reviewed documentation, this accident is analysed for the storage and transfer stages, with the corresponding auxiliary systems used in each case (overpack, transfer cask, etc.), when applicable. The concern about this accident lies in the fact that the impact of a sufficiently large object with sufficient speed, combined with the drag from the wind, could cause the DSS to tip-over, condition that has already been analysed in section 2.5.1. Apart from the damage derived from the tip-over, the effect of the missile itself on the Storage System components is analysed as well. In the case of a large projectile impact, it is considered to be deformable.

Postulated cause(s)

- Missiles generated by natural phenomena (tornado winds, hurricane, etc.)

Postulated damage(s) to the DSS and related Safety Functions

- Damage to the water jacket shell and loss of the water of the transfer cask. (RS, HT)

Accident analysis

Of all the Storage Systems and configurations evaluated in the reviewed analyses, no occurrence of tip-over has been determined for the tornado characteristics summarised in Table 2 and Table 3 due to a big object impact.

Significant damage has only been found in case of an impact to the transfer cask. The consequence is the perforation of the water jacket outer shell and the consequent loss of the water, which serves as means of coolant and radiation shielding, thus affecting the respective Safety Functions.

Summary of compromised Safety Functions in the DSS: (RS, HT)

Severity of an Impact from a Big Object from the DSS point of view	2
---	----------

Possible effects on the fuel

- As explained in the thermal effects on the spent fuel derived from the loss of water in the water jacket during other accidents (e.g., horizontal, fire), a decrease in the capacity of extracting heat coming from fuel might occur. Analysis carried out by the licensee show that, although the fuel temperature rises above the normal operating temperature, it does not reach extremely high values (>400°C), which according to ISG-11 (US NRC, November 2003), could, in principle, compromise the structural integrity of the cladding. (TE)

Summary of effects on the SNF: (TE)

Severity of an Impact from a Big Object from the SNF point of view	1
---	----------

2.5.6.2 Medium Object

As explained earlier, a medium-sized, rigid projectile, such as a piece of pipe or a log, could have the capacity to penetrate the neutron shielding or even the containment barrier. In addition, depending on the analysis consulted, credibility is given to the possibility of a cask tip-over, as a consequence of the medium object impact. In other analyses, due to the large difference between the masses of the DSS and projectile, a tip-over is not postulated. Nevertheless, as required by RG 1.76 (US NRC, January 2006), Storage System penetration shall be analysed.

Postulated cause(s)

- Missiles generated by natural phenomena (tornado winds, hurricane, etc.)

Postulated damage(s) to the DSS and related Safety Functions

- Water jacket outer shell penetration (though omitted for conservatism) and loss of water in the water jacket of the transfer cask. (HT, RS)
- Penetration of certain transfer cask components (e.g., lid door outer shell, lid lead shielding, outer shell). (RS)
- Penetration and plastic deformation of certain Storage System components (e.g., outer shell, outer lid). (No consequences from the safety point of view)
- Radiation shielding penetration (either concrete, lead, or polymeric materials). (RS)

Accident analysis

Of all the Storage Systems and configurations evaluated in the reviewed analyses, no occurrence of tip-over has been determined for the tornado characteristics summarised in *Table 3* due to a medium-sized object impact.

As noted in the list of damages to the different Storage Systems, in some cases, the accident analyses do not take into account the intervention of some components (e.g., outer shell of the water jacket). This is done to add conservatism to the calculation, as omitting these components implies more kinetic energy from the projectile to be transferred to components of greater concern (inner shells with confinement function).

Nevertheless, it is demonstrated that, for the tornado characteristics in RG 1.76 (US NRC, January 2006), medium-sized object will not carry sufficient energy to compromise the confinement boundary of the Storage Systems.

Summary of compromised Safety Functions in the DSS: (RS, HT)

Severity of an Impact from a Medium Object from the DSS point of view	2
--	----------

Possible effects on the fuel

- As explained above, the impact of a medium-sized object is not capable of causing the tip-over or substantial movement of the DSS, so no loads of a mechanical nature will be induced on the fuel. The loss of water in the outer jacket, as explained throughout the rest of this document, will lead to a reduction of heat dissipation, and to an increase in the temperature of the fuel assemblies. According to the analyses consulted, during this condition, PCT will remain under short-term and accident conditions in ISG-11 (US NRC, November 2003). (No effects to the SNF)

Summary of effects on the SNF: (None)

Severity of an Impact from a Medium Object from the SNF point of view	0
--	----------

2.5.6.3 Small Object

The last case of projectile impact is analysed considering an object small enough to slip through any inlet, ventilation hole, etc. the Storage System may have, especially in case of Storage Systems with overpack. The geometry of the Storage System must ensure that no direct impact of the projectile on any component whose failure could lead to loss of containment is allowed.

Due to the large difference between the masses of the object and the Storage System, the DSS tip-over is precluded.

Postulated cause(s)

- Missiles generated by natural phenomena (tornado winds, hurricane, etc.)

Postulated damage(s) to the DSS and related Safety Functions

- Dents without penetration. (No consequences from the safety point of view)

Accident analysis

It is demonstrated that the kinetic energy of the small projectile is not sufficient to cause damage to the external components of the Storage System (including auxiliary systems) in any case, producing only small indentations, which in no case penetrate far enough to compromise any Safety Function.

Summary of compromised Safety Functions in the DSS: None

Severity of an Impact from a Small Object from the DSS point of view	0
---	----------

Possible effects on the fuel

- From the list of damages to the DSS, it can be seen that the impact of the small-sized object has minimal effect on the Storage System and therefore no effect on the fuel. (No effects on the SNF)

Summary of effects on the SNF: (None)

Severity of an Impact from a Small Object from the SNF point of view

0

2.5.7 Flooding

Like the site in which they are located, the ISFSI and the Storage System contained therein should be placed above the probable flood elevation for a specified return period, which has been cautiously determined. Flooding of the Storage System is therefore highly improbable, but is still being analysed. In case of multi-purpose Storage Systems, where the system is intended to be used both for storage and transport, a flood test is required by 10 CFR 71 (US NRC) and ADR (ADR - European Agreement concerning the International Carriage of Dangerous Goods by Road).

The flooding accident is approached in different ways depending on the consulted analysis:

- a) Establishing a certain height of water or pressure head based on design loads and analytically evaluating whether the DSS will be able to withstand this pressure head without losing its tightness.
- b) Applying the loads as a function of height of the water and determining the maximum pressure that the DSS is capable of withstanding, as well as the failure mode of the DSS (loss of tightness through the seals, lid failure, shell failure, etc.). This, depending on the type of DSS, yields figures (several hundred meters in some cases) that could hardly be reached during a flood episode in an ISFSI, perhaps during a transport accident across a lake or the sea, which are not within the scope of this document.

Lastly, in case of Storage Systems with overpack, which rely on natural convection as means of heat evacuation, a smart flood condition is postulated by DSS designers, where water rises just enough to block the lower air inlets of the overpack. This condition is analysed in section 2.5.11.

Postulated cause(s)

- River overflow
- Tsunami
- Dam breach
- Tank rupture

Postulated damage(s) to the DSS and related Safety Functions

- Lid seal leak and DSS flood. (CF, CC)
- Total structural collapse. (SS, CF, RT, CC, HT, RS)

Accident analysis

The loss of tightness through the seals of the DSS lid would cause the interior cavity to flood and to be filled with water, equalising the pressures outside and inside of it, and not changing the geometrical configuration of the DSS.

In the event of a total failure of the DSS it is possible that it would be crushed in such a way that it would become completely unusable. This condition is not credible during a flood episode, as it would only occur at large depths and would imply that seals have not leaked before, something that according to the analyses, would occur at shallower depths, and therefore is dismissed.

In the event of a shallow flood (not to be confused with smart flood condition explained in section 2.5.11), the only effect on the Storage System would be an increase heat removal capacity.

Summary of compromised Safety Functions in the DSS: (CF, CC)

Severity of a Flooding from the DSS point of view	2
--	----------

Possible effects on the fuel

Distinguishing between the previous cases, in case of a loss of tightness through a seal, the fuel elements would be subject to the pressure of the surrounding water after the flood. The pressure to which the fuel elements are subjected during the operation of a reactor, of the order of 13 MPa for a PWR and 7 MPa for a BWR, is considerably higher than that which can be reached during a ISFSI flood, so no concerns are raised.

In the event of a structural failure of the DSS, the fuel elements would probably be crushed in a way that they would be unrecoverable, and thus affected in every way.

In the event of a shallow flood (not to be confused with smart flood condition explained in section 2.5.11), the only effect on the fuel would be an increase heat removal capacity due to the improvement in convection coefficient and thus, the further cooling of the fuel.

Summary of effects on the SNF: (None)

Severity of a Flooding from the SNF point of view	0
--	----------

2.5.8 Burial under Debris

The Storage Systems under the scope can be placed in a sheltered environment, such as storage buildings, underground vaults etc., or out in the open, on pads or soil. In any of these cases, there is a possibility that they might end up being buried by debris, originating from following sources:

Postulated cause(s)

- Building collapse
- Debris transported by a tornado
- Debris transported in a flooding
- Mudslide

Postulated damage(s) to the DSS and related Safety Functions

- Component overheating (e.g., inner seal). (HT, CF)
- Structural effects (bounded by flooding accident and dismissed).

Accident analysis

In the case of burial under debris, the Storage System might be affected in the following ways:

- 1) The weight of the debris or any object might impose mechanical loads and structural consequences on the DSS. According to the analyses consulted, these consequences are covered by those of the flood accident explained in section 2.5.7.
- 2) The debris that surrounds the DSS will act as an insulator, both against radiation and against heat evacuation. In the first case, from the point of view of radiological protection, it does not have adverse consequences, in the second case, the accumulated debris might act as an adiabatic insulator, increasing the temperature of the components of the Storage System, as well as its content.

The analysis of this last condition is carried out as follows: it is considered that the container is adiabatically isolated and the maximum heat generation for which the Storage System is designed for is imposed. The temperature of the components of the DSS and the fuel will increase indefinitely until one of them reaches the admissible limit, point at which the DSS is considered to have failed. This limit will be reached after a certain time, of the order of several tens of hours, thanks to the great mass and thermal inertia of the container. This time limit indicates the time available to unearth a container after it is buried to avoid damage to the DSS and SNF.

Summary of compromised Safety Functions in the DSS: (CF, HT)

Severity of a Burial under Debris from the DSS point of view	2
---	----------

Possible effects on the fuel

- Limiting exclusively to the effects caused by the adiabatic isolation of the container, as a result of its burial, the fuel elements behave in the same way and suffer the same effects as the container. As explained in the thermal effects on the spent fuel derived from other accidents (e.g., tip-over, fire, object impact, etc.) the effect, therefore, is the increase in fuel temperature, which shall be maintained below short-term and accident conditions in ISG-11 (US NRC, November 2003). (TE)

Summary of effects on the SNF: (TE)

Severity of a Burial under Debris from the SNF point of view	1
---	----------

2.5.9 Extreme Temperature Changes

This accident refers to possible increase in temperatures due to natural causes (e.g., during heat waves) that will be maintained for several days, long enough to allow the Storage System to reach thermal equilibrium.

Postulated cause(s)

- Extreme environmental temperatures held for several days

Postulated damage(s) to the DSS and related Safety Functions

- No consequences from the safety point of view (material heating under allowable limits).

Accident analysis

The atmosphere acts as a cold temperature sink for the evacuation of the heat generated by the fuel, being the later at a significantly higher temperature (an order of magnitude) during dry storage. The Storage Systems are designed to work in a range of temperatures that can occur throughout the year, for what historical temperatures of the locations where they will be placed have been taken into account. The effect of an increase in the atmospheric temperature around the DSS, although it would slightly affect the heat evacuation, does not have adverse consequences on the DSS or the fuel, since it would be a limited increase compared to the normal temperature of the DSS.

Summary of compromised Safety Functions in the DSS: (None)

Severity of Extreme Temperature Changes from the DSS point of view	0
---	----------

Possible effects on the fuel

- In the same way as the temperature increase in the DSS components, a slight increase in the temperature of the fuel, which will be at any case within short-term accident conditions, does not impose any effect to the fuel performance. (No effects on the SNF)

Summary of effects on the SNF: (None)

Severity of Extreme Temperature Changes from the SNF point of view	0
---	----------

2.5.10 Supplemental Cooling System Failure

This accident applies only to Storage Systems that make use of some type of auxiliary equipment for the transfer of fuel to the storage module and with active cooling systems (e.g., a transfer cask with a water jacket).

In addition, it must be noted that, based on the review of certain Operating Experience (OE), it has been found that this kind of accidents have indeed occurred during the loading this type of Storage Systems.

Postulated cause(s)

- Electrical supply failure
- Loss of coolant

Postulated damage(s) to the DSS and related Safety Functions

- Component overheating due to heat transfer decrease. (HT)
- Loss of radiation shielding water. (RS)

Accident analysis

As indicated in the postulated causes, the loss of the supplemental cooling system can occur as a result of a failure of the system responsible for circulating and cooling the water (either due to a system or general electrical failure) or due to the loss of the coolant itself (due to a leak, poor operation, evaporation after a fire, etc.).

In the first case, the immediate consequence of the failure of the electrical system is the increase of the coolant temperature to boiling point and relief of generated steam through a pressure relief valve, until jacket of the transfer cask is partially empty, affecting the heat dissipation and radiation shielding.

Summary of compromised Safety Functions in the DSS: (RS, HT)

Severity of a Supplemental Cooling System Failure from the DSS point of view	2
---	----------

Possible effects on the fuel

- As explained in the thermal effects on the fuel derived from other accidents (e.g., tip-over, fire, object impact, etc.) the effect, therefore, is the increase in fuel temperature, which shall be maintained below short-term and accident conditions in ISG-11 (US NRC, November 2003). (TE)

Summary of effects on the SNF: (TE)

Severity of a Supplemental Cooling System Failure from the SNF point of view	1
---	----------

2.5.11 Blockage of Air Inlets

This accident only applies to systems that make use of an overpack during the storage phase, and which rely on heat dissipation by natural convection and air circulation through ventilation openings. If the vents were to become blocked, air circulation would be interrupted, leading to a reduction in heat dissipation. Unlike in the case of burial under debris accident analysed in section 2.5.8, in this case the DSS is not adiabatically insulated, so that heat extraction through the outer surfaces of the DSS is still possible.

As seen in other sections, the causes postulated for this accident may be various, and of different nature.

Postulated cause

- Snow
- Volcanic activity
- Flooding (flood water or debris)
- Debris transported by a tornado

Postulated damage(s) to the DSS and related Safety Functions

- Material overheating due to heat transfer decrease. (HT)

Accident analysis

The development and the effects of this accident are similar to those of thermal nature during DSS burial under debris, explained in section 2.5.8, which bounds this one.

The main effect is an increase in the temperature of the Storage System components and a consequent increase in the pressure in the canister containing the fuel assemblies. However, for a determined period of time, which exceeds that of the scheduled periodic surveillance at the ISFSI (in which the objects that may be blocking the ventilation openings shall be discovered and removed), the temperature and pressure values will remain below the admissible limit.

Summary of compromised Safety Functions in the DSS: (HT)

Severity of a Blockage of Air Inlets from the DSS point of view	1
--	----------

Possible effects on the fuel

- As explained in the thermal effects on the fuel derived from other accidents (e.g., tip-over, fire, object impact, etc.) the effect, therefore, is the increase in fuel temperature, which shall be maintained below short-term and accident conditions in ISG-11 (US NRC, November 2003). (TE)

Summary of effects on the SNF: (TE)

Severity of a Blockage of Air Inlets from the SNF point of view	1
--	----------

2.6 Summary of accidents and results

This section summarises the results of the analysis carried out in section 2.5 by means of Table 5 and Figure 2 –, helping to visualise which accidents possess the highest severity from the point of view of the Dry Storage Systems and Spent Nuclear Fuel.

ACCIDENT		DSS	SNF	
1	Dry Storage System Tip-Over	6	3	
2.1	Dry Storage System Drop	Vertical Drop	4	3
2.2		Horizontal Drop	5	3
2.3		Corner Drop	5	3
3	Fire	2	1	
4	Explosion (External Overpressure)	0	0	
5	Lightning	0	0	
6.1	Object Impact	Big Object	2	1
6.2		Medium Object	2	0
6.3		Small Object	0	0
7	Flooding	2	0	
8	Burial under Debris	2	1	
9	Extreme Temperature Changes	0	0	
10	Supplemental Cooling System Failure	2	1	
11	Blockage of Air Inlets	1	1	

Table 5 – Accident Severity Ranking

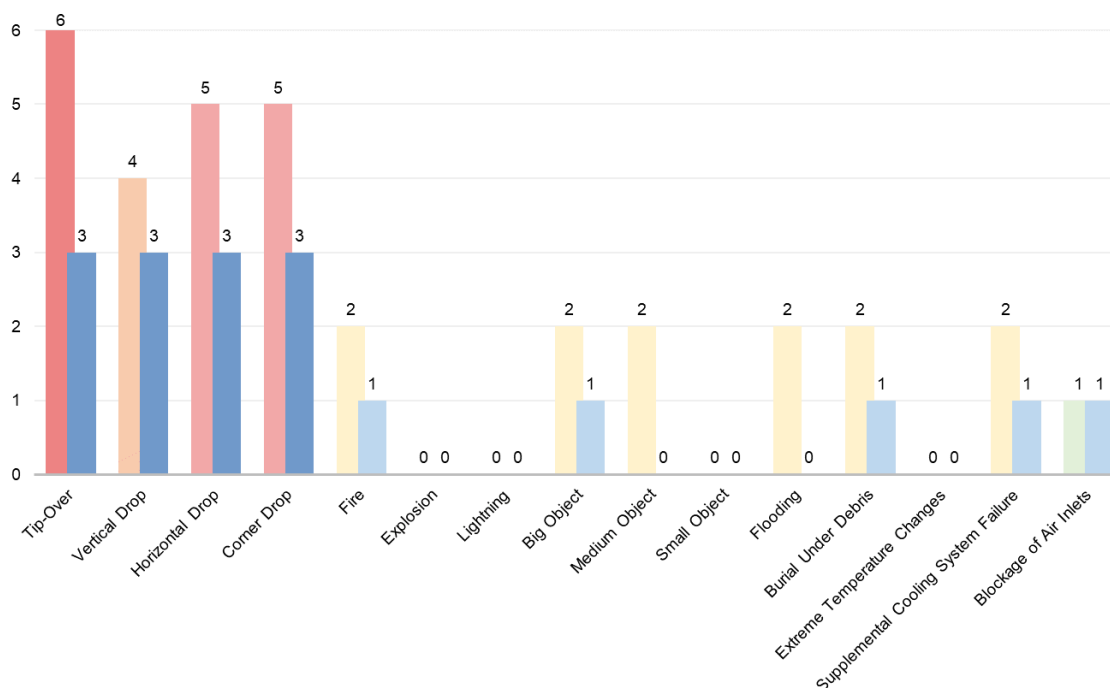


Figure 2 – Accident Severity Chart

In summary, some conclusions are drawn:

- The severity of an accident in the DSS is not necessarily related to the severity in the SNF, as it can be seen in the case of flooding or medium object impact.
- Accidents involving movement of the DSS (tip-over and drop) can have the greatest effect on the fuel, which confirm the prioritisation of their analyses, whatever its relevance from the DSS point of view.
- A number of analyses that are not of great relevance from the DSS nor SNF damage point of view are identified (explosion, lightning, small object or extreme temperature changes).

2.7 References

- ADR - European Agreement concerning the International Carriage of Dangerous Goods by Road.* (n.d.).
- ANSI. (June 1993). *ANSI N14.6-1993.*
- EPRI. (December 2021). *EPRI 30020200929 Phenomena Identification and Ranking Table (PIRT) Exercise for Spent Fuel Cladding Gross Rupture.*
- IAEA. (2012). *SSG-15 Storage of Spent Nuclear Fuel.*
- IDOM. (August 2021). *EJP-EURAD_IIT_003 A Review of Loading Types and Magnitudes in Spent Fuel Assemblies During Dry Cask Drop Accidents.*
- IDOM. (November 2020). *EJP-EURAD_IIT_002 Dry Cask Storage and Spent Fuel Phenomena Risk Assessment Methodology & Potential Accidents.*
- Kondoh, K., & Fujita, C. (1994). *CRUD removal for fuel assembly by ultrasonic cleaning.*
- NRC. (2019). *NUREG-2214 Managing Aging Processes In Storage (MAPS) Report.*
- US NRC. (n.d.). *10 CFR Part 71 Packaging and Transportation of Radioactive Material.*
- US NRC. (n.d.). *10 CFR Part 72 Licensing Requirements for the Independent Storage of Nuclear Fuel, High-Level Radioactive Waste, and Reactor-Related Greater than Class C Waste.*
- US NRC. (April 2020). *NUREG-2215 Standard Review Plan for Spent Fuel Dry Storage Systems and Facilities.*
- US NRC. (January 2006). *Regulatory Guide 1.76 Design-Basis Tornado and Tornado Missiles for Nuclear Power Plants.*
- US NRC. (July 1980). *NUREG-0612 Control of Heavy Loads at Nuclear Power Plants.*
- US NRC. (July 2011). *Regulatory Guide 1.91 Evaluations of Explosions Postulated to Occur at Nearby Facilities and on Transportation Routes Near Nuclear Power Plants.*
- US NRC. (November 2003). *ISG-11 Cladding Considerations for the Transportation and Storage of Spent Fuel.*
- US NRC. (November 2020). *NUREG-2224 Dry Storage and Transportation of High Burnup Spent Nuclear Fuel.*

3. Study of the mechanical performance of PWR SFA in accident scenarios with Finite Element Analysis

3.1 From small scale rodlet models to full scale spent fuel assemblies

3.1.1 Abstract

Based on the experimental data of three-point bending tests performed on irradiated rodlets, a series of so-called “3D models” were developed in Ansys® version 2021 R1 [1]. These models contain a detailed representation of pellets and cladding using 3D finite elements (FEs) and in combination with the experimental data, they were used to quantify the mechanical properties of the model components. This procedure is described in greater detail in [15].

The current report focuses on the subsequent steps of these investigations. First, the procedure of creating rodlet models from 1D beam elements with the same mechanical response as the 3D models under bending loads is described. The goal of this effort is to reduce the computation requirements of the so called “1D models” so that they can be used as a basis for modelling larger scale components and assemblies. Different modelling approaches are evaluated while sensitivity and optimisation studies are performed to determine the response of each model.

Based on the 1D model selected as optimal with regards to computational requirements and response under loading, failure criteria were defined for fuel rods using strain as an indicator of failure. Subsequently, a series of smaller scale models and eventually a full-scale FE of a spent fuel assembly (SFA) was created. This full-scale model was subjected to a bending load and was used to evaluate how forces are distributed between components and evaluate a series of results that allow to determine whether fuel rod failure has occurred, based on the derived failure criteria.

3.1.2 Introduction

Detailed beam models (hereafter named “3D models”) were created with the purpose of evaluating the mechanical properties of fuel rods based on the force-displacement curves extracted from three-point bending tests. Even though the final optimised models can model the response of actual rodlets with great success, they are limited by their increased computational requirements. Therefore, this detailed modelling approach would not be suitable for creating larger scale assemblies. Consequently, a solution to reduce the computational cost, while maintaining agreement between the experimental data and the finite element model (FEM), needed to be found.

The high computational requirements of the 3D models can be attributed to two main factors:

- The contacts between the different components of the model (e.g., pellet-to-pellet, pellet-to-cladding, etc.)
- The increased number of FEs necessary to model all components and achieve a solution independent to the number of elements.

To address both above-mentioned factors, it was decided to simplify the created FEMs by leveraging simpler FEs during the modelling process. Specifically, it was decided to recreate the three-point bending test using 1D elements (lines) to represent the different components of the fuel rods. Different models were created, each with a varied amount of complexity. The reasoning behind the selection of the most appropriate model which will be used to create larger scale assemblies is presented in the

following section. The detailed 1D beam model analysis on which the following reasoning is based on can be found in [2].

3.1.3 Modelling approaches and optimal simplified model selection

3.1.3.1 Evaluated 1D models

Three different 1D models were developed, each with a different modelling approach and with different complexity. All models were subjected to the same optimisation process, to determine which one best represented the experimental results of the three-point bending experiment. The main characteristics of each model are summarised below:

- Annular cylinder model – The fuel rod is represented using beam elements with an annular cylindrical cross-section, which has the geometrical properties of the cladding. Pellets are not modelled explicitly.
- Cylinder model – The fuel rod is represented using beam elements with a cylindrical cross section with the same diameter as the outer diameter of the fuel rod cladding. Pellets are not modelled explicitly.
- Combined model – The cladding is represented using beam elements with an annular cylindrical cross-section. Additionally, pellets are represented by a single cylindrical beam. It was also attempted to create a combined model with individual cylindrical beams acting as pellets; however, the endeavour was soon abandoned as the created model resulted in serious convergence issues and its computational cost was comparable to that of the 3D model when convergence was eventually achieved.

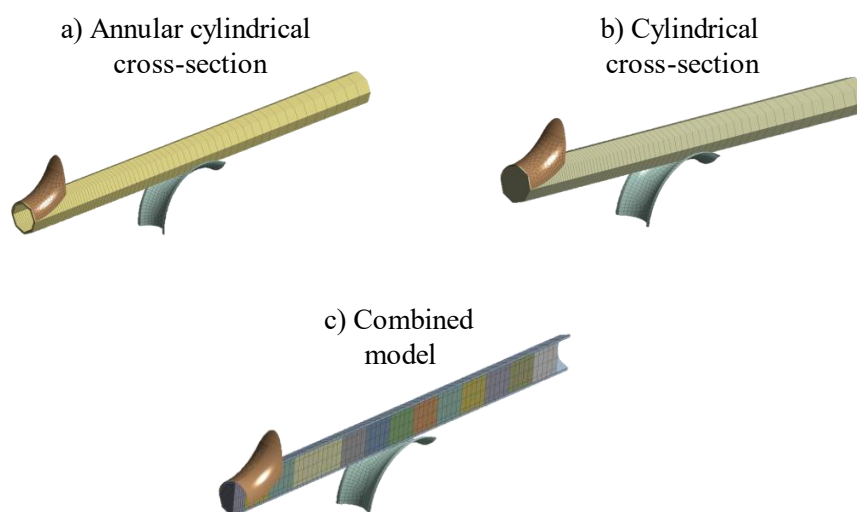


Figure 3 – The three different 1D models evaluated to determine which best corresponds to the mechanical data of three-point bending tests and has lower computational requirements. a) Model with annular cylindrical cross-section elements and cladding geometrical properties, b) Model with cylindrical cross-section elements and diameter equal to the cladding outer diameter, c) Model with annular cylindrical cross-section elements representing the cladding and cylindrical cross section elements representing the pellets placed inside the cladding.

3.1.3.2 Material models, sensitivity studies and optimisation procedure

The material properties of models a) and b) as well as of the cladding of model c) are defined with the use of the Voce material model as this is implemented in Ansys® (Eq. 1). In the case of the pellets of model c) a bilinear material law is used to define their material properties. The Voce material model is used to describe the response of a material after it has entered the plasticity regime, or in other words, after it has exceeded its yield stress (YS).

$$\sigma = \sigma_0 + R_0 * \varepsilon_{pl} + R_{inf} * (1 - e^{-b*\varepsilon_{pl}}) \quad (Eq. 1)$$

Where σ is the calculated stress, σ_0 is the initial YS of the material, R_0 is the linear coefficient and defines the slope of the saturation stress, ε_{pl} is the plastic strain, R_{inf} is the exponential coefficient, which is calculated as the difference between the initial and saturation stress, and b is the exponential saturation coefficient, which governs the rate at which saturation is achieved and material enters complete plasticity.

To determine the effect of the different modelling parameters on the response of the 1D models, a series of sensitivity studies were conducted. Through these sensitivity studies the optimal numerical settings configuration for each of the models was determined. Additionally, the relative importance of the different material properties on the response of the model was evaluated. It therefore became apparent, which material properties should be varied during the subsequent optimisation process to fit the mechanical response of the model to the experimental data.

Both the sensitivity studies as well as the optimisation of the model response were performed using Ansys OptiSlang v6.2.0 [3]. OptiSlang uses a quality measure named coefficient of prognosis (CoP) to evaluate the relative importance of the input variables and to optimise the selection of the metamodel of optimal prognosis (MOP) [4].

In the case of sensitivity studies, the CoP indicates the importance of the variable with respect to the solution quality. Higher CoP values denote that a variable is of high importance and thus has a higher effect on the model solution in comparison to a variable with a lower CoP. In the case of optimisation, the CoP is used to describe the predictive quality of the MOP. Higher CoP values indicate that the metamodel can be reliably used to explore the solution space, therefore avoiding time consuming FEM simulations. It is noteworthy that the MOP is multidimensional and the number of its dimensions corresponds to the number of variables optimised, including the error function used to determine the best fit.

Based on the sensitivity study results, it was decided to vary the following parameters for each 1D beam model:

- a) Annular cylinder model: The Voce material model parameters are parametrised.
- b) Cylinder model: The Voce material model parameters and the elastic modulus are parametrised.
- c) Combined model: The Voce material model parameters and the elastic modulus of the outer annular cylindrical beam and the elastic modulus, yield strength and tangent modulus of the inner cylindrical beam are parametrised.

An example of an MOP produced during the optimisation process of a model can be seen in Figure 4. Each simulation corresponds to one red point in the graph. For each simulation the error (result deviation from input data) is calculated as a function of σ_0 and R_{inf} . The “best fit” of each parameter corresponds to the simulation that has the smallest error value.

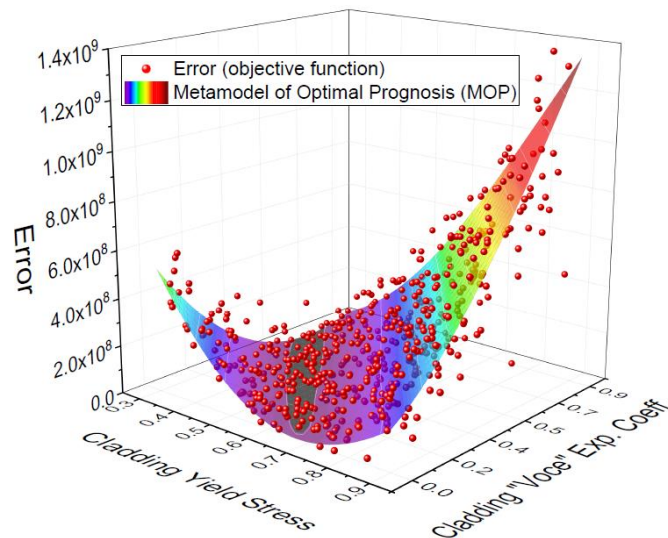


Figure 4 – Example of a MOP produced during the optimisation process. The error of each simulation is plotted against the most important parameters of the optimisation process (in this case σ_0 and R_{inf}). The best fit of each parameter corresponds to the simulation with the lowest error value.

3.1.3.3 Optimisation results and selection of best model

The 1D beam models of Figure 3 – are calibrated against the experimental force-displacement curves using experimental data corresponding to three different burnup (BU) values; 18.3 GWd/tHM, 46.9 GWd/tHM and 58.6 GWd/tHM, respectively. In Figure 5 the best-fit force-displacement curves of each model, based on the properties extracted from the optimisation process, are compared to the corresponding experimental data. For the annular cylinder and cylinder models results for all BUs are available whereas for the combined model, only results for the 18.3 GWd/tHM BU experiment are presented.

In the case of the annular cylinder model the elastic modulus is maintained the same as in the cladding of the 3D model. It has already been established that the elastic modulus of the 3D model follows the response of the fuel rod cladding [5,15]. Therefore, the annular cylinder model can be considered an empty cladding with modified plasticity parameters to account for the “lack” of pellets. In the case of the other two models, it is not possible to maintain the same elastic modulus.

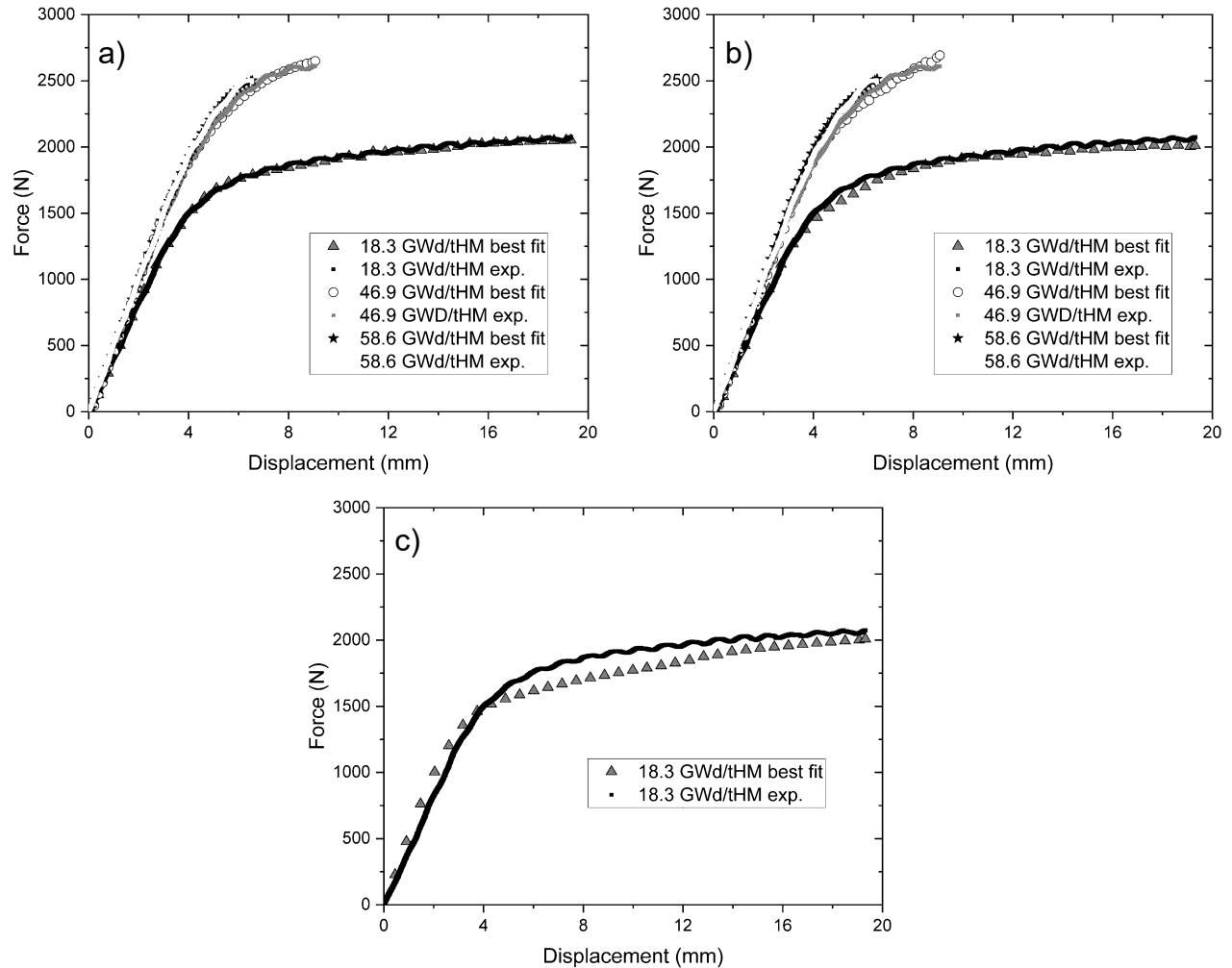


Figure 5 – Comparison between experimental force-displacement curves and best-fit curves of the 1D beam models, as derived from the optimisation process. a) Annular cylinder model, b) Cylinder model, c) Combined model.

Based on the results of Figure 5, one can derive that all models provide an acceptable fitting to the experimental force-displacement curves. Nevertheless, construction of larger scale assemblies will be based on a single model. Therefore, it is necessary to eliminate two of the three evaluated models.

Out of the three models, it is evident that the combined model provides a worse fitting compared to the other two. In addition to that, additional parameters need to be included in the optimisation process, thus leading to longer optimisation times with worse overall results and significant convergence issues. Individual simulations also required additional time to reach convergence compared to the other two models, mainly due to the increased number of interactions present in the model. Based on the above reasoning, it was thus decided to reject the combined model as a candidate for the modelling of larger scale assemblies.

When comparing the annular cylinder and cylinder models, it appears that the achieved fitting is of similar quality while both models require similar computational time to converge. Nonetheless, the annular cylinder model has a set of advantages compared to the cylinder model. The biggest advantage is the fact that the elastic properties of the cladding material can be directly assigned to the annular cylinder model. It is therefore not necessary to have an additional optimisation parameter, which cannot

be easily correlated to actual experimental data. Instead, one can simply use the experimentally derived Young’s modulus for the annular cylinder model. Additionally, overall, the annular cylinder model demonstrated lower-error values for all best-fit simulations when compared to the cylinder model.

Based on the analysis discussed above, it was decided that the annular cylinder model would be most reliable for the construction of larger scale assemblies. This would allow the direct correlation of elastic properties between experimental results and the FEM and would reduce the parameters necessary for optimisation. The values of the optimised parameters of the annular cylinder model for the different values of BU can be found in Table 6.

Burnup [GWd/tHM]	σ_0 [MPa]	R_0 [MPa]	R_{inf} [MPa]	b
18.3	450.0	1210.2	363.4	482.6
46.9	750.4	213.5	485.0	170.3
58.6	643.0	915.2	537.0	549.0

Table 6 – Best-fit values of the annular cylinder model parameters, as calculated from the optimisation process performed with OptiSlang.

3.1.4 Derivation of failure criteria

One of the goals of creating FEM of fuel rods is to be able to evaluate whether a rod has “failed” under a specific load. The failure of a rod can have different meanings depending on the requirements set forth by, e.g., the regulator during the transport of a fuel assembly, or the internal regulations of a nuclear facility, during handling of an assembly.

In previous modelling studies focusing on the loadings experienced by fuel rods during handling of fuel assemblies (e.g., during transport), fuel rods were assumed to fail after the YS value was exceeded. Therefore, in those cases, fuel rods that enter plasticity are assumed to “fail” and potential release of the fuel rod contents cannot be excluded as soon as plastic deformation occurs.

However, when evaluating the normalised stress and strain values of the annular cylinder beam model at the yield and failure points for different BUs, it is evident that this approach introduces a large amount of conservatism, since the yield stress and strains are significantly lower than the respective values at failure (Figure 6). Furthermore, based on the results of the same figure, it is evident that the assumption that failure occurs at the yield point is less conservative in the cases of higher BU values when using strain as a measure of failure. The reason for this is that for higher BUs, fuel rods become less ductile and therefore smaller plastic (and total) strain values are expected.

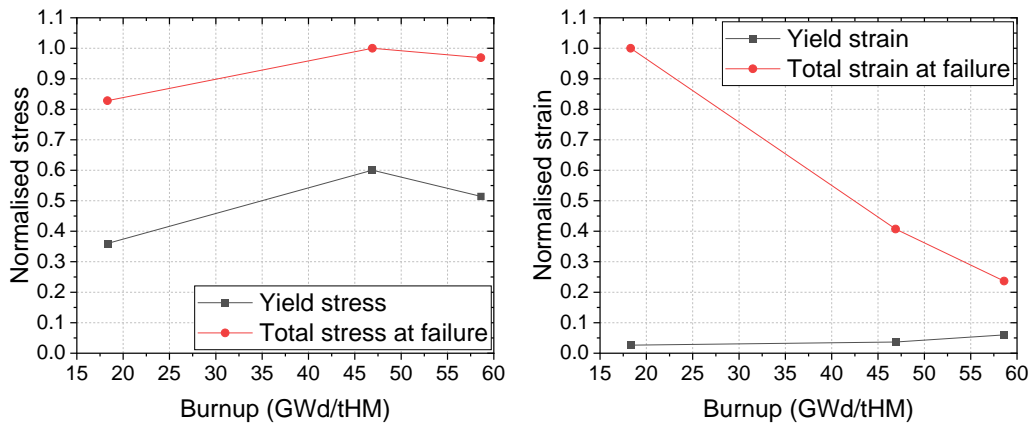


Figure 6 – Comparison of normalised stress (left) and strain (right) values at yield and at failure for different BU values.

The current study contributes significantly towards the understanding of past YS behaviour of fuel rods and specifically allows the derivation of failure criteria based on the experimentally defined point of failure, thus reducing the amount of conservatism. Through the optimisation process of the 1D beam models it is possible to correlate the total displacement of a sample to an accumulated (plastic) strain value.

The advantage of using strain for the derivation of failure criteria is two-fold. Firstly, the total strain to failure is easier to determine through experimental tests, by measuring the total change in length of a sample. Contrarily, stress cannot be easily defined in the plastic region, especially in samples with high ductility. Secondly, based on the results of Figure 6, the use of stress as a failure criterion leads to higher uncertainties regarding the determination of failure. The reason for this is that difference between the yield and failure stresses is not as significant as the difference between yield and failure strains. Specifically, failure stress is between approximately 1.7 and 2.3 times higher than yield stress for the different BU values. On the other hand, the total strain at failure is between approximately 4 and 40 times higher than yield strain for different BUs. Therefore, if a stress and a strain value are defined with the same relative error, the uncertainty of determining failure, using stress will be greater, since it will be more difficult to assess how far away from failure a component is.

In Table 7, the plastic and total strains recorded at the failure displacement of the annular cylinder beam model are presented for the different BU values simulated.

BU value (GWd/tHM)	1D beam plastic strain @ failure (%)	1D beam total strain @ failure (%)
18.3	18.30	19.49
46.9	6.74	7.94
58.6	3.44	4.61

Table 7 – Plastic strain at failure extracted for the different BU values corresponding to the material properties of Table 6, for the annular cylinder beam model.

It must be noted that the values of strain reported in Table 7 corresponds to the constructed 1D annular cylinder beam model and should not be used to define the actual rodlets that were subjected to the three-point bending test. The reason for this is that the 1D beam model contains a series of simplifications and assumptions that render it incomparable to an actual rodlet, such as the fact that in the 1D model local pellet-cladding interactions, which could lead to increased local stresses and strains, are ignored. Therefore, the extracted values should only be used to determine failure for 1D beam models with the same modelling approach and cannot be extended or correlated to other models or actual samples.

3.1.5 Transition to larger scale assemblies

After deciding on the optimal simplified 1D beam model to be used as a basis for larger scale assemblies and defining the fuel rod failure criteria, a stepwise approach towards creating larger scale models of PWR fuel assemblies was adopted. The goal of this approach was to determine the optimal numerical parameters to ensure proper interaction between assembly components, as well as reduce the computational effort of the created models.

It should be noted that from this point of the report and onwards, no experimental data that corresponds directly to each of the simulated scenarios exists. Therefore, the geometrical and mechanical properties of all beam models representing fuel rods are based on the mechanical properties of the annular cylinder model, as listed in Table 6. For other modelled components, such as guide tubes and most spacer grids, physical properties were inferred from mechanical tests on samples taken directly from irradiated guide tubes consisting of the material of interest. Additional material properties for other components (e.g., top and bottom end pieces) are based on literature and typically correspond to un-irradiated materials.

All simulation times mentioned below are based on simulations running on four physical cores of an Intel i9 10850K with 128GB DDR4, CAS 16 RAM running at 3000MHz.

3.1.5.1 Components of a spent fuel assembly

A PWR fuel assembly consists of the following main components (Figure 7):

- Fuel rods
- Spacer grids
- Guide tubes
- Top and bottom nozzles

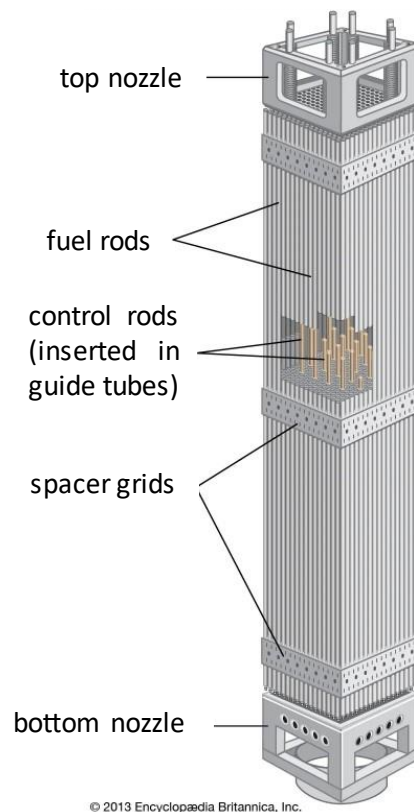


Figure 7 – Overview of basic components of a PWR fuel assembly. Original received from Encyclopaedia Britannica, Inc. [6].

The main skeleton of a PWR fuel assembly consists of the spacer grids and guide tubes. Each spacer grid consists of smaller rectangular cells in which fuel rods are inserted. Each of these cells contains a series of springs meant to keep the fuel rods in a fixed distance from each other and absorb small loads. Spacer grids are connected to guide tubes either by welding or through tight fit. The main purpose of guide tubes is to maintain the spacer grids at a fixed position and provide the structure of the assembly by being connected to the top and bottom nozzles. Additionally, control rods and other measurement instrumentation can be inserted through them to control and monitor the assembly during reactor operation.

To create a FEM of a fuel assembly it is mandatory that all basic components are implemented in the final model. As creating accurate models of each of these components would lead to a very complex and computationally intensive model, it is necessary to make simplifications during the modelling of each component.

3.1.5.2 Modelling of spacer grid springs

Spacer grid springs can be separated in two different types: springs and dimples. Both types behave as a spring, however, their stiffness varies. Springs are generally deformed easier and are used to hold fuel rods in place, while also allowing small movements to avoid deformation of the cladding. Dimples, on the other hand, are stiffer and are used to absorb larger loads and keep the fuel rods at a specific distance from the spacer grid cell walls. The shape of spacer grid springs and dimples can be found in Figure 8 whereas the configuration of springs and dimples in the developed models described in the next sections is found in Figure 9.

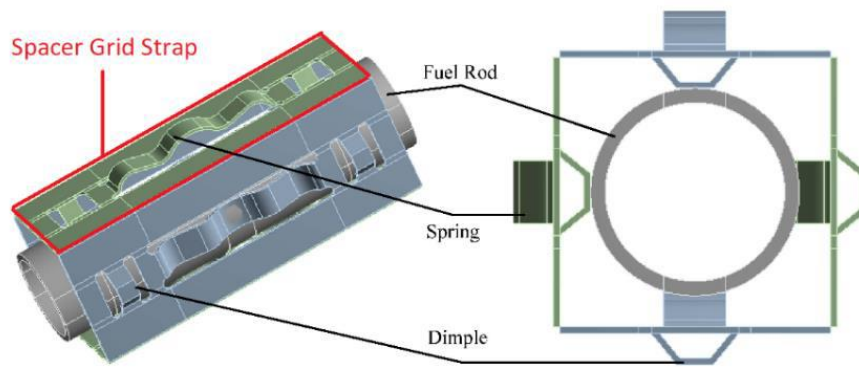


Figure 8 – Shape of spacer grid springs and dimples on an actual cladding (left: 3D view, right: lengthwise cross-section).

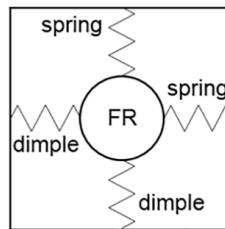


Figure 9 – Spring and dimple configuration of developed FEMs.

Based on Adkins et al. [7] the response of springs and dimples is non-linear. To achieve this non-linear response, it is necessary to input a force-displacement curve describing the spring element behaviour under different loads. The loading curves used for springs and dimples are those of Figure 10.

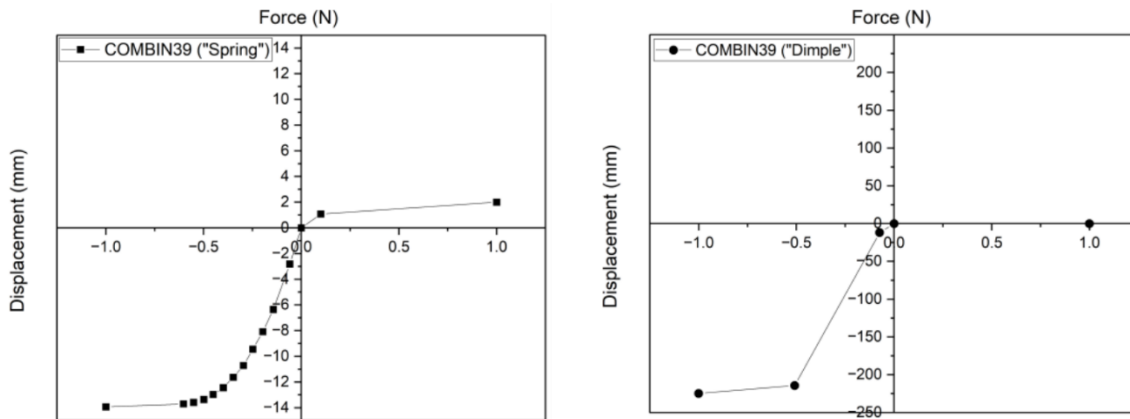


Figure 10 – Force-displacement curves describing the behaviour of springs (left side) and dimples (right side). This data is based on the report of Adkins et al. [7] and is used in the current FEM.

3.1.5.3 Preliminary evaluation of multiple component interactions and shell element-based spacer grid design

The first step towards large-scale models is to ensure that contacts between multiple simplified components (e.g., beam elements) can be correctly established and to determine an initial set of numerical parameters that would allow this.

For this reason, a 2x2 model was created, containing four fuel rods (annular cylindrical cross-section beam elements) and one spacer grid created using shell elements. Fuel rods are connected to spacer grids through springs, with the orientation and response of said springs corresponding to Figure 9 and Figure 10 respectively. The developed 2x2 model can be seen in Figure 11.

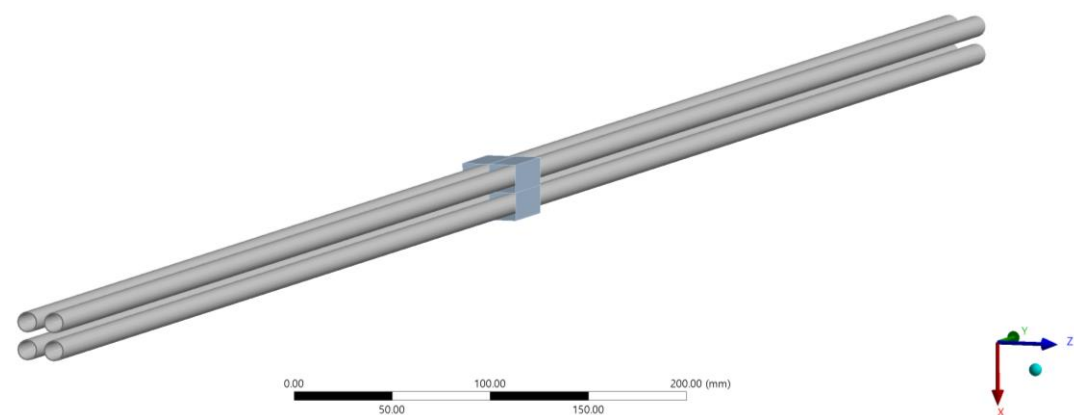


Figure 11 – Assembly consisting of four beams with an annular cylinder cross-section and a 2x2 spacer grid modelled using shell elements.

The model was subjected to a series of different loadings. Based on the results of the different simulations, it was made possible to determine the numerical parameters so that all necessary contacts (beam-to-beam(s), beam(s)-to-spacer) are correctly established and no significant penetration between components occurs.

The abovementioned tests act as proof that it is possible to simulate assemblies of multiple beams and that contact between multiple bodies at once is possible. In addition to that, the loading scenarios tested all converge within approximately 20 minutes or less, therefore meaning that expansion to even larger scale assemblies is feasible.

3.1.5.4 Spacer grid modelling approaches

Based on the analysis described in section 3.1.3 it was decided that fuel rods would be modelled as beams with an annular cylinder profile. However, so far only one spacer grid modelling option has been evaluated: that of using shell FEs to represent spacer grids (section 3.1.5.3). Apart from shell-based spacer grids it would also be possible to create spacer grids based on beam FEs. The difference between the beam elements used to simulate fuel rods and those used to simulate spacer grids is the cross-section of the beam. Based on studies performed by Klymyshyn et. al. [8], spacer grids modelled using beam elements can better reproduce the bending behaviour of the spacer grid itself, compared to ones using shell elements. It was therefore decided to create a beam element spacer grid model and test its response under different loadings. The model used for these studies contains twenty-five fuel rods constructed using beam elements with an annular cylinder profile and a 5x5 spacer grid constructed using beams with a rectangular cross-section profile (Figure 12). Fuel rods are connected to the spacer grid using spring elements with the parameters described in section 3.1.5.2.

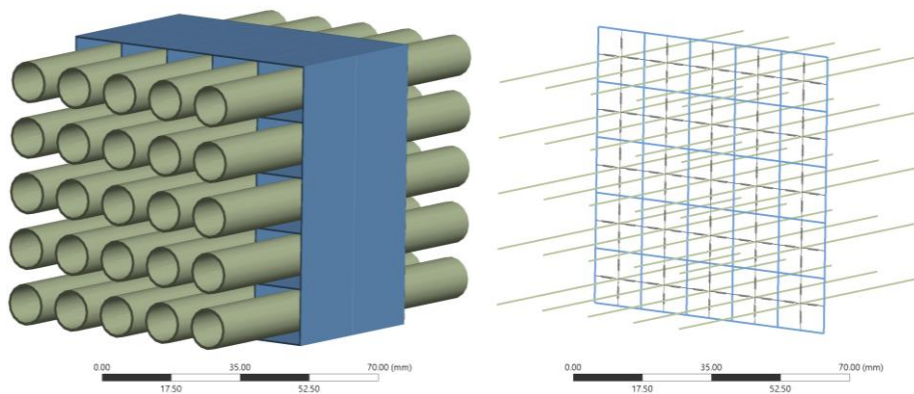


Figure 12 – FEM of a 5x5 spacer grid consisting of beam elements with a rectangular profile and 25 fuel rods consisting of beam elements with an annular cylinder profile. On the left side is the model with cross-sections visible whereas on the right side is the same model with cross-sections turned-off.

The model of Figure 12 was subjected both to a crushing load, with a force acting on the top side of the model, as well as to a bending load, with a force acting at the end points of fuel rods. In the crushing load simulation, the spacer grid deforms and comes into contact with the fuel rods, as would be expected. However, in the case of the bending load applied on the beams, the contact between spacer grid and fuel rods is not established correctly. Specifically, the fuel rods appear to penetrate the spacer grid edges while bending. The reason for this behaviour is linked to how contacts between beam elements are defined in Ansys®. The description of the issue is out of the scope of the current report; nevertheless, additional information can be found in the Ansys® Mechanical APDL manual [9], specifically when examining the CONTA177 element type information regarding contact cylinder radii.

Therefore, when simulating loadings such as horizontal drop tests or crushing of fuel assemblies it might be more accurate to use beam elements for the spacer grids to better capture their bending behaviour. Nonetheless, when bending forces are applied to fuel rods, spacer grids are not expected to be significantly deformed and thus, the spacer grid models based on shell elements should be sufficient to model such cases. Taking into account the above and considering the fact that the material properties of fuel rods in the simplified model are based on three-point bending test experimental data, thus making them more suitable for bending scenario simulations, it was decided that for the models described in this report shell element spacer grids would be used.

3.1.5.5 Implementation of guide tubes and top and bottom nozzles

After evaluating the different modelling approaches for spacer grids and fuel rods, it was decided to create a small-scale assembly containing all basic components of a fuel assembly. Therefore, a 3x3 model containing eight fuel rods, one guide tube (also modelled as a beam with an annular cylindrical cross-section), three shell spacer grids and one top and bottom nozzle respectively was created. The guide tube outer diameter is the same as the inner size of the spacer grid cell and is bonded to the cell walls. Further, top and bottom edge pieces are represented as surfaces modelled with shell elements and have a hole through which the guide tube fits. The guide tube is bonded to the edges of the nozzles as well. The material properties of low BU (18.3 GWd/tHM, Table 6) were assigned to the fuel rods.

Since the developed model presented a plain of symmetry at the ZX plane (see Figure 13 for axis orientation) it was decided to leverage this symmetry to reduce the required computational time. Therefore a “half-symmetric” model was developed. Both the “full” and half-symmetric models can be seen in Figure 13.

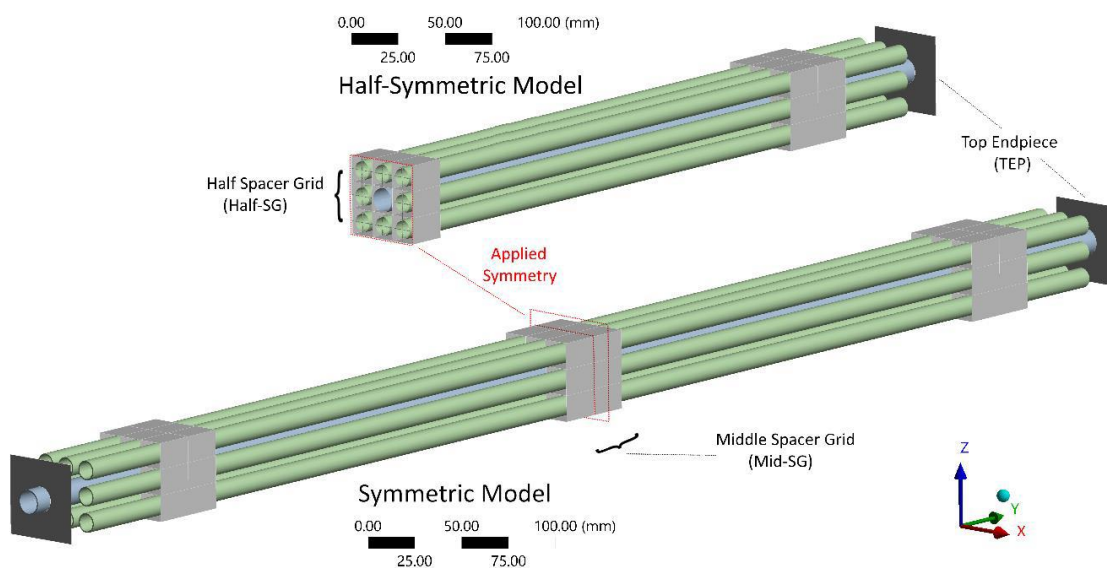


Figure 13 – Full and half-symmetric 3x3 model. The model contains all the basic components of a fuel assembly.

As the developed model contains all main components of a full-scale assembly, it was decided to use it as a basis for performing a series of sensitivity studies. These studies are performed for a series of numerical (e.g., contact settings), physical (e.g., spacer grid springs and dimples response under loading) and material (e.g., mechanical properties of guide tube and spacer grids) parameters. The goal is to determine the effect each parameter has on the response of the model and of individual components, so that the correct parameters can be selected for modelling different scenarios, especially in case experimental data for different fuel assembly loadings become available in the future. For each performed study, data relevant to the response of individual components was collected (e.g., strain and stress values of individual beams), while the total assembly response was also evaluated. The detailed analysis for all evaluated parameters is out of the scope of this report but can nevertheless be found in [10]. In section 3.1.5.6, the sensitivity study performed on springs and dimples response under loading is briefly presented.

3.1.5.6 Sensitivity analysis of individual modelling parameters – Effect of non-linear springs on total model response.

The effect different parameters have on the response of the model is evaluated under a bending scenario similar to a three-point bending test. Specifically, a displacement load is applied at the top side of the middle spacer grid on the half-symmetric model, pushing it downwards, while the other two spacer grids are constrained from moving. This loading differs from a three-point bending since in this case the edge spacer grids are fixed and not simply supported. Based on these boundary conditions, the reaction force is extracted from the surfaces where the displacement is applied.

To evaluate the effect that non-linear springs and dimples have on the model results, two edge cases were modelled. In the first case, the springs and dimples are modelled with a linear response and their longitudinal stiffness is set to 1 N/mm. In the second case, the response of springs and dimples is governed by the force-displacement curves of Figure 10.

The model with the linear spring definitions showed a much better convergence behaviour compared to the one with non-linear. To facilitate the convergence of the non-linear spring model, it was decided to increase the number of simulation “sub-steps”, thus decreasing the rate at which loads are applied. In

the end, the non-linear model achieved the same convergence as the linear one, although it required approximately 20% additional simulation time to do so. The overall model force-displacement behaviour for each case is presented in Figure 14.

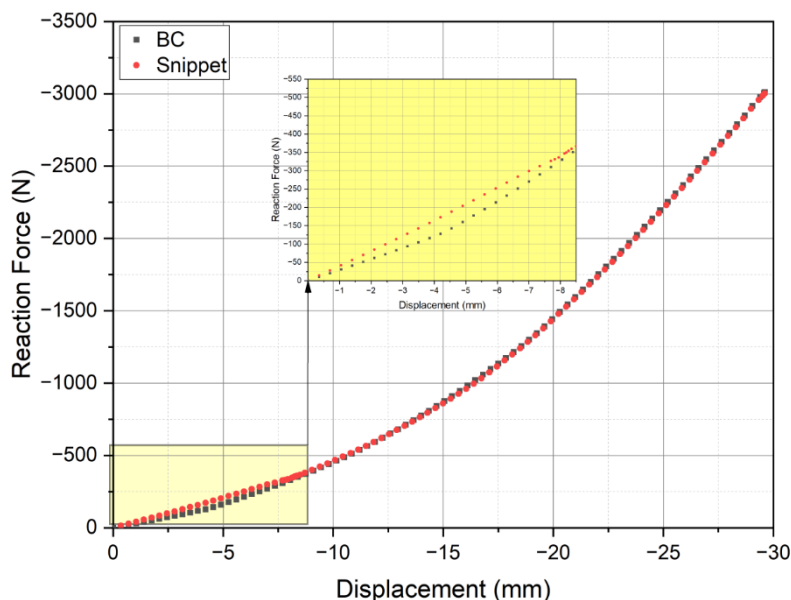


Figure 14 – Force-displacement behaviour of the model in the case of linear spring definition (black points - “BC” curve) and non-linear spring definition (red points – “Snippet” curve).

Observing the results in Figure 14 it can be easily seen that a small variation between the two curves is found at lower displacements, until approximately a displacement of 8 mm. Beyond that point the two curves almost completely align. The reason for this is that at smaller displacements the main forces applied on the model originate from two sources: from the stiffness of the different components (fuel rods, guide tubes, etc.) being deformed under the applied displacement and from the springs and dimples of the spacer grids. Since the non-linear spring elements exhibit higher forces during initial deformation compared to linear ones, it is expected that in these smaller displacements the total reaction force of the model will be bigger due to these springs. However, as the displacement of the model increases, a series of contacts (rod-to-guide tube, rod-to-grid) start developing while the reaction force from the deformation of different model components keeps increasing. At this point, these forces occurring from contacts and the stiffness of individual components largely dominate the reaction force of the model. Consequently, the difference between the two curves becomes insignificant as the applied displacement increases.

Based on the reasoning above, it is safe to assume that simplifying the design of spring elements should not significantly affect the total response of the current, lower BU, model. This is especially true when bending loadings leading to big deformations are applied and multiple contacts between different model components occur.

In the case of higher BUs, the total displacement until the model reaches its failure point is significantly smaller than the low BU model. It would therefore be expected that the contact forces developed between the different components would be smaller. On the other hand, due to the increased strength demonstrated by higher BU fuel rods, the overall forces applied by them would be increased even at smaller deformations. Therefore, in the case of higher BU values further studies would be required to evaluate the effect simplified springs have on the total model response.

3.1.5.7 Spent fuel sub-assembly response investigation

After determining the effect of different modelling parameters on the response of the model, it was decided to create a 15x15 PWR sub-assembly model. This model was used to evaluate the necessary simulation time, as well as investigate how a model of such scale would respond under a bending loading.

The developed 15x15 sub-model consists of twenty guide tubes, four spacer grids and one top and bottom nozzle, respectively. The modelling approach and connections between components are the same as in the smaller scale model of Figure 13. Furthermore, the simulation parameters were defined with the goal to minimise the simulation time while making sure that contacts between components are correctly established. Spacer grid springs and dimples were modelled using the force-displacement curves of Figure 10 while the fuel rods were assigned the material properties of the *lowest BU* (Table 6). The non-deformed model can be seen in Figure 15.

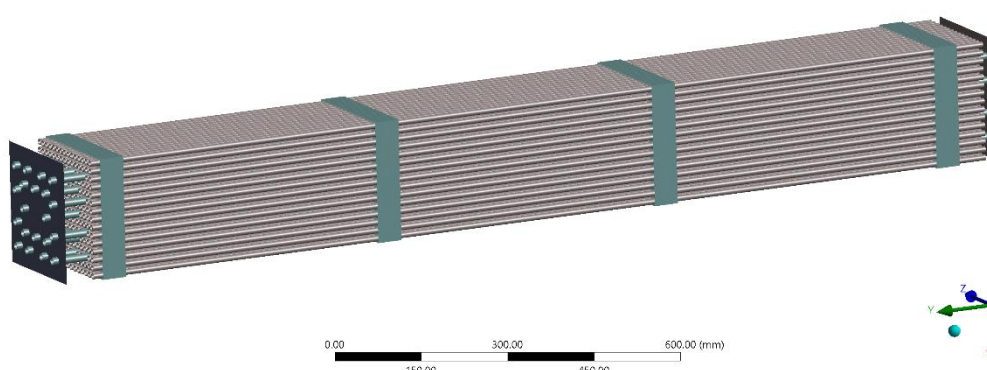


Figure 15 – FEM of a 15x15 spent-fuel sub-assembly. The model consists of 205 fuel rods, 20 guide tubes, 4 spacer grids and 1 top and bottom end piece respectively.

Out of all the models described so far, this model is expected to best represent the response of an actual fuel assembly under a bending load, as it is essentially a shorter version of a full-scale assembly. It is subsequently subjected to two different bending loading scenarios. The first loading is based on that described in the paper of Guerin et al. [11]. Specifically, all spacer grids except the first one were constrained from moving. Additionally, an “obstacle” (zero displacement constraint) was placed at 1/3 of the distance between the first and second spacer grid (closer to the second spacer), thus preventing the fuel rods from moving further. Finally, a displacement was applied at the top nozzle. The second loading is different from the first one only in a single aspect; the “obstacle” is removed. The deformed shape of the model in both cases can be seen in Figure 16 whereas the position where the maximum fuel rod strain is found in each bending scenario is found in Figure 17. It should be noted that the strain results of Figure 17 are considered preliminary.

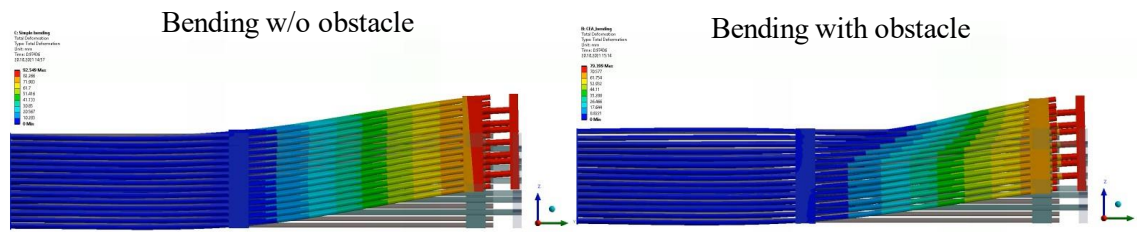


Figure 16 – Deformed shape of 15x15 FEM of a spent-fuel sub-assembly under two different bending loads applied at the top end piece. On the right-hand side, an obstacle (zero displacement constraint) is positioned at 1/3rd of the distance between the first and second spacer grids. The un-deformed shape of the model can also be seen in each case. The colour scale corresponds to the displacement of each model component.

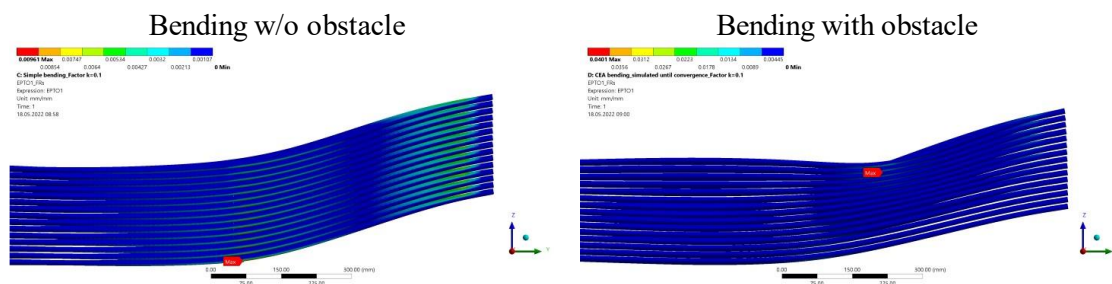


Figure 17 – Deformed shape of fuel rods of a 15x15 FEM of a spent-fuel sub-assembly under two different bending loads applied at the top end piece. On the right-hand side, an obstacle (zero displacement constraint) is positioned at 1/3rd of the distance between the first and second spacer grids whereas in the left-hand side there is no obstacle. The colour scale refers to the principal total strain, although strain results are preliminary. The maximum strain location is depicted using a red label.

Based on the results of Figure 17, the location of the maximum strain of the fuel rods changes based on the simulated loading scenario. Additionally, in the scenario where an obstacle is modelled, the maximum strain is approximately four times higher than the strain in the case where no obstacle is present, while the total simulated displacement in the case with an obstacle is approximately 20% less than the other case. Therefore, based on the simulation results, a loading with an obstacle would pose a higher risk of fuel rod rupture compared to a normal bending loading.

3.1.5.8 Full-scale spent fuel assembly model

The final step in the model creation process is the full-scale assembly FEM. The model of section 3.1.5.7 was extended and four additional spacer grids were added so that the size of the model matches that of an actual fuel assembly. The modelling approach of all components as well as the settings of the simulation parameters are the same as the model of section 3.1.5.7. The un-deformed model can be seen in Figure 18.

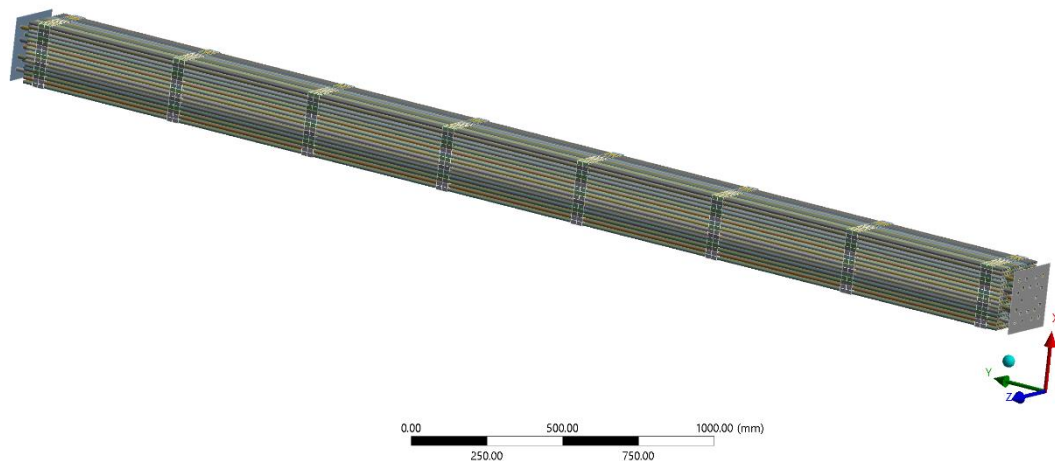


Figure 18 – Full-scale FEM of a PWR spent fuel assembly. The model consists of 8 spacer grids 205 fuel rods, 20 guide tubes and 1 top and bottom end piece respectively.

3.1.6 Full-scale model – Challenges and analysis results

The transition to a full-scale model and its subsequent analysis were not an easy undertaking, mainly due to the size of the model, which caused issues with the graphical user interface (GUI) of Ansys®. To address some of these issues a series of scripts were developed, mainly focusing on extraction of results. Below the different challenges as well as the extracted results of the full-scale model are presented.

3.1.6.1 Challenges associated with the full-scale model

The creation of the full-scale model is unfortunately not automated, thus meaning that a large number of contacts and parameters need to be defined manually. Hence, a significant time-investment from the side of the user is necessary to create a FEM of a full-scale assembly, from the initial CAD model to the final FEM with all contacts and boundary conditions defined. In total, more than 15 hours of “manual” work were required to create the CAD model, define all necessary interactions between model components and set the necessary simulation parameters.

Apart from the large time investment to define contacts and simulation settings, the full-scale model is also very hard to manipulate since the Ansys® GUI is very slow to respond whenever a new item is selected. This behaviour becomes worse as the number of specified interactions, elements and components increases and was already an issue with the model described in section 3.1.5.7. Moreover, creating new graphs or result sets is also a very time-consuming process, not only due to the slow GUI, but also due to the long time required to perform any post-processing actions.

Apart from the modelling difficulties, interpreting the results of the full-scale model is also troublesome. Since the size of the model corresponds to an actual full-scale SFA, there are no direct experimental data, at least corresponding to scenarios similar to the ones modelled here, which could be used to compare the results of the model to. Therefore, the results extracted from this model should be considered as estimates and should be used mainly as guidance to identify problematic regions during simulated loadings or for the planning of experimental campaigns.

3.1.6.2 Simulated loading scenario

The model of Figure 18 was subject to the “bending without obstacle” loading described in section 3.1.5.7 and seen on the left side of Figure 16. This selection of the loading scenario is based on the fact that in this case fuel rods are subjected mainly to bending loads. Since the 1D beam models were calibrated using three-point bending experimental data, the results of this loading would be expected to represent the behaviour of fuel rods more accurately. The material properties of the fuel rod components correspond to the low BU material properties of Table 6, effectively simulating the response of a spent fuel assembly with a low BU. A comparison between the deformed and un-deformed shape of the model can be seen in Figure 19. The colour scale in this figure corresponds to the displacement of different model components.

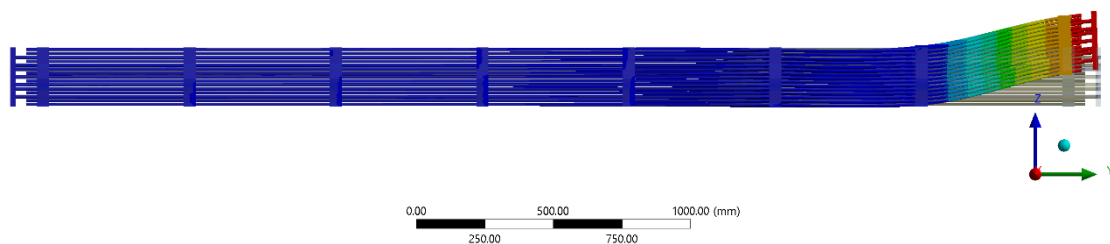


Figure 19 – Comparison between the deformed and un-deformed shape of the full-scale model. The colour scale corresponds to the displacement on the different components of the assembly. Red corresponds to higher displacement values whereas dark blue to lower.

The maximum displacement achieved by the model before the simulation is unable to converge is approximately 140 mm. It is assumed that further adjustment of the boundary conditions and density of FEs on different components could lead to increased convergence of the model.

As can be seen from the results of Figure 19, the displacement of the top nozzle appears to be affecting components up to the fourth spacer grid, although displacements in that region are very small. It would therefore be expected that the highest loadings would be expected closest to the region where the displacement load is applied. Additionally, one could use a sub-assembly model containing less spacer grids to evaluate the response of the different components at the regions where the loading is highest. This would in turn save both modelling and simulation time and make evaluation of results easier. However, before determining the optimal size of the sub-model, additional results should first be evaluated.

3.1.6.3 Simulation results

For the full-scale model described above, results were extracted using a series of automation scripts, thus significantly reducing the post-processing time of the model. These results provide insights to the response of the individual model components under the described bending load and can be used to evaluate their response and assist in planning future experimental campaigns, which would in turn lead to the better understanding of the assembly response.

Using the automation scripts, a series of results that can assist in the determination of whether a fuel rod has failed can be extracted. In the simplest case, where failure occurs after a fuel rod exceeds its yield stress, two outputs are necessary to identify rods that have failed. The first output is the number of rods exceeding their yield stress value for each displacement and the second one is the location of each of these rods.

The number of beams exceeding their yield stress value for each time step in the current model, based on the applied boundary conditions, can be seen in Figure 20. Two distinct regions can be identified in this graph. The first plateau (between approximately 75 mm and 113 mm of displacement) is created by the guide tubes, which enter the plasticity regime first. After approximately 113 mm of displacement, a constant increase in the number of beams entering plasticity is observed: these are the fuel rods entering plasticity, whose number increases with the displacement of the model. This graph is accompanied by a series of tables, one for each time step, in which the position of the rods exceeding their yield stress is shown by a Boolean parameter. If the value is 0, then the rod is still within the elastic region, whereas when the value is 1, the rod has entered plasticity and is subsequently assumed to have “failed”. A representation of such a table can be seen in the picture embedded in Figure 20, where the beams already in plasticity (in this case, all guide tubes) are marked in red.

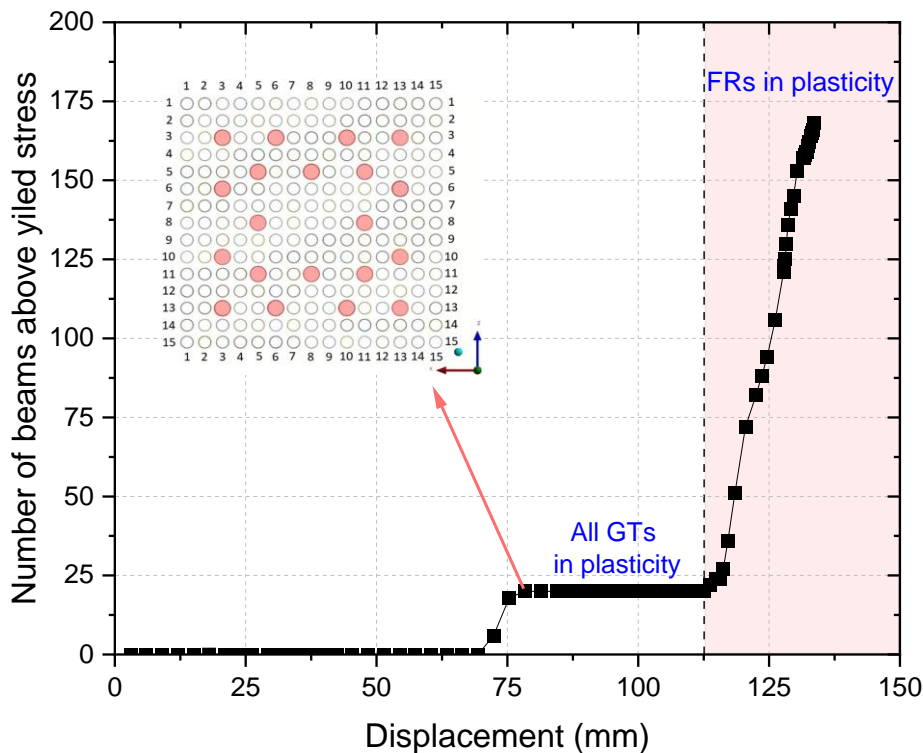


Figure 20 – Number of fuel rods that have exceeded their yield stress value based on the applied displacement.

To reduce conservatism, one could use the total (plastic) strain defined at maximum displacement before failure occurs, instead of the yield stress/strain. Based on this failure criterion, it would be expected that the number of failures in an assembly would be significantly reduced, especially for lower BU values.

In this scenario, the results of Figure 20 are no longer sufficient to determine whether a rod has failed. For this reason, the time and location of the maximum plastic strain is output for each fuel rod. These results are subsequently compared to the derived failure criteria of Table 7 and based on the outcome of the comparison the number of rods exceeding the defined (plastic) strain limit can be identified for each loading scenario. For the loading scenario investigated in the current report, the plastic strain experienced between the different fuel rods and the guide tubes is visualised in Figure 21. The plastic

strain results are normalised using the maximum observed plastic strain values on fuel rods. The orientation of the assembly corresponds to that of the embedded picture in Figure 20.

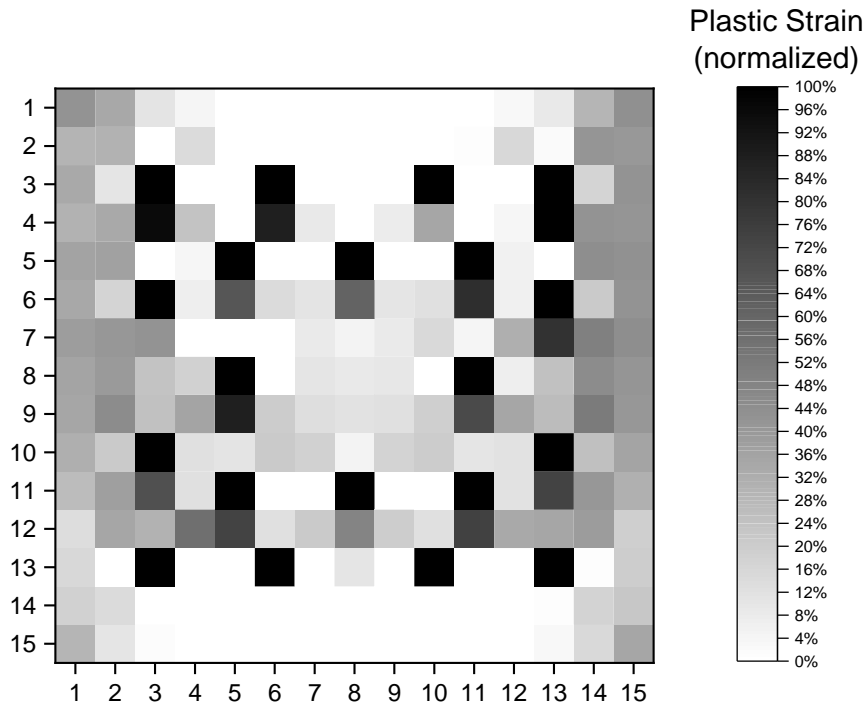


Figure 21 – 15x15 grid showing the principal plastic strain of each beam of the full-scale model for the loading scenario described in section 5.2. The values of the plastic strain are normalised using the maximum observed plastic strain on fuel rods. Therefore, the guide tubes, which exceed this maximum strain value, appear as completely black in the current representation. The layout of the assembly matches that of Figure 20.

Based on the results of Figure 21, it is evident that the components experiencing the highest loading are the guide tubes, which also demonstrate strain values significantly higher than those of the fuel rods. This is also the reason that guide tubes appear as completely black in this figure, as their maximum strain value far exceeds that of fuel rods and therefore the scale of the graph. Moreover, a significant portion of fuel rods appear to not have or barely have entered plasticity whereas the maximum value of plastic strain on fuel rods is observed at the rods found directly below the guide tubes. Nevertheless, the actual plastic strain values of fuel rods are significantly lower than the failure plastic strain listed in Table 7 for the low BU case. It must, however, be noted that the current results are only preliminary and that in order to ensure their accuracy, they should be compared to experimental data. Furthermore, the failure values of Table 7 correspond only to fuel rods, thus meaning that in the current investigation the failure of guide tubes, which could subsequently lead to additional loadings on fuel rods, was not evaluated.

Finally, it is also possible to visualise the loading of specific fuel rods at selected time steps by extracting the Shear Force and Bending Moment diagrams of the rod. In Figure 22 the Shear Force and Bending Moment diagrams of the rod in position (1,1) (numbering based on Figure 20 and Figure 21) can be found.

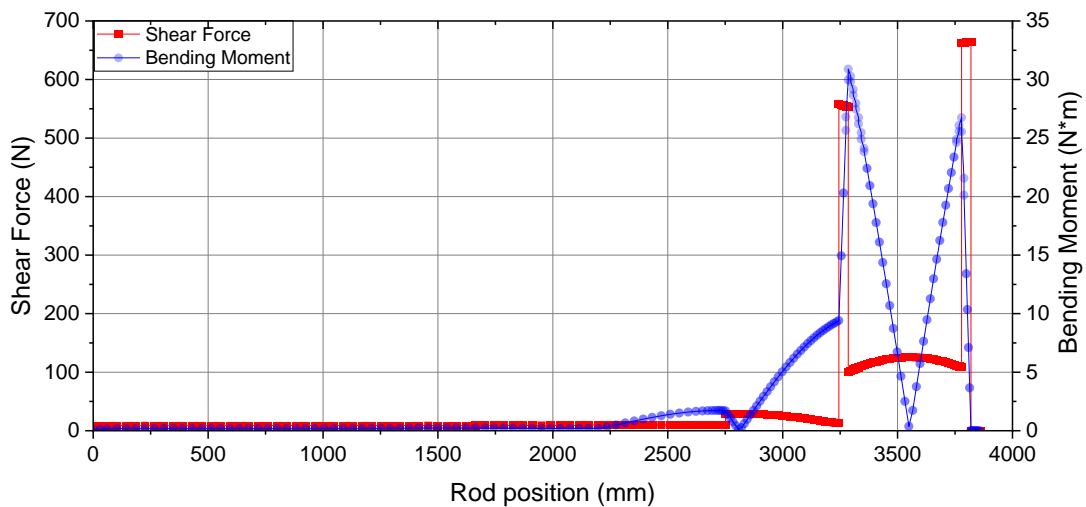


Figure 22 – Shear force and bending moment diagram along the length of the beam at position (1,1), at the last converged time step of the simulation. The right vertical axis corresponds to the bending moment whereas the left vertical axis corresponds to the shear force. The 0 position of the rod is specified at the side of the fuel assembly where no loading is applied.

Based on the results of Figure 22, the maximum shear forces and bending moments are registered at the locations where the fuel rod contacts the first and second spacer grids. From the third spacer grid and onwards, the forces and moments applied on the rod appear to diminish significantly. Therefore, any potential failure would be expected to be closer to the side where the loading is applied on the fuel assembly and most likely at the locations where the fuel rods are in contact with the spacer grids.

This argument is also supported by the results of Figure 23, where the stress is visualised on fuel rods and spacer grids. Higher stresses on fuel rods are observed closer to the locations of the first and second spacer grids, whereas the rod stresses from the third spacer grid and onwards (out of frame) is significantly lower.

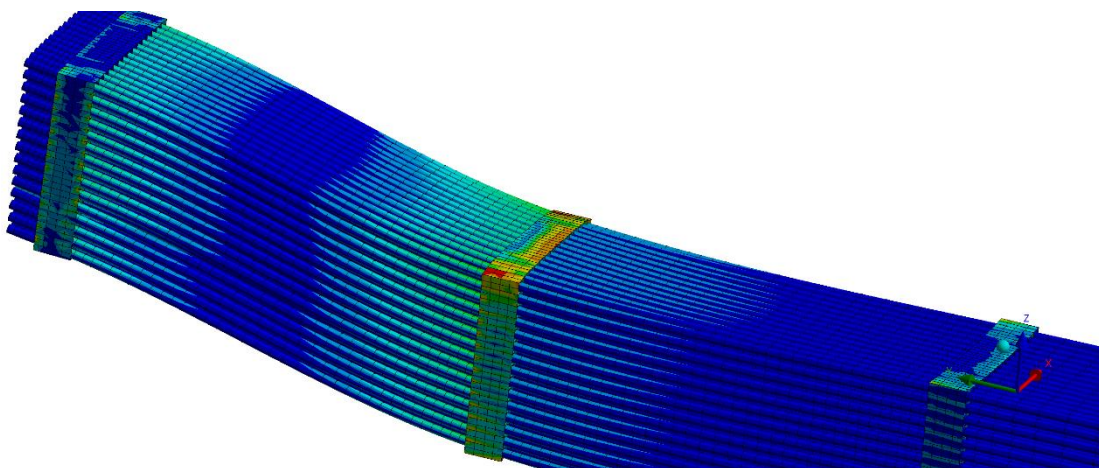


Figure 23 – Side view of the full-scale model showing the developed stress on fuel rods and spacer grids at the maximum modelled displacement. Blue colour corresponds to lower stresses whereas red colour corresponds higher stresses. The guide tubes and top nozzle are hidden but their effects have nevertheless been considered in these results.

The results of Figure 22 and Figure 23 also confirm the hypothesis made in section 3.1.6.2 that mainly the components closest to where the loading is applied are affected by the load. Therefore, based on these figures, one could theoretically evaluate the response of a full-scale model under the same loading by modelling a smaller-scale model. Such an approach would save a significant amount of computational and modelling time, although this assumption should first be tested to evaluate its correctness.

3.1.7 Conclusion and outlook

In the current report, the transition from small scale rodlet modelling towards full-scale fuel-assembly models was discussed. Specifically, it has been shown that it is possible to correctly simulate experimental data of three-point bending tests using a simplified model approach, with the optimal modelling approach being that of a 1D beam model with an annular-cylindrical cross-section. Based on this simplified model, it was demonstrated that it is possible to determine the failure of fuel rods and subsequently build larger scale assembly FEMs, even reaching the size of a full-scale fuel-assembly.

Based on the three-point bending test simulation results of the 1D beam model, it was possible to define the total and plastic strain to failure for each simulation, which represented a different rod segment with different average burnup. This value can subsequently be used as a failure criterion for fuel rods in larger-scale models. This significantly reduces the amount of conservatism compared to cases where failure was assumed to occur when the yield stress was reached. Additionally, the use of strain instead of stress for the determination of failure allows easier correlation between experimental and simulation data and leads to lower uncertainties with regards to the determination of how far a rod is from its point of failure.

Although the modelling of a full-scale assembly has proven to be a viable, the modelling process is plagued by issues relevant to the GUI responsiveness, mainly due to the very high number of modelled components and their complex interactions. Nevertheless, the created model was used for simulating a bending scenario, which has provided valuable insight regarding the total response of the model under loading and the load distribution between the different components of the assembly. More specific, guide tubes appear to be withstanding the highest loads whereas fuel rods appear to barely enter plasticity.

A series of automation scripts were also developed to allow easier extraction and post-processing of the model results. Nevertheless, to allow for easier modifications of the model in the future, it would be beneficial to automate the model creation process as well. Such automation would lead to reduced hands-on time from the side of the user and would enable the simulation of multiple different loading scenarios and the evaluation of different modelling approaches. Additionally, it should also be tested whether the creation of full-scale models is necessary for different loading scenarios, as the preliminary analysis of the full-scale model has shown that loadings mainly affect the region closest to them and components further away are not significantly loaded (if at all).

An additional improvement in the current modelling approach would also be to assign variable material properties along the length of the fuel assembly. Based on the results of previous analysis [12–14], it has been shown the middle part of the assembly is irradiated at a higher rate compared to its edges, therefore meaning that the BU in the middle section of fuel rods would be expected to be higher. This would affect how the model responds depending on which sections of the model are loaded and would thus make the model more realistic.

Finally, it is noteworthy that the creation of fuel-assembly FEMs is not a substitute for experiments. Nonetheless, FEMs can serve as a guide towards which regions of the assembly should be evaluated and which tests would provide useful data. Consequently, the combination of experimental data and the created FEMs can be used for identifying problematic regions during different loadings and estimating whether failure of fuel rods is likely.

3.2 References

- [1] Ansys® *Professional, Release 2021 R1*.
- [2] Michele Bellotti, "Towards beam modelling for static structural analysis of spent nuclear fuel rods," Master's dissertation, EPFL, Lausanne, 2020.
- [3] Ansys® *OptiSlang, v6.2.0*.
- [4] T. Most and J. Will, Eds., *Sensitivity analysis using the Metamodel of Optimal Prognosis*, 2011.
- [5] E. Vlassopoulos, "Structural performance and mechanical properties investigation of spent nuclear fuel rods under static and dynamic bending loads," EPFL, Switzerland, 2021.
- [6] Encyclopedia Britannica, Inc., *Nuclear fuel assembly for a pressurised-water reactor*. [Online]. Available: <https://www.britannica.com/technology/nuclear-reactor/History-of-reactor-development> (accessed: Feb. 15 2024).
- [7] H. Adkins *et al.*, "Used Nuclear Fuel Loading and Structural Performance Under Normal Conditions of Transport - Demonstration of Approach and Results on Used Fuel Performance Characterisation: Used fuel disposition campaign," Fuel Cycle Research & Development, U.S. Department of Energy, Sep. 2013.
- [8] N. Klymyshyn, K. Kadooka, P. Ivanusa, C. Spitz, and J. Fitzpatrick, "30 cm Drop Modeling," 2020.
- [9] Ansys® *Professional, Release 2021 R1: Help System, Ansys® Mechanical APDL, Chapter 7: Element Library, CONTA177*: ANSYS, Inc.
- [10] M. Hadjigeorgiou, "Sensitivity studies on the structural response of a PWR spent fuel sub-assembly using finite element modelling," Master's dissertation, EPFL, Lausanne, 2022.
- [11] C. Guerin *et al.*, "CAST3M modelling of a spent fuel assembly bending during a handling accident. Rod failure risk evaluation from the experimental results of spent fuel rod bending test," *Mechanics & Industry*, vol. 15, no. 4, pp. 301–305, 2014, doi: 10.1051/meca/2014031.
- [12] V. F. Castro, R. Miró, C. Pereira, and G. Verdú, "A burnup credit methodology for PWR spent fuel storage pools: Application to a standard PWR nuclear power plant," *Nuclear Engineering and Design*, vol. 419, 2024, doi: 10.1016/j.nucengdes.2024.112948.
- [13] J. C. Wagner, M. D. DeHart, and C. V. Parks, "Recommendations for Addressing Axial Burnup in PWR Burnup Credit Analyses - NUREG/CR-6801, ORNL/TM-2001/273," U.S. Nuclear Regulatory Commission, Mar. 2003.
- [14] J. C. Wagner and M. D. DeHart, "Review of Axial Burnup Distribution Considerations for Burnup Credit Calculations - ORNL/TM-1999/246," Oak Ridge National Laboratory, Mar. 2000.
- [15] EURAD Deliverable n° 8.8 - Thermo-mechanical-chemical properties of unirradiated and irradiated samples of spent nuclear fuel rod segments and cladding, 2024

4. Development of a stochastic approach to determine probability of fuel rod cladding failure under accident scenarios

4.1 Introduction

During the storage and transport of spent nuclear fuel until its final disposal, it is of utmost importance to accurately predict its behaviour, both in nominal conditions and possible accident scenarios, in order to ensure that the safety functions are fulfilled [1]. As the first engineering barrier of radioactive materials, cladding integrity and degradation becomes the ultimate goal of such assessments.

EURAD's Spent Fuel Characterisation work-package (SFC), aims at understanding spent fuel performance until its final disposition in a deep geological repository [2]. To meet this goal both analytical and experimental studies have been conducted.

This section describes a methodology to estimate cladding failure probability of Spent Nuclear Fuel (SNF) in a postulated accident scenario. This methodology is based on three main elements: FRAPCON-xt [3], HYDCLAD [4] and DAKOTA [5]. The former is an in-house extension of FRAPCON to dry storage carried out by CIEMAT. The second is a CIEMAT model to estimate across-cladding hydrogen distribution and precipitation. The last one is a multi-purpose statistical toolbox developed by SNL. By articulating these three elements, a fast estimate of fuel rods integrity is estimated without requiring highly-demanding computational, which would rely on highly uncertain boundary conditions.

4.2 Methodology

4.2.1 Approach

The methodology approach is based on three pillars:

- The thermo-mechanical characterisation of the fuel rod (particularly the cladding) right at the onset of the accident. This relies on a fuel performance code calibrated to obtain more accurate predictions of the variables that may have an important impact on the spent fuel behaviour during the storage stage [6].
- The cladding response under the accidental conditions. This is modelled through cladding mechanical properties and failure criteria (i.e., threshold to the Figure of Merit considered, FOM) valid under the prevailing conditions (section 4.2.2 and 4.2.3). This entails an extension of the fuel performance code.
- The extension of the analysis to cladding failure probability. It is based on a statistical analysis from input variabilities imposed (section 4.2.4).

Figure 24 sketches this approach, highlighting how crossing the statistical analysis (using maximum cladding stress as the Figure Of Merit, FOM) with the failure criterion results in a failure probability. The threshold has been taken conservatively from a critical review of the open literature available.

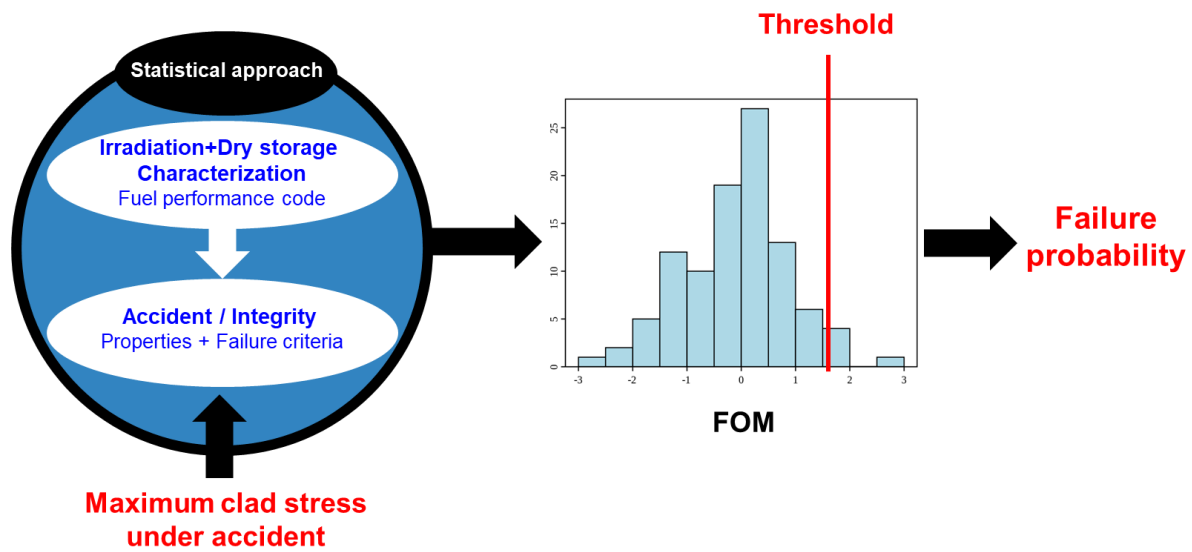


Figure 24 – General diagram of the methodology.

The code used for the fuel performance simulation under irradiation and dry storage conditions is FRAPCON-xt [7]. It is a CIEMAT’s extension to dry storage conditions of the steady-state fuel performance code FRAPCON, developed by Pacific Northwest National Laboratory (PNNL) for the US Nuclear Regulatory Commission [8]. Additionally, the methodology encompasses the modelling of the hydrides distribution and reorientation within the cladding from the coupling with FRAPCON-xt of the HYDCLAD CIEMAT’s model [3], [4].

It should be noted that FRAPCON-xt has been supplemented with an extension of its predictive capability of Rod Internal Pressure (RIP) beyond 60 GWd/tU, in case burn-ups are extended in future (FRAPCON-xt*) [6].

4.2.2 Cladding mechanical properties

The cladding stress has been selected as FOM. In particular, cladding yield stress is used in the approach. Nonetheless, it is well known that yield stress depends on how cladding is loaded. Accordingly, and based on data available, the calculation of stress differentiates between uniaxial and flexural loading.

Uniaxial loads:

The FRAPCON mechanical model includes cladding properties correlations (for irradiated material) supported by uniaxial test data for yield stress, plasticity, ultimate tensile strength and uniform elongation. These correlations, though, do not apply in the case of cladding with radial hydrides and/or hydride blisters. In other words, their application assumes no radial orientation of hydrides and no blisters in cladding.

The stress – strain behaviour in FRAPCON is modelled with the Hooke’s law (Eq.1) for the elastic regime and the Eq.2 for the plastic regime.

$$\sigma = \varepsilon \cdot E \quad (\text{Eq. 1})$$

$$\sigma = K \cdot \varepsilon^n \cdot \left(\frac{\dot{\varepsilon}}{10^{-3}}\right)^m \quad (\text{Eq. 2})$$

Therefore, the yield stress is the intersection of these two equations (Eq. 3).

$$\sigma_Y = \left[\frac{K}{E^n} \cdot \left(\frac{\dot{\varepsilon}}{10^{-3}}\right)^m \right]^{\frac{1}{1-n}} \quad (\text{Eq. 3})$$

where,

σ : stress

ε : strain

E: elastic modulus (f(T, [O₂], cw, φt))

K: strength coefficient (f(T, cw, φt))

n: strain hardening exponent (f(T, φt))

m: strain rate exponent (f(T))

Regarding the strain limit, the criterion defined in FRAPCON [8] (Eq. 4), is used.

$$\varepsilon = a - b \cdot T + c \cdot \exp\left(\frac{\varphi t}{d}\right) - \sqrt{\frac{[H]_{ex}}{e}} \quad (\text{Eq. 4})$$

being,

a, b, c, d and e: fitting parameters

T: cladding average temperature

φt : fast neutron fluence

[H]_{ex}: hydrogen concentration in excess of solubility limit

Note that the cladding mechanical properties modelled in FRAPCON-xt take into account both the irradiation hardening (i.e., yield stress increases with the irradiation) and thermal annealing (i.e., decrease of hardening at high temperature during long periods of time, like in dry storage) [10].

Flexural loads:

In case of flexural loads, a correlation between yield stress and burnup has been implemented in FRAPCON-xt (Eq. 5). This correlation has been derived from experimental stress-strain data obtained from bending tests conducted by NAGRA-JRC within the scope of the EURAD project (Task 3 of SFC work-package).

$$\sigma_Y = 2.54 \cdot Bu + 653.5 \quad (\text{Eq. 5})$$

In Figure 25 the model used by FRAPCON for the calculation of the yield stress is compared with the experimental data provided within the project for irradiated material. In order to carry out the comparison, the conditions under which the calculation has been performed have been the same as those under

which the data have been measured (i.e., at room temperature and for end of life in reactor). The figure shows the same trend with burnup, but quantitative differences, being the yield stresses calculated with FRAPCON more than a 20% higher than measurements.

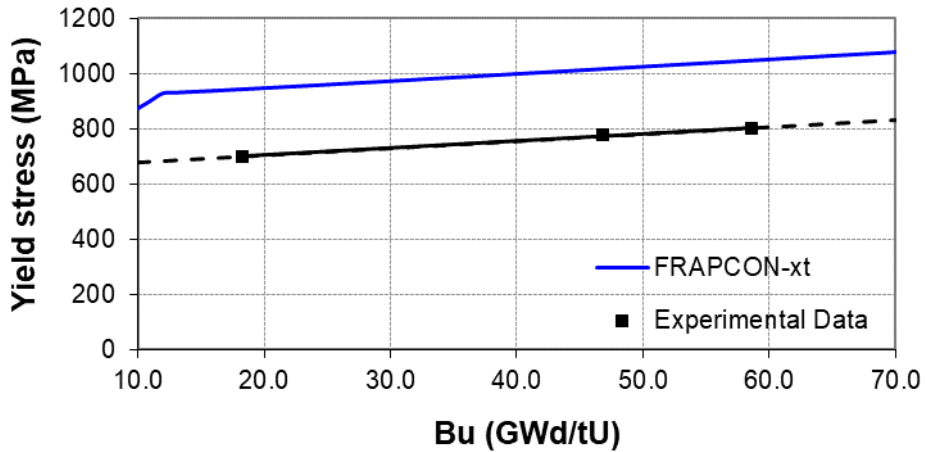


Figure 25 – Yield stresses vs. burnup (at EOL and room temperature).

For flexural loads, the strain limit defined from experimental data for irradiated material would be used. In Figure 26, FRAPCON's strain limit is compared with these experimental data.

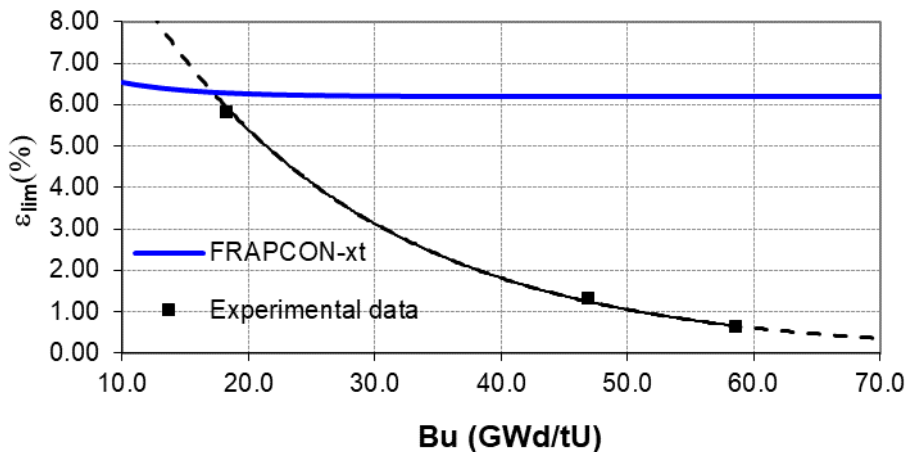


Figure 26 – Comparison of the strain limits between FRAPCON and data provided from the project.

As noted, the strain-to-failure estimated by FRAPCON barely changes and it is higher than those derived from experimental observations over practically the entire burnup domain: the higher the burnup, the larger the discrepancy. The strains-to-failure data were derived through applying the beam theory to measurements (i.e., fresh cladding tubes were treated as beams). The samples used for the testing were not submitted to high temperature for long periods of time, so that annealing did not play any role in recovering irradiation damage. This might be, at least, part of the reason of the difference between both sources of strain-to-failure values.

4.2.3 Failure criteria

Figure 27 outlines the logics scheme in place to decide whether a fuel rod cladding failed or not. As expected, the failure criteria set are embedded. A short description is given below:

- The first criterion is based on the ISG-11 [11], which limits the cladding hoop stress to 90 MPa to ensure the integrity of the fuel cladding due to hydrides radial reorientation embrittlement. Beyond this stress level, it is considered that hydrides reorientation could lead to brittle cladding.
- Going down the left branch, the next criterion refers to temperature of ductile-to-brittle transition at the time of the accident, and the second one to the deformation limit for brittle cladding with reoriented hydrides. Due to the scarcity of data, these two criteria have not been used in the subsequent application of the methodology.
- In the case of the right branch, the first criterion limits the concentration of radially reoriented hydrides after dry storage to characterise the ductility of the cladding, the second compares the stress endured by the cladding (assumed ductile) at the accident with the yield stress to determine if the plastic regime is attained. The last criterion of this branch compares the strain reached by the cladding with the strain limit. The first of these three criteria has not been used in the application due to the lack of data in terms of a radial hydrides concentration limit to compare with.

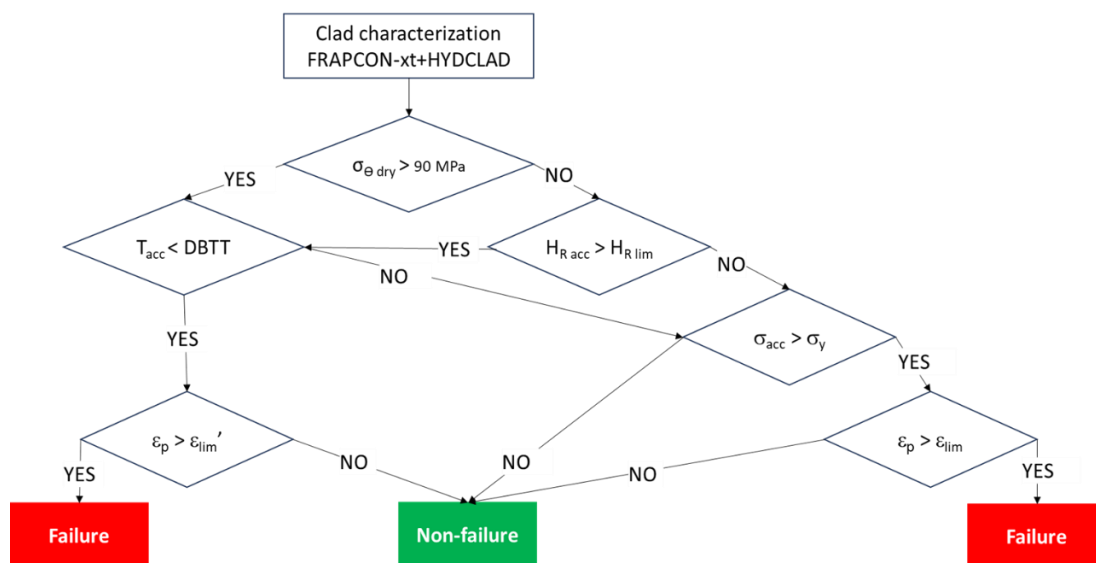


Figure 27 – Failure criteria.

It should be noted that the failure criteria used in the methodology so far are based on information made available in the open literature and on the information obtained within the EURAD project.

Particularly, it is considered the following:

- If the maximum cladding hoop stress in dry storage (related to the storage onset) is higher than 90 MPa, there is hydride radial reorientation. From a very conservative point of view the cladding is considered brittle, assuming that any load can break the cladding. Note that, as it is said

before, the scarcity of available information about a sound threshold for irradiated claddings as a function of the radial hydrides concentration (e.g., ductile-to-brittle transition temperature or strain limit) prevents from reducing this high conservatism in the current methodology. If this threshold were made available, the methodology would take advantage of the HYDCLAD predictions about radial hydrides.

- If the maximum cladding hoop stress in dry storage is lower than 90 MPa, due to the lack of a limit for the radial hydrides concentration, it is considered that there is not enough hydrides radial reorientation to cause the embrittlement of the cladding. Thus, the cladding is considered ductile (with the irradiation damage taken into account by the material properties modelling) and the failure limit imposed is the yield stress [12]. Based on that, if the cladding hoop stress is lower than the yield stress, it is considered that there is no cladding failure, whereas if it is higher, a second criterion is applied, comparing the attained deformation with the deformation limit to determine if there is cladding failure.

4.2.4 Statistical analysis

The statistical analysis has been adopted by coupling FRAPCON-xt with the statistical toolbox DAKOTA [13]. This coupling allows the propagation of thermo-mechanical input variabilities to obtain the failure probability from the output targeted (i.e., FOM selected). The variabilities considered are the fuel rod design, irradiation history, cladding temperature evolution in dry storage, and cladding temperature at the time of the accident. With these variabilities, DAKOTA fixes an input for each FRAPCON-xt run (scheme in Figure 28) and applies a Monte Carlo based on a simple random sampling.

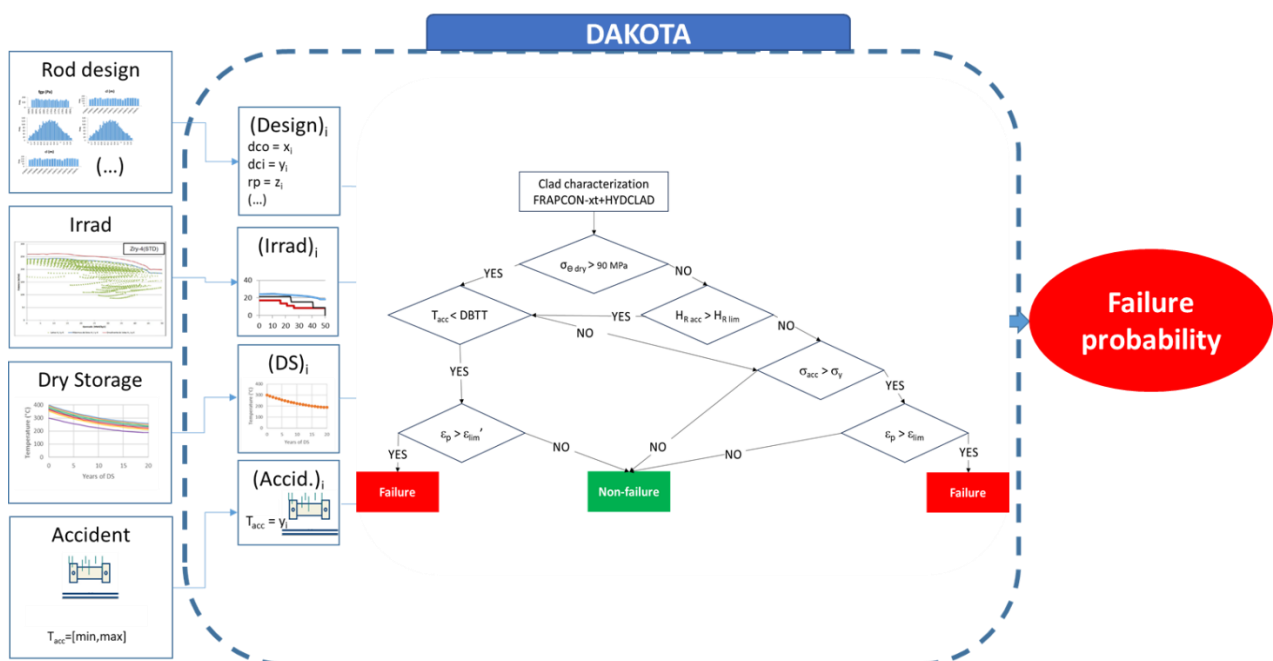


Figure 28 – Statistical approach scheme.

4.3 Application

4.3.1 Base Case

The methodology has been applied to an irradiated PWR fuel rod under a transfer cask side drop accident after 20 years of dry storage in a metallic cask. A total of 1000 cases has been created with DAKOTA and simulated with FRAPCON-xt. The input parameters for which variability in their value has been defined, can be classified as follows:

- Rod design. Helium fill gas pressure and fuel density have been selected for the application, due to their impact on the cladding stress [14]; their variability has been defined by a uniform probability density function between 1.86 and 2.51 MPa and a normal distribution (with a mean value of 95.5% and a standard deviation of 0.228% of the UO₂ theoretical density), respectively.
- Power history. 3 cycles have been simulated with constant linear power in each one (Figure 29). The power in each cycle is the parameter to vary, with uniform distributions between maximum and minimum levels that come from a database of commercial power histories [15].
- Dry storage conditions. The parameter selected as a key aspect in the study is the cladding temperature. Uniform distributions have been applied between temperatures profiles along time obtained in previous studies with Ansys Fluent [16], [17]. The initial maximum temperature ranged from 300 to 400 °C.
- Accident conditions. The parameter varied is the cladding temperature for its impact on the cladding properties (i.e., yield stress). It has been applied a uniform distribution between 100 and 200 °C, which is a range typically considered in related tests [18].

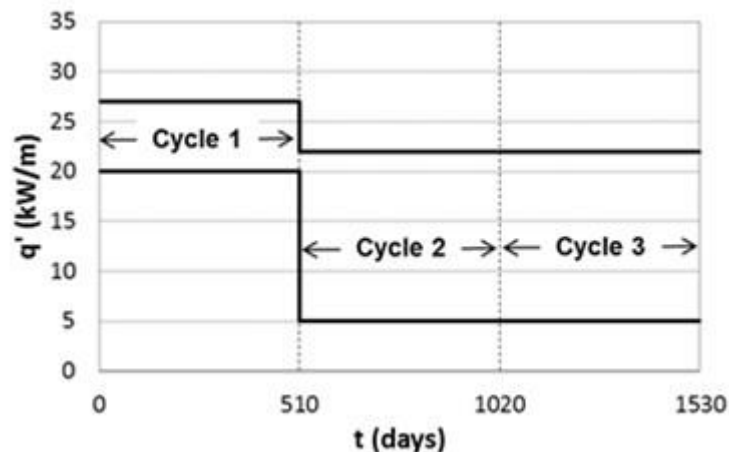


Figure 29 – Variability in lineal power history [15].

Concerning the maximum cladding stress in the accident, a maximum stress value of 405 MPa, found in the literature for a side drop analysis of a Dry Storage Canister [19], has been applied.

Due to the impact of the temperature on the cladding properties, since the accident analysis has been conducted at temperatures between 100 and 200 degrees and the information for flexural loads is at

room temperature, the analysis has been carried out using the properties included in FRAPCON, which, as already explained, are derived from uniaxial tests.

Figure 30 shows the results obtained in terms of cladding hoop stresses at the dry storage onset (left figure, which compares the results with the hydride radial reorientation threshold of 90 MPa), and the cladding yield stress as the failure limit considered in the accident for ductile material (right figure, which compares the estimations with the maximum stress applied of 405 MPa). The results show large safety margins:

- Maximum cladding hoop stress at dry storage onset of 79 MPa gives rise to around 14% of margin with respect to the threshold set. Thus, according to the methodology, the cladding is ductile;
- Minimum yield stress at the accident of 457 MPa gives rise to around 13% of safety margin, taking into account the accident maximum stress applied, that is to say, the failure probability is zero.

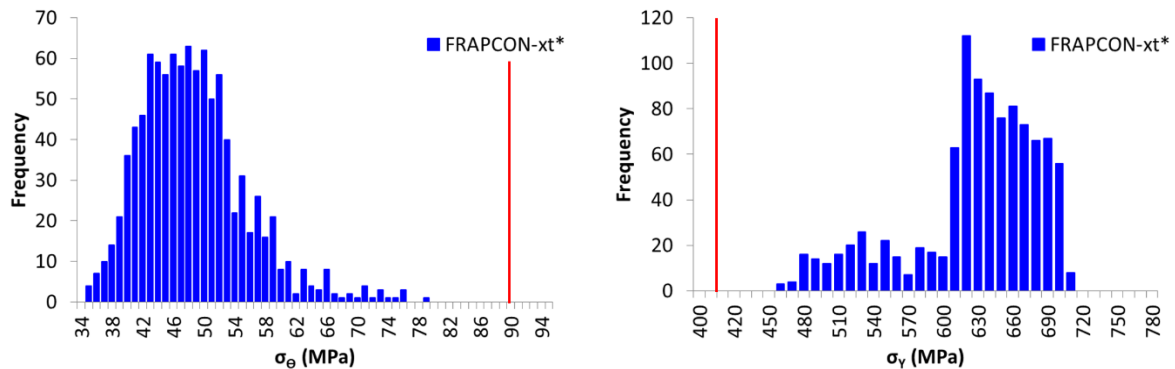


Figure 30 – Cladding hoop stress at dry storage onset (left) and yield stress at the moment of the accident (right); red lines represent the ductile-to-brittle threshold set (left) and the accident maximum stress applied (right).

4.3.2 Scoping calculations

In this section, three factors that could have an impact on the assessment carried out are analysed. The first one refers to the irradiation stage, the second one to the storage stage, and the third one to the criterion used in the accident stage.

Irradiation stage:

The impact of the FGR modelling on the hydride radial reorientation embrittlement at high burnup has been studied. The FRAPCON-xt (with MASSIH FGR model) was compared with FRAPCON-xt* (with FRAPFGR model calibrated above 60 GWd/tU) in terms of the maximum cladding hoop stress predicted at the beginning of dry storage (Figure 31);

From Figure 31 it can be inferred that there is no important impact of the FGR model used. Particularly, the maximum stress obtained with the MASSIH model is around 5% lower than the one estimated with the calibrated FRAPFGR model. Note that despite maximum burnups of 68 GWd/tU have been reached, most burnups obtained with the Monte Carlo are below 60 GWd/tU.

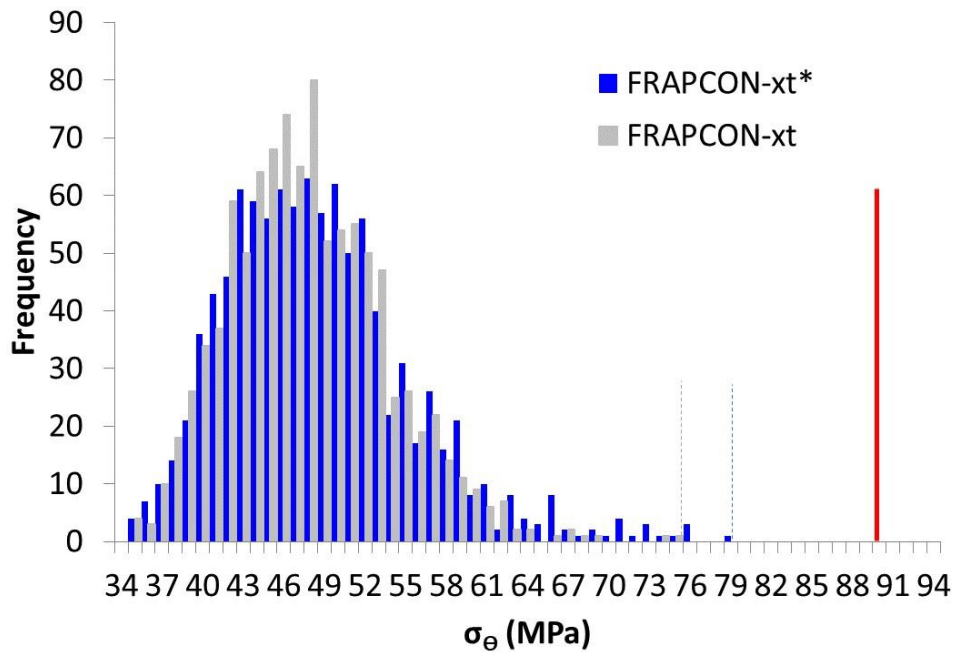


Figure 31 – Cladding hoop stresses at the dry storage onset. Predictions with FRAPCON-xt (MASSIH) and FRAPCON-xt* (calibrated FRAPFGR).

Storage stage:

In this case, the effect of the irradiation damage annealing on the yield stress in the accident is assessed. The FRAPCON-xt* prediction has been compared against two additional cases, one of them disabling the annealing model (No annealing) and the other setting the irradiation damage to zero (Full annealing) (Figure 32).

In Figure 32, it can be observed notable differences of the parametric cases (no annealing and full annealing) with respect to the base case (FRAPCON-xt* with the annealing model by default). In spite of that, only the complete recovery of the irradiation damage gives rise to non-zero failure probability with the accident stress applied in this study; even in this case, the failure probability is low (0.3%). The differences obtained with these parametric cases point out that the irradiation damage annealing is an important aspect to be analysed for the assessment of the integrity of SNF under accident scenarios.

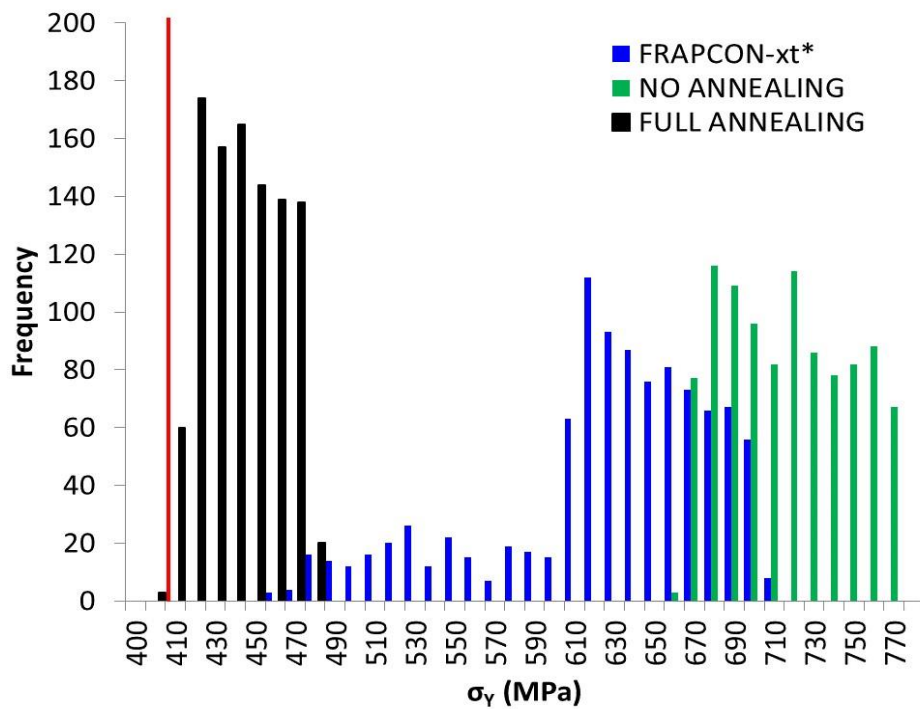


Figure 32 – Yield stress at the accident. Predictions with FRAPCON-xt*, and with no annealing and full annealing.

In order to check the FRAPCON’s modelling of the cladding irradiation damage annealing, experimental data from a recent work at a temperature of 360°C [20] have been compared with results given by simulating the same conditions with FRAPCON-xt* (Figure 33). The comparison was made in terms of a fast neutron fluence (related to the irradiation damage) and the yield stress of the material. The code predictions show almost negligible effect of the annealing (it should be noted that the experimental trend is captured around 400 °C), while the experimental data show an important impact on the yield stress at a temperature of 360 °C (decrease from 700 to 400 MPa, approximately). Therefore, further assessment/enhancement is needed for the FRAPCON-xt* annealing model under dry storage conditions, in order to enhance the accuracy of the methodology presented.

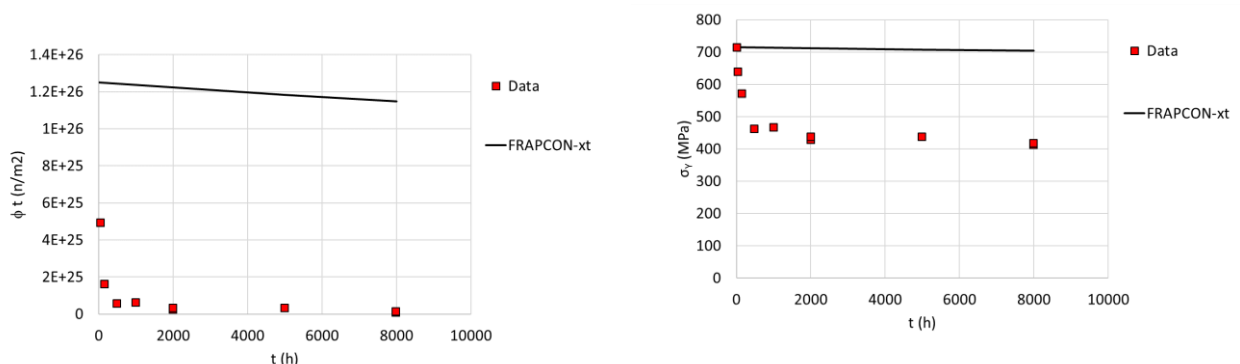


Figure 33 – Model-to-data comparison for fast neutron fluence (left) and yield stress (right) evolution with irradiation damage annealing at 360 °C. Data from [20].

Accident stage:

To ensure conservatism in the results obtained with FRAPCON-xt*, the calculations of yield stresses have been repeated for an accident at room temperature, allowing a comparison between the results obtained for axial and flexural loads. As it can be seen in Figure 34, the yield stresses obtained with FRAPCON-xt* are lower than those resulting from applying an interpolation of the experimental results to the burnups of the rods studied (It should be noted that, as it is said before, while FRAPCON-xt* are at the accident time, the experimental data are at end of life in reactor). Assuming that the behaviour observed at room temperature still stands at higher temperatures, the comparison of properties from flexural and axial tests indicates that the plastic regime would not be reached. Thus, the study remains conservative.

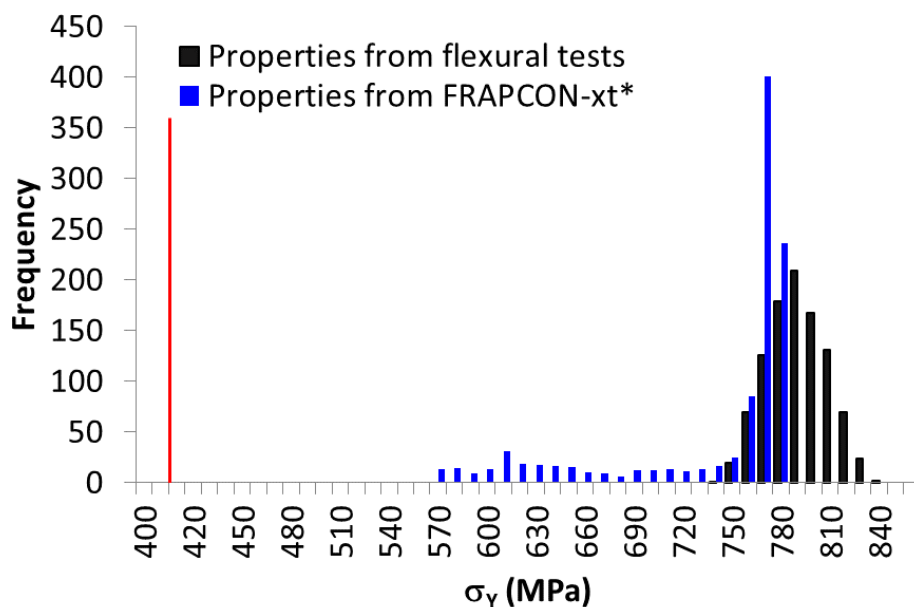


Figure 34 – Yield stresses obtained with FRAPCON-xt* at room temperature and with the interpolation of the experimental results with the burnup.

4.4 Final remarks

CIEMAT has developed a methodology to evaluate spent nuclear fuel rod cladding behaviour under handling/transport accidents, based on a statistical approach to characterise the cladding supported by an extended version of the FRAPCON-xt code.

The proof of concept derived has been verified through an application carried out in a postulated accident scenario (side drop with maximum load below 450 MPa after interim storage of fuel irradiated up to 70 GWd/tU). This proof of concept allows analysing the impact of aspects of interest for the cladding characterisation. The main conclusions from this analysis are the following:

- The analysis conducted has shown wide safety margins of hoop stress at drying for radial hydrides embrittlement (up to 70 GWd/tU)
- A potential impact of irradiation damage annealing indicates the need to further study this effect during dry storage.

4.5 References

- [1] IAEA, “Storage of spent nuclear fuel. SSG-15” 2020. [Online]. Available: <http://www-pub.iaea.org/MTCD/Meetings/PDFplus/2014/cn219/Presentations/12EKudryavtsev.pdf>.
- [2] SJÖLAND, A., CHRISTENSEN, P., ZETTERSTRÖM EVINS, L., BOSBACH, D., DURO, L., FARNAN, I., METZ, V., ZENCKER, U., RUIZ-HERVIAS, J., RODRÍGUEZ VILLAGRA, N., KIRÁLI, M., SCHILLEBEECKX, P., ROCHMAN, D., SEIDL, M., DAGAN, R., VERWERFT, M., HERRANZ, L.E., HORDYNSKYI, D., FERIA, F., VLASSOPOULOS, E., “Spent nuclear fuel management, characterisation, and dissolution behaviour: progress and achievement from SFC and DisCo” EPJ Nucl. Sci. Technol., vol. 9, p. 13, 2023, doi: 10.1051/epjn/2022029.
- [3] FERIA, F., AGUADO, C., HERRANZ, L.E., “Extension of FRAPCON-xt to hydride radial reorientation in dry storage” Ann. Nucl. Energy, vol. 145, p. 107559, 2020, doi: 10.1016/j.anucene.2020.107559.
- [4] F. FERIA AND L. E. HERRANZ, “Assessment of hydride precipitation modelling across fuel cladding: Hydridding in non-defective and defective fuel rods” Ann. Nucl. Energy, vol. 188, no. March, p. 109810, 2023, doi: 10.1016/j.anucene.2023.109810.
- [5] ADAMS, B.M., EBEIDA, M., ELDRED, M., et al., “Dakota, A Multilevel Parallel Object-Oriented Framework for Design Optimization , Parameter Estimation , Uncertainty Quantification , and Sensitivity Analysis : Version 6 . 2 Theory Manual” no. July 2014, 2015.
- [6] EURAD Deliverable 8.8, “Thermo-mechanical-chemical properties of unirradiated and irradiated samples of spent nuclear fuel rod segments and cladding”, 2024.
- [7] HERRANZ, L.E., FERIA, F., “Extension of the FRAPCON-3.3 creep model to dry storage conditions” Prog. Nucl. Energy, vol. 52, no. 7, pp. 634–639, 2010, doi: 10.1016/j.pnucene.2010.04.003.
- [8] GEELHOOD, K.J., LUSCHER, W.G., RAYNAUD, P.A., PORTER, I.E., “Frapcon-4.0: A Computer Code for the Calculation of Steady-State, Thermal-Mechanical Behavior of Oxide Fuel Rods for High Burnup,” PNNL-19418 Vol.1 Rev.2, 2015.
- [9] GEELHOOD, K.J., BEYER, C.E., LUSCHER, W.G., “Stress/Strain Correlation for Zircaloy” no. July, 2008, [Online]. Available: <http://www.ntis.gov/ordering.htm>
- [10] HAGRMAN, D.L., REYMANN, G.A., “MATPRO-Version 11: a handbook of materials properties for use in the analysis of light water reactor fuel rod behavior” Nureg/Cr-0497; Tree-1280 Trn 79-010376, 1979, [Online]. Available: <http://www.osti.gov/servlets/purl/6442256/>
- [11] US NRC, “ISG-11 Rev.3 - Cladding considerations for the transportation and storage of spent fuel” Spent Fuel Project Office Interim Staff Guidance - 11 , Revision 3, vol. 122, no. 1. 2003.
- [12] US NRC, “NUREG 2215 - Standard Review Plan for Spent Fuel Dry Storage Systems and Facilities” 2017.
- [13] ADAMS, B.M., EBEIDA, M., ELDRED, M., et al., “Dakota, A Multilevel Parallel Object-Oriented Framework for Design Optimization, Parameter Estimation, Uncertainty Quantification, and Sensitivity Analysis: Version 6.0 User’s Manual” no. July 2014, p. 331, 2014.
- [14] AGUADO, C., FERIA, F., HERRANZ, L.E., “Major sensitivities in FRAPCON-xt modeling of high burn-up fuel rods during dry storage to design and irradiation variables” Kerntechnik, vol. 85, no. 6, pp. 413–418, 2020, doi: 10.3139/124.200069.
- [15] FERIA, F., AGUADO, C., HERRANZ, L.E., “Methodology for a realistically conservative characterization of spent fuel in dry storage” Ann. Nucl. Energy, vol. 140, p. 107148, 2020, doi: 10.1016/j.anucene.2019.107148.

- [16] FERIA, F., AGUADO, C., HERRANZ, L.E., “Extension of FRAPCON-xt to hydride radial reorientation” Ann. Nucl. Energy vol. 145, pp. 25–27, 2019, <https://doi.org/10.1016/j.anucene.2020.107559>
- [17] HERRANZ, L.E., PENALVA, J., FERIA, F., “CFD analysis of a cask for spent fuel dry storage: Model fundamentals and sensitivity studies” Ann. Nucl. Energy, vol. 76, pp. 54–62, 2015, doi: 10.1016/j.anucene.2014.09.032.
- [18] GÓMEZ SÁNCHEZ, F.J., MARTIN RENGEL, M.A., RUIZ-HERVIAS, J., “A new procedure to calculate the constitutive equation of nuclear fuel cladding from ring compression tests” Prog. Nucl. Energy, vol. 97, pp. 245–251, 2017, doi: 10.1016/j.pnucene.2017.02.001.
- [19] ALBERDI, X., GOICOECHEA, C., GORROCHATEGUI, I., “A review of loading types and magnitudes in spent fuel assemblies during dry cask drop accidents. EJP-EURAD_IIT_003 v.0” 2021.
- [20] AOMI, M., YAMADA, D., SAKAMOTO, K., MIURA, Y., YOKOYAMA, H., SHIMIZU, M., ISHIOKA, S., SHIMA, A., TEZUKA, H., “Effects of thermal annealing on mechanical property and microstructure of BWR spent fuel cladding during dry storage”, 20th International Symposium on the packaging and transportation of radioactive materials (PATRAM22), (Juan-les-Pins, France, 11-15 June 2023), 2023.

5. Oxidation under air at 200 °C of irradiated fuel sections at high burn-up: destructive examinations (metallography, SEM, TEM) of UOX section with Zy-4 cladding ruptured after 13,630 hours of heating

5.1 Introduction

Within the framework of a research project in the tripartite institute gathering EDF, CEA and Framatome, the behaviour of irradiated fuel rods under dry storage conditions is studied. In particular, the accidental scenario corresponding to an exposure to air of a defective nuclear fuel rod is considered.

To this aim, a first oxidation campaign (200 °C under air) was performed at CEA from 2002 to 2007 on UOx and MOX irradiated fuel fragments and on irradiated fuel sections with Zy-4 cladding with a cumulative duration of approximately 14000 hours [1], [2]. This campaign highlighted a rupture of the cladding for several sections [2], [3]. The formation of U_3O_8 was considered to explain the swelling of the fuel because of the lower density of U_3O_8 (8.34 g.cm⁻³) compared to UO_2 (10.99 g.cm⁻³) but no proof of its existence was observed experimentally. A second oxidation campaign was performed under the same conditions (200 °C under air for 13500h) between 2008 and 2011 on fragments of UOx and MOx to study the possible formation of U_3O_8 for longer oxidation times [4] and on six sections with Zy-4 cladding and six sections with M5 cladding.

At the end of the oxidation experiments, visual inspection of the sections revealed a cladding rupture following the rod vertical axis, occurring for 5 out of 6 rods with Zy-4 cladding, after 8000 h of heating [5]. Based on the low weight gain and the visual inspection, no U_3O_8 was assumed to be formed during the oxidation. Metallographic and SEM observations on UOx sections with Zy-4 cladding (BU = 64.4 GWd/tU) showed that the layers of internal and external zirconia were not modified and that additional fracturing occurred at the periphery of the pellet. No modification of the microstructure was noticed, with no U_3O_8 formed. The cladding rupture was supposed to originate from a weakening and an opening of the grain boundaries correlated to an interconnection of gas bubbles in intergranular position from 0.55 to 0.95R. This would result in a gas release, creating stress on the internal part of the cladding, initiating its rupture. The latter was found to be located where the cladding is the most fragile, i.e. close to a spall of external zirconia and where the hydride are accumulated in the form of a blister.

In order to understand the rupture phenomenon, further studies were performed on the opening of the grain boundaries. To this aim, another section of the same rod, also exposed to air at 200 °C for 13630 h, was studied. A lengthwise and straight rupture of the cladding was observed in this case, occurring between 8100 and 13600 hours of oxidation. In this work, destructive analyses such as metallographic observations, Focused Ion Beam-SEM (FIB-SEM) and Transmission Electron Microscopy (TEM), were performed on this rod section, and are presented with a focus on the study of the grain boundaries along the pellet radius. All the experiments were performed at the LECA-STAR facility, in the hot laboratories, at CEA Cadarache (France).

5.2 Principles of the experiment and sample description

5.2.1 Principles of the experiment

The principle of the oxidation tests, with the experimental setup illustrated in Figure 35 – , is the following: the fragments and sections were placed in small airtight stainless steel containers with a brass screw-on lid. The containers were then put into the pits of an oven, where the temperature was regulated at 200 ± 1 °C, using a thermocouple. No control of the atmosphere was performed, with only the airflow of the cell as incoming gas. During the experiments, the samples were extracted periodically from the pits to be weighted with a 1-mg precision scale to study the mass variation compared to their initial mass (before oxidation).

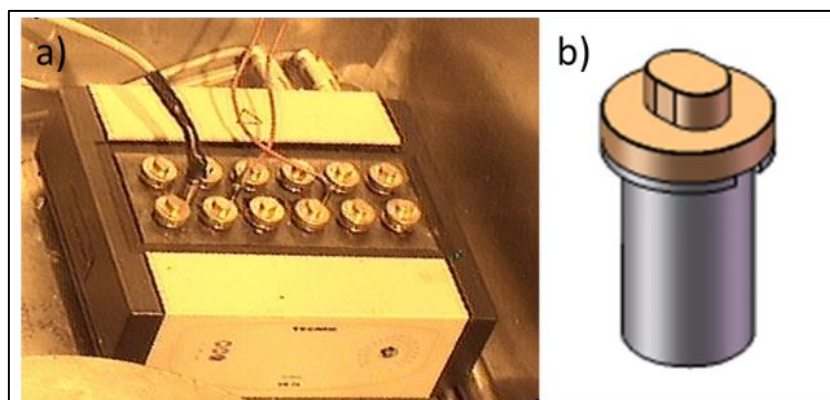


Figure 35 – (a) Oven used for long term oxidation cells, consisting of 12 cylindrical cells in a copper block and (b) example of a container, both used in the hot cell.

5.2.2 Kinetic results and visual observations

Figure 36 – presents the weight gain curves of the various sections of UO_2 during the oxidation tests. The kinetics of oxidation are similar for all sections [5]. Two domains can be identified on the UOX curves: a first fast oxidation phase, between 0 and 6000 h, and a second slow phase, almost linear, until the end of the oxidation tests at approximately 13650 h. The final oxidation rate is inferior to 3% and no acceleration of the kinetics is visible, indicating the absence of formation of U_3O_8 . The final oxidation rate seems to be dependent on the length of the section in the case of Zy-4 cladding, with smaller oxidation rates for long sections. In the case of the section of interest (Section 4), the final oxidation rate is 2.46 %.

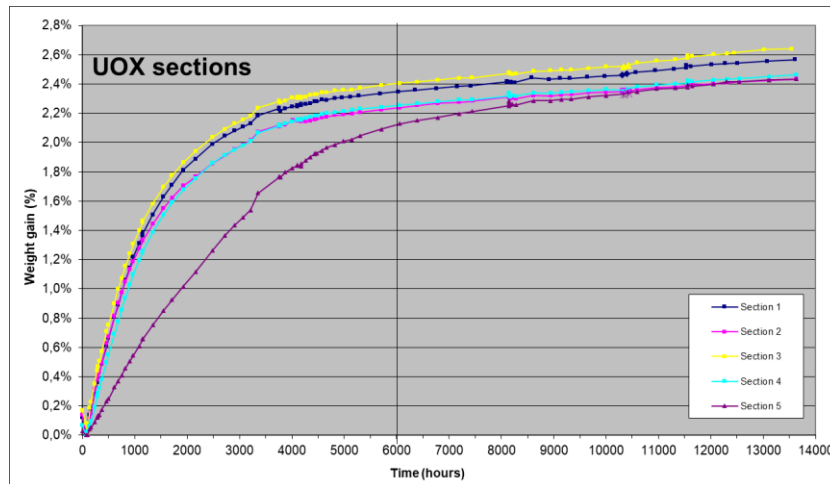


Figure 36 – Weight gain of UOx sections as a function of time.

Pictures of the section of interest taken during the oxidation test are shown in Figure 37. A longitudinal straight-lined rupture of the cladding, indicated by the red arrow, can be seen, occurring between 8140 and 13600 h.

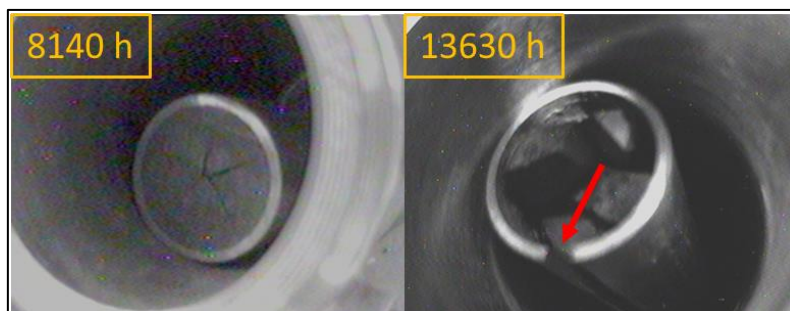


Figure 37 – Section of interest section after 8140 and 13630 h of oxidation test under air at 200 °C [5].

5.2.3 Characteristics of the section of interest

In this work, experiments were performed on a section of 30 mm of UO₂ with Zy4 cladding (irradiated during 6 cycles), heated at 200 °C under air during 13630 h.

5.2.3.1 Preparation of the section

The section was extracted from the fourth floor of the rod, with the following dimensions: low at 2122.2 mm/rod bottom and high at 2152.2 mm/rod bottom. The state of the section at the end of the oxidation test is shown in Figure 38.

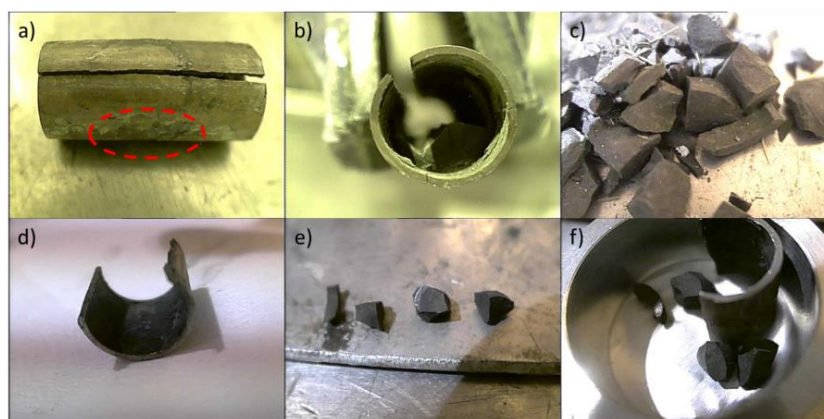


Figure 38 – Sample's section after 13630 h of oxidation test at 200 °C under air, with (d) and (e) the cladding section and fragments selected for observations.

The cladding presents several cracks, all straight-lined and within the cladding axis, with an irregular surface. The red circle on Figure 38(a) corresponds to a spall. While taking the section out of its container, the integrity of the fuel pellet was damaged and numerous fragments fell out of it, while some remained attached to the cladding. During the cutting operation performed to reduce the length of the section, the cladding broke into 2 pieces. From the fallen fragments, four were selected for optical observations (Figure 38(e)), as well as a segment of the cladding (Figure 38(f)).

5.3 Optical observations

5.3.1 Cladding

A segment of cladding, which does not represent the whole circumference of the pellet, was selected and prepared for optical observations (Figure 39). The areas highlighted by the coloured rectangles correspond to the ones studied by optical microscopy and SEM.

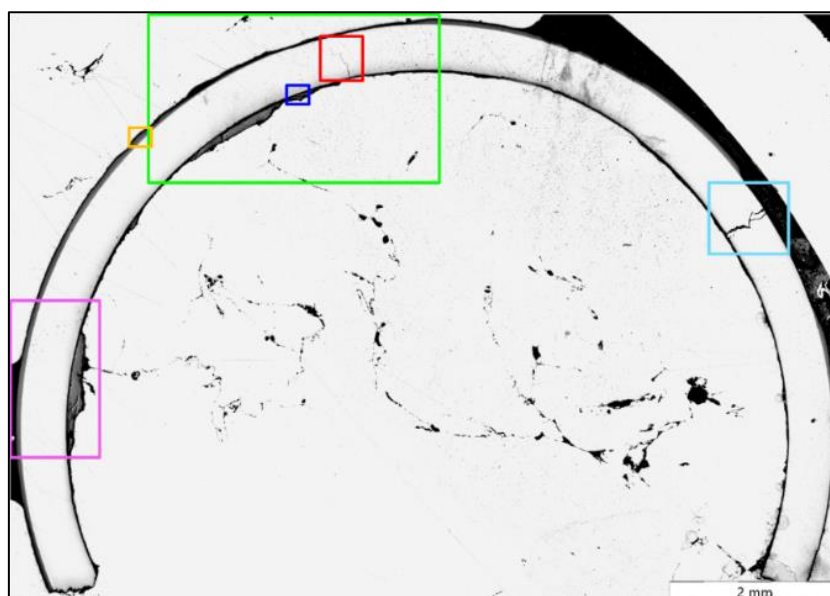


Figure 39 – Optical observation of the cladding segment and positions of the detailed areas.

The rupture of the cladding can be seen on the bottom left part of Figure 39. The presence of radial cracks within the cladding is also revealed here. Small pieces of fuel attached to the cladding as well as a small layer of external zirconia can also be observed. Zooms on these details are presented in Figure 40 (red for the crack, orange for the external zirconia and blue for the pellet/cladding interface).

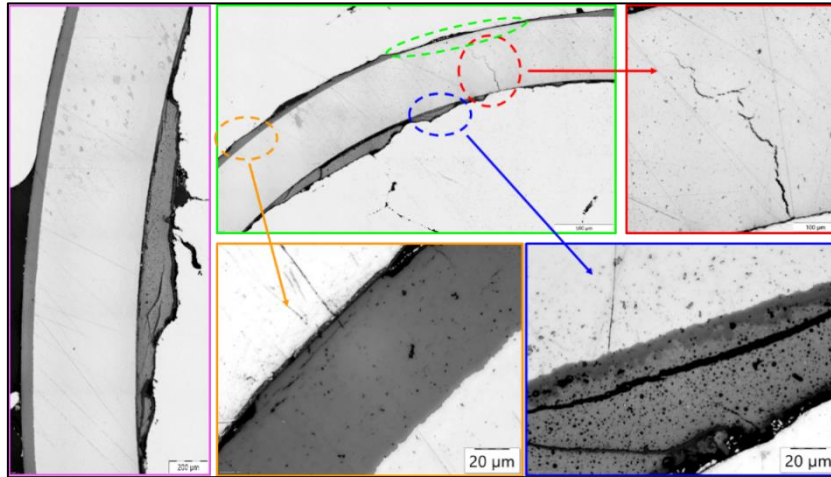


Figure 40 – Optical observations of the cladding (green and pink) and selected areas of crack (red), external zirconia (orange) and pellet/cladding interface (blue).

The zoom on the crack section (in red) reveals a network of cracks, mainly radial, originating from the pellet/cladding interface and moving through the cladding, however not reaching the external zirconia. The latter, observed in the orange zoom, has a thickness of approximately 70 µm. When looking at the selected area of Figure 40 and at the whole micrograph on Figure 39, it can be noticed that this thickness is not homogenous throughout the whole cladding.

The pellet/cladding interface is presented on the blue zoom. A dark grey area is observed, moving towards the fuel, corresponding to an oxide formation due to oxygen transport from the UO₂ fuel to the zirconium of the cladding, which induces cladding oxidation. This internal zirconia is interconnected with the fuel by “chemical bonding” and enhanced the grip between the fuel and the cladding. This explains why some pieces of the fuel remained attached to the cladding while the rest of it broke down into pieces during the handling of the section. This zirconia layer is present throughout the whole periphery of the pellet (see blue area on Figure 40), with some pores visible, and is approximately 5 to 15 µm thick. A wave-shape is observed for this layer, with peaks and withdrawals within the fuel. This aspect is typical of M5 and Zy-4 claddings irradiated in similar conditions. Circumferential cracks are also visible on this zoom, as well as the typical microstructure of the High Burnup Structure (HBS) in particular with a high density of small bubbles.

5.3.2 Fuel

As the fragments were detached from the rest of the pellet when they were prepared, it was necessary to identify first their positions within the pellet. The location of three samples among the selected ones was identified, which are represented in Figure 41 with the associated positions.

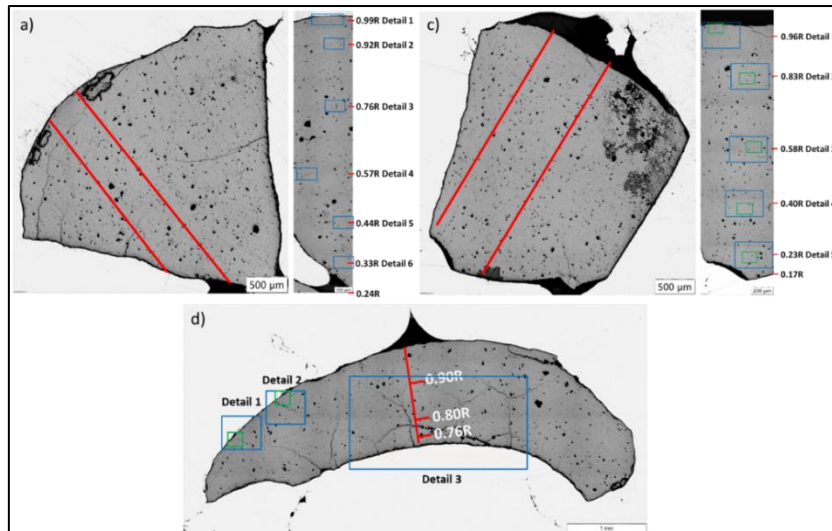


Figure 41 – Positions of the selected fragments and areas observed by optical microscopy.

These images revealed the presence of circumferential cracks, mainly located between 0.70R and the pellet/cladding interface. Radial cracks are also visible at the periphery of the pellet (Figure 41(d)), where a network of numerous cracks is present. The same type of cracks were already observed in [5] and the cracks at the extreme periphery were found to originate from the oxidation test and the release of constraints present in the pellet. Pores of various sizes can also be observed, located along the whole pellet radius. It can be seen that the surface of the fragments at the extreme periphery is not flat, as some pieces remained attached to the cladding.

Optical observations of the details shown in Figure 41 were performed and as the microstructure was similar for the fragments (a) and (c), only the results obtained on the fragment (a) are presented in Figure 42.

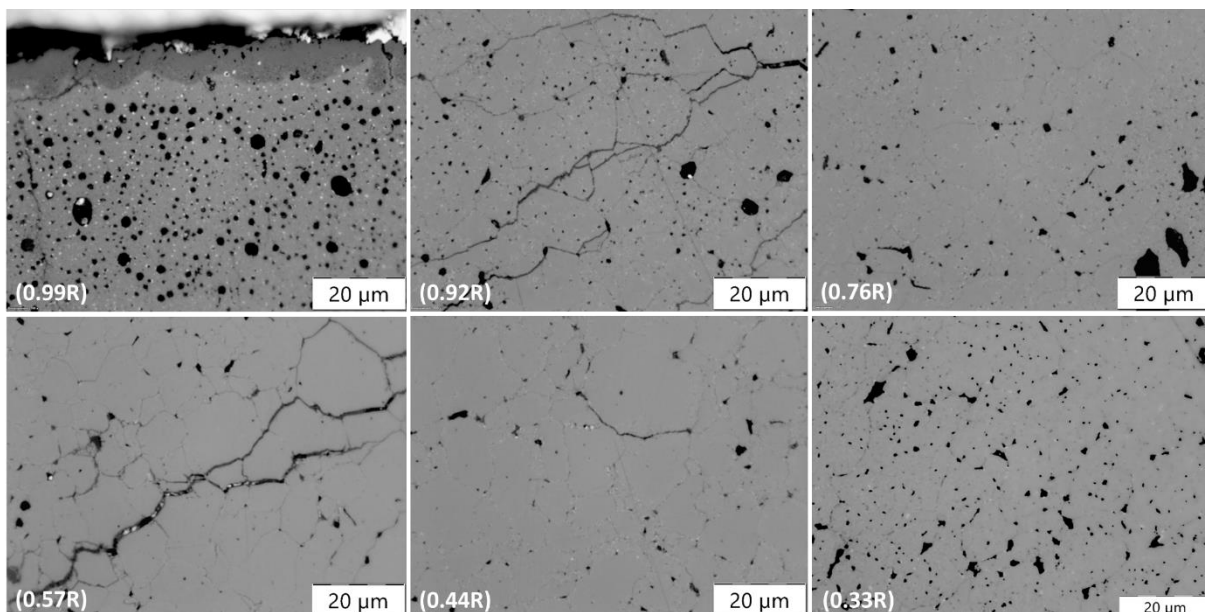


Figure 42 – Detailed areas of Fragment (a) from 0.99R to 0.33R.

The presence of U_3O_8 is not evidenced with these optical observations.

The weakening of the grain boundaries is highlighted here in Figure 42. The interconnection of the intergranular gas bubbles, as well as the opening of the grain boundaries was supposed to enhance the release of gaseous fission products located in the intergranular bubbles. This would have resulted in a mechanical constraint applied to the cladding, leading to its rupture. This assumption is comforted by the location of pores at grain boundaries.

5.4 SEM observations

Various types of SEM observations were performed on a fuel fragment (c) as well as on the cladding segment.

5.4.1 2D

5.4.1.1 Cladding

SEM observations of various areas of the cladding where cracks can be seen were performed, with different examples illustrated in Figure 43.

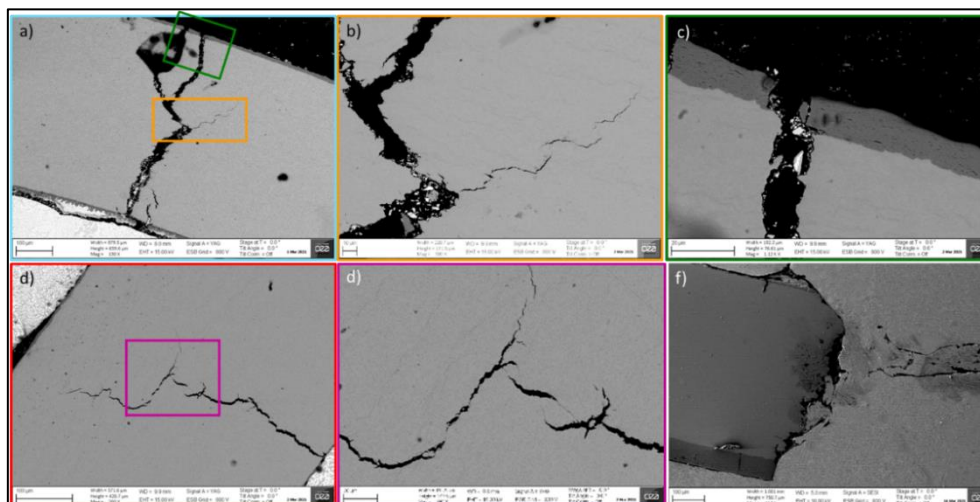


Figure 43 – SEM observations of different sections of the cladding segment.

These observations indicate that radial and circumferential cracks also occurred in the cladding after occurring in the fuel. This highlights the pressure applied to the cladding by the swelling phenomena happening in the fuel during the oxidation test. The area of the cladding rupture is visible in Figure 43(f) and it can be noticed that it is not a sharp rupture with an irregular surface and a quasi-linear orientation.

On Figure 43(a), (c) and (d), a thin layer of external zirconia of approximately $10\ \mu\text{m}$ is visible, while the thickness of the non-oxidised cladding is approximately $525\text{-}550\ \mu\text{m}$. It can be seen that the external zirconia layer is not homogeneous throughout the whole cladding, with some variations of its thickness and its boundary in some areas. This inhomogeneity can be related to the presence of spalls on the outer of the cladding.

5.4.1.2 Fuel/cladding interface

As observed in Figure 40, pieces of fuel remained attached to the internal zirconia of the cladding. SEM observations on the fuel/cladding interface were performed and are presented in Figure 44.

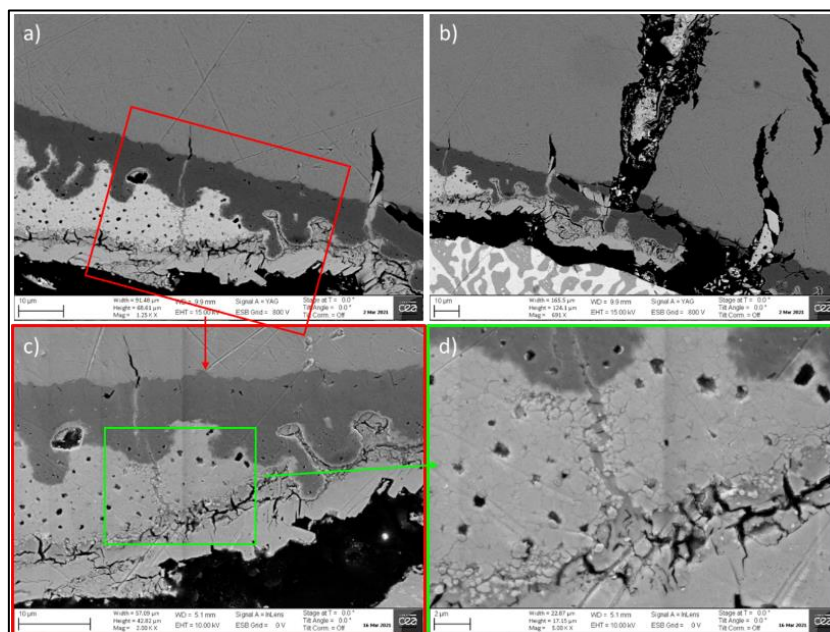


Figure 44 – SEM observations of different areas of fuel/cladding interface.

As previously said, a layer of internal zirconia is observed on the different areas analysed. It is not homogenous throughout the whole cladding and presents a wave shape, with some movements in and out of the fuel. Its thickness varies between 5 to 15 μm . On Figure 44(c) and (d), a network of circumferential and radial cracks at the extreme periphery of the pellet is visible. A restructured area is also observed on Figure 44(d) with the presence of numerous bubbles and a subdivision of the grains located close to a crack.

5.4.1.3 Fuel

2D imaging was done first to study the microstructure along the pellet radius on the areas previously studied (green rectangles on Figure 41(c)). The images obtained for 0.96R, 0.83R, 0.58R, 0.40R and 0.23R are presented in Figure 45.

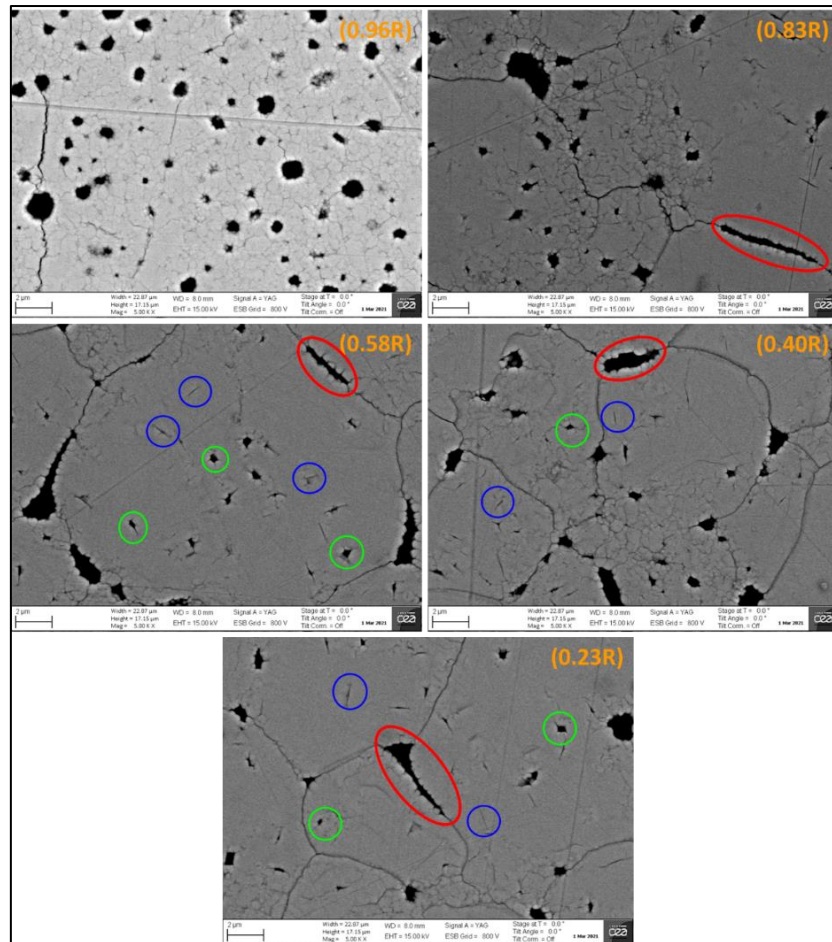


Figure 45 – SEM observations of Fragment (c) at 0.96R, 0.83R, 0.58R, 0.40R and 0.23R.

At 0.96R, the typical microstructure of the HBS is observed, with a restructured zone, i.e. a subdivision of grains leading to smaller grains of less than 1 μm . The grain boundaries are visible, with cracks along them in some areas. A high concentration of intergranular round-shaped bubbles of various sizes (from 1 to 0.2 μm) can also be noticed.

At 0.83R, a subdivision of the grains is also visible, with sub-micrometric grains corresponding to the beginning of the HBS formation. However, in this case, bigger grains of few microns remain. The subdivision noticed here leads to smaller grains inside big grains, appearing mainly at or near the initial grain boundaries. On this image, it can be noticed that the grain boundaries seem to be open, with some bubbles in them. As for 0.96R, intergranular bubbles are seen, however in smaller proportion and of different shapes, mainly lenticular.

A similar microstructure is observed at 0.58R, 0.40R and 0.23R, with a subdivision of the grains near the grain boundaries, surrounded by bigger grains of few microns. At these positions, an opening of some grain boundaries is noticed, with the presence of intergranular oblong bubbles (see red circle on Figure 45). Intragranular bubbles of peculiar shape can also be observed. Indeed, the bubbles appear to have a central round part, from which dendrites are growing (see green circles on Figure 45). Another particular feature observed at these three positions is the presence of small cracks at the surface, highlighted with the blue circles on Figure 45. These cracks seem to be connected to the bubbles and thus to indicate the presence of cavities below the surface.

These images obtained along the pellet radius revealed a subdivision of the grains occurring at the grain boundaries independently of the position, as well as an opening in some areas of the grain boundaries and the presence of bubbles of peculiar shapes.

5.4.2 3D

In order to look into these features, 3D observations were performed with a FIB-SEM at 0.2R and 0.8R of the same fragment. Several areas were studied for each pellet radius but only one will be presented at each pellet radius as they all revealed the same observations for one position.

5.4.2.1 0.2R

The area studied at 0.2R is a cube with images taken every 15 nm, resulting in overall 803 images, covering a cube of $15 \times 8 \times 8.9 \mu\text{m}^3$. Among them, 607 images were sorted out and used for this work. A refinement procedure was applied to the selected images to correct potential differences in position, defects of curtaining and lighting during the acquisition.

The Figure 46 presents several images, taken every 750 nm (one image out of 50) and highlights the variation of the microstructure in depth in the material.

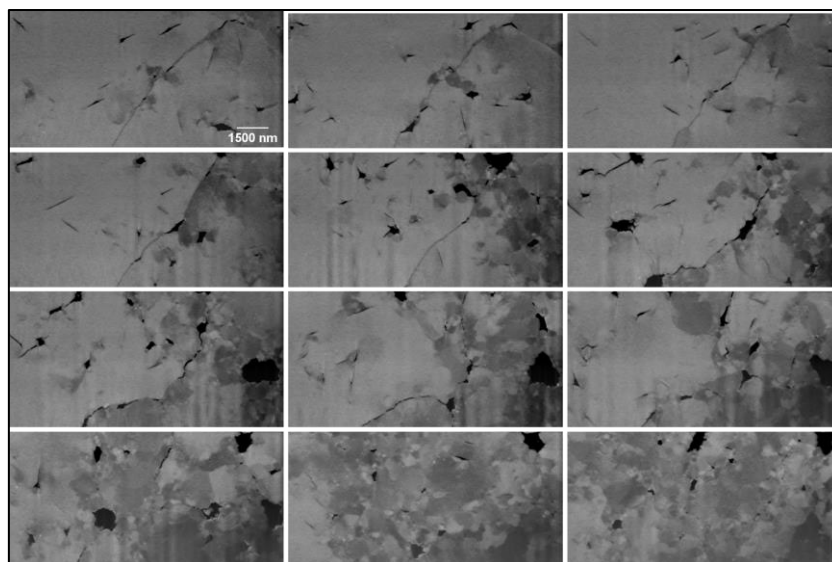


Figure 46 – Images at 0.2R extracted from a 3D acquisition (step of 750 nm between each image, one image out of 50).

An image extracted from the 3D acquisition is visible in details in Figure 47 –. White spots are observed, indicating the presence of small metallic precipitates. It can be noticed that these precipitates are mainly located close to the bubbles.

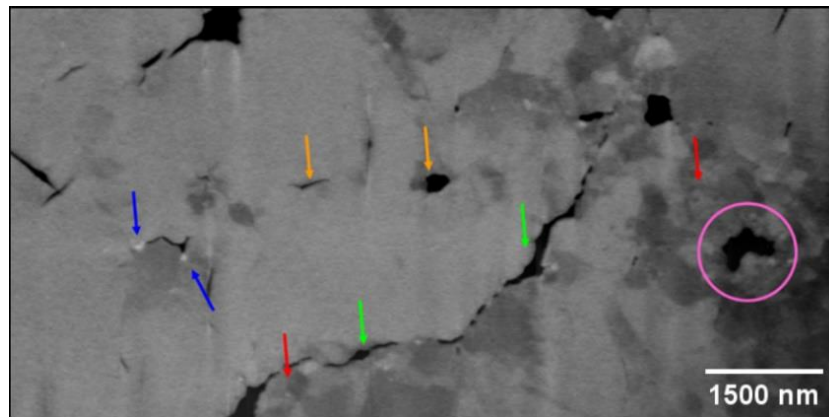


Figure 47 – SEM observation at 0.2R taken during a 3D acquisition, revealing the presence of precipitates, intragranular and intergranular bubbles and subdivided grains.

A restructuring phenomenon, with a subdivision of the grains (differences in grey contrast, indicated in red on Figure 47 –) is visible near the grain boundaries and near a big porosity (pink circle), as already previously observed. This highlights a misorientation of the grains in the areas of the grain boundaries.

Concerning the grain boundaries visible on Figure 47 –, it can be noticed that they are not continuously opened. Indeed, bubbles are present along them (in green on Figure 47 –) but do not constitute a continuous network.

A better vision of the peculiar shapes of the intragranular gas bubbles, as indicated in orange on Figure 47 –, is also possible with these images. Indeed, the cracks, as observed in blue in Figure 45, as well as round-shaped cavities with dendrites growing in some directions are also visible.

A deeper look into these observations was possible with the use of machine learning to perform a 3D reconstruction of the intra- and intergranular bubbles. The results can be seen in Figure 48.

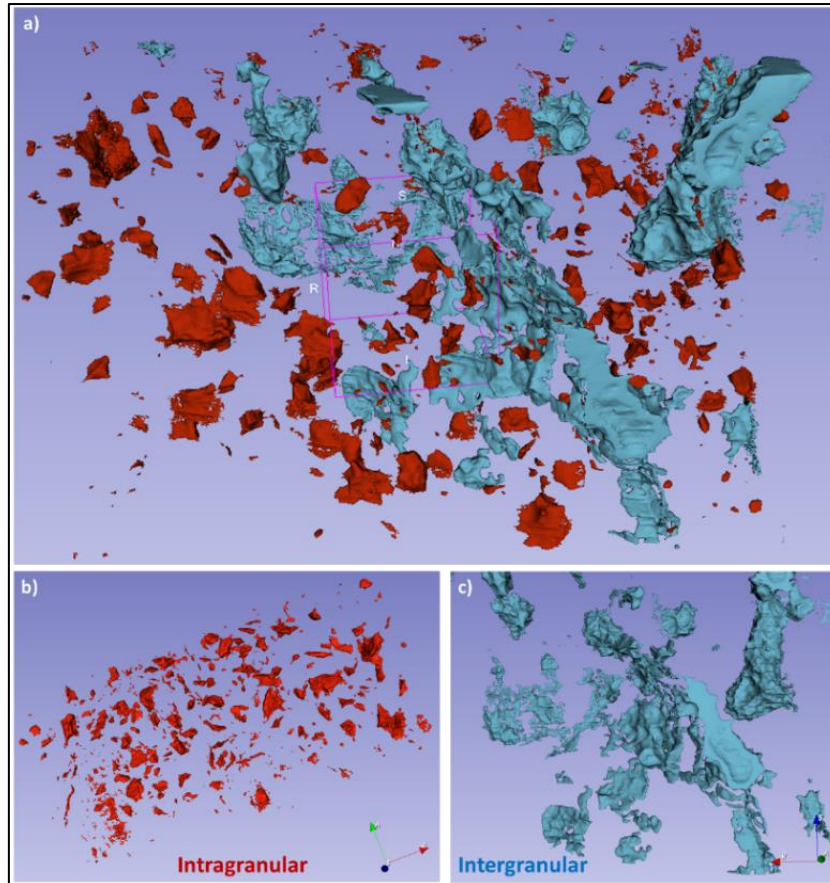


Figure 48 – 3D reconstruction of the (a) total porosity, (b) the intra- and (c) intergranular bubbles in the area studied at 0.2R.

As previously explained, when looking at the intergranular bubbles (Figure 48(c)), it can be seen that they do not constitute a continuous network, with some interconnections of bubbles in some areas but not on the whole intergranular porosity. Thus, the grain boundaries are not fully opened. In addition, as previously described, differences in orientation of the grain boundaries can be observed.

The 3D reconstruction of the intragranular bubbles (Figure 48(b)) reveals a chip shape for the bubbles identified as surface stripes in Figure 47 –, as well as their preferential orientations in the plane. In addition, the chip-shaped bubbles appear to be isolated, whereas more complex systems are interconnected. Zooms on two intragranular bubbles were performed and the results are presented in Figure 49 and Figure 50.

The 3D reconstruction of a surface crack presented in Figure 49 reveals the shape of a chip for this type of bubbles. It consists of a flat bubble with a small cavity in the middle of approximately 1.5 μm diameter and is rather flat, with a thickness of ~ 150 nm.

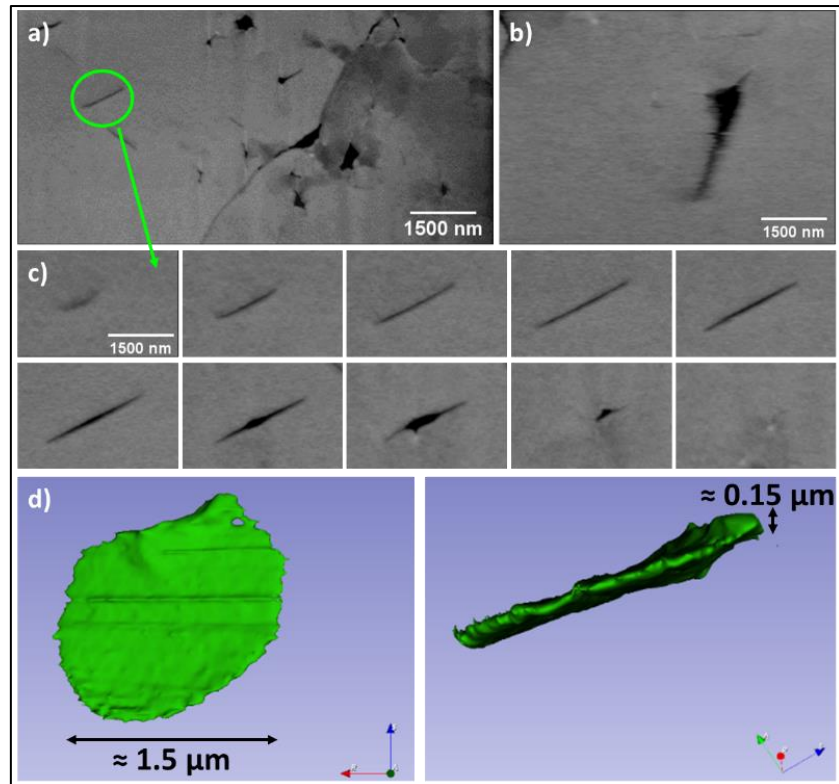


Figure 49 – (a) Front view of an intragranular bubble, (b) top view, (c) series of images used for the 3D reconstruction (1 image every 15 nm) and (d) 3D reconstruction of the pore.

The Figure 50 presents the 3D reconstruction of a network of intragranular bubbles. The interconnection of chip-shaped bubbles is observed here.

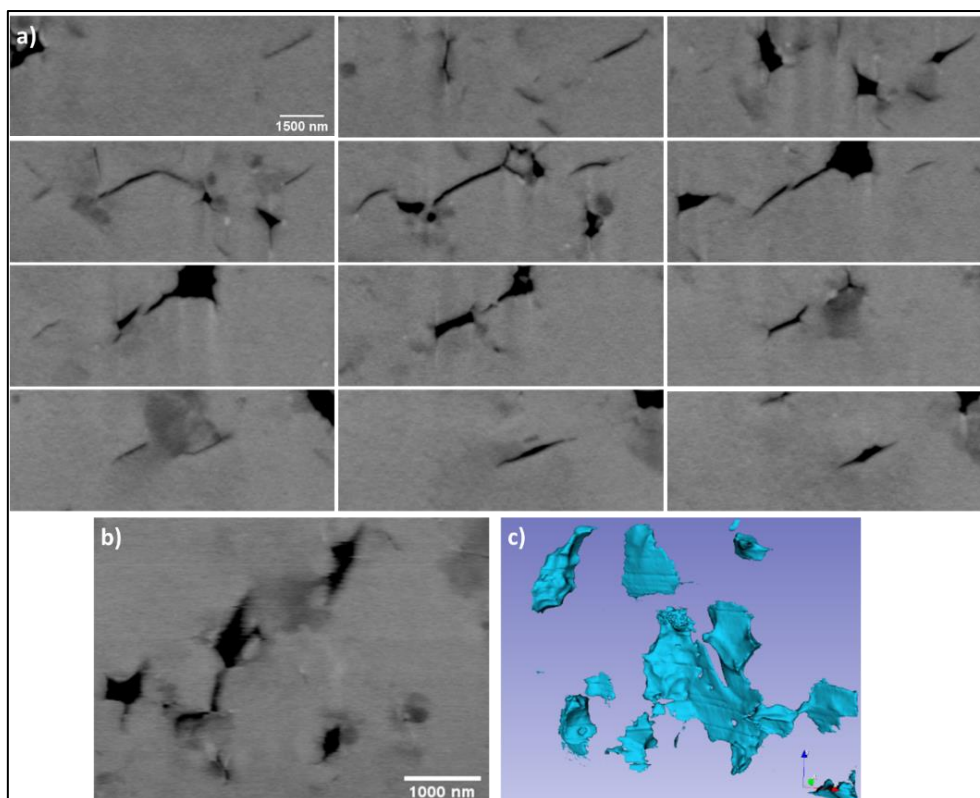


Figure 50 – (a) Front view of an intragranular bubble, series of images used for the 3D reconstruction (1 image every 15 nm) of the pore of interest, (b) top view and (c) 3D reconstruction of the pore.

5.4.2.2 0.8R

The area studied at 0.8R is a cube with images taken every 15 nm, resulting in overall 634 images. 592 of them were sorted out and used for this work. A refinement procedure was applied to the selected images to correct potential differences in position and lighting during the acquisition.

The Figure 51 presents several images, taken every 750 nm (one image out of 50) and follows the variation of the microstructure in depth in the material.

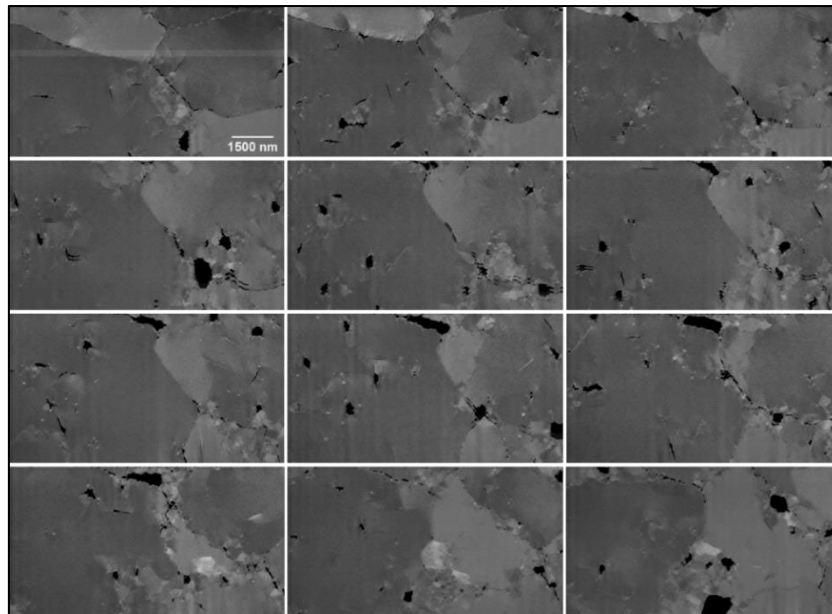


Figure 51 – Images at 0.8R extracted from a 3D acquisition (step of 750 nm between each image, one image out of 50).

An image extracted from the 3D acquisition is visible in details in Figure 52 –.

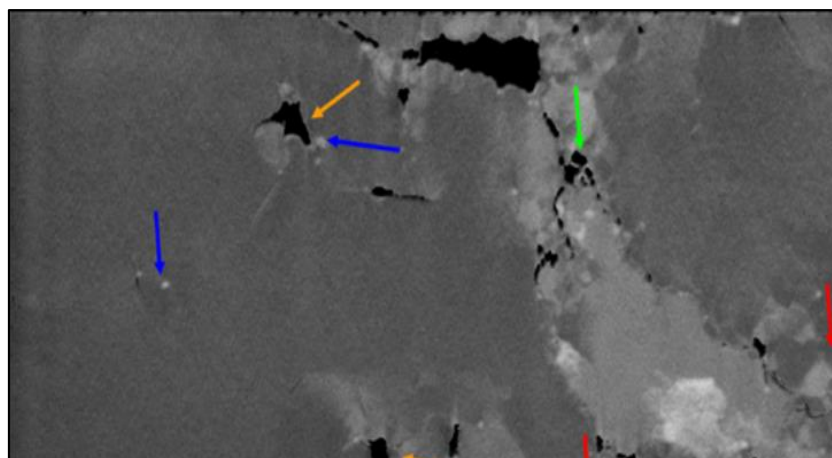


Figure 52 – SEM observation at 0.8R taken during a 3D acquisition, revealing the presence of precipitates, intragranular and intergranular bubbles and subdivided grains.

The same features already observed at 0.2R can be found here, such as the presence of metallic precipitates. In addition, a subdivision of the grains is occurring, with the appearance of small grains of different contrasts at the grain boundaries (indicated in red on Figure 52 –). Intragranular gas bubbles with a stripe shape on the analysed surface can also be observed, as well as bubbles of random shapes with dendrites growing on them. The discontinuity of the bubbles network at the grain boundaries is also visible on the figure.

A deeper look into these observations was possible with the use of machine learning to perform a 3D reconstruction of the intra- and intergranular bubbles (Figure 53).

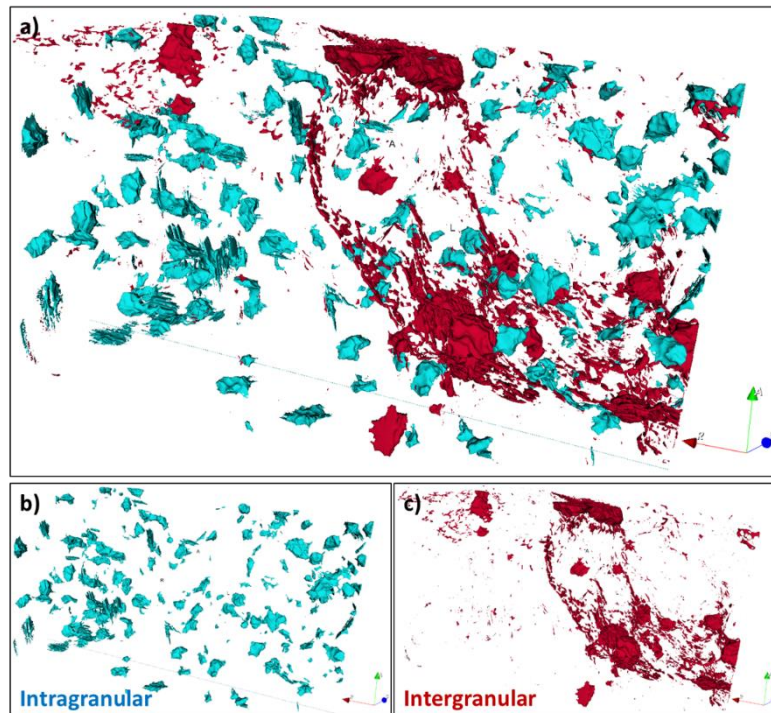


Figure 53 – 3D reconstruction of the (a) total porosity, (b) intra- and (c) intergranular bubbles in the area studied at 0.8R.

Concerning the intragranular bubbles, the presence of chip-shaped bubbles is observed, as it was already the case at 0.2R, as well as some more round-shape ones. However, differences can be noticed regarding the intergranular bubbles. Indeed, a bubbles network is identified, presenting a draping effect, with a concentration of bubbles in some areas. In addition, no clear opening of the grain boundaries is observed.

In order to better visualise the shape of the intragranular bubbles, zooms on three of them were performed and are presented in Figure 54 and Figure 55.

Different shapes of bubbles are revealed with this 3D reconstruction. The bubble in Figure 54 is constituted of a sphere, from which straight dendrites are growing in different oriented ways. The green compounds visible on this reconstruction correspond to metallic precipitates, visible in white on the images. Drape flat bubbles are presented on Figure 55, containing some holes. The last type of bubbles obtained by 3D reconstruction (Figure 55) contains a spherical part as well as a chip, interlinked within each other. The chip seems to present a preferred orientation and to precipitate on the edge of bubbles.

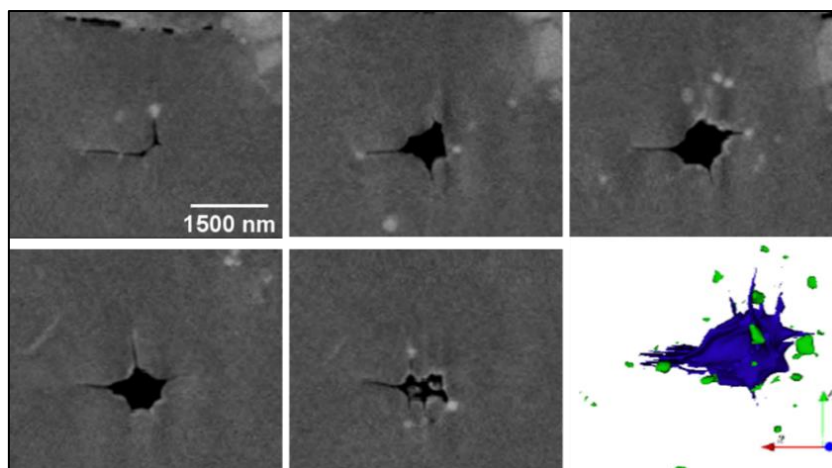


Figure 54 – Series of images and 3D reconstructions of one type of intragranular bubbles (sphere and dendrites, in blue) and precipitates of metal fission products (green).

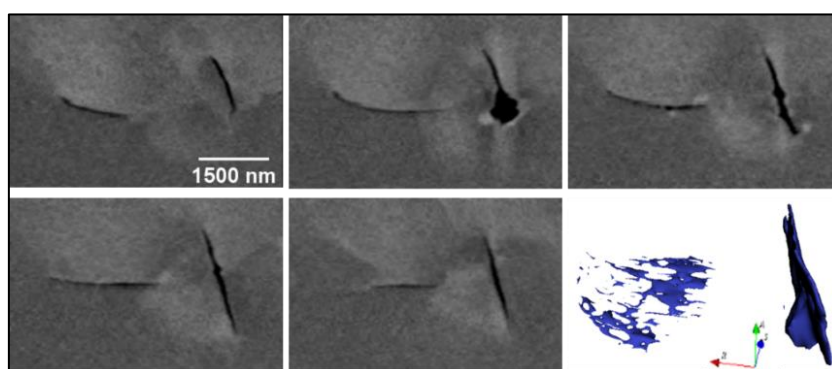


Figure 55 – Series of images and 3D reconstructions of two other types of intragranular bubbles (draped flat bubble and interlinked chip bubble).

5.4.2.3 Comparison 0.2R and 0.8R

When comparing the 3D results obtained at 0.2R and 0.8R, the same observations can be made. Indeed, similar microstructures are visible, with the presence of subdivided grains, located at the grain boundaries, indicating a restructuring phenomenon. In addition, intragranular bubbles are present at both locations, with similar types of shape. A difference can be found concerning the intergranular bubbles, as a draping effect is noticed at 0.8R. This is not the case at 0.2R, where the network of grain boundaries is less hemstitched. At 0.8R, it appears that the intergranular bubbles are smaller than the ones observed at 0.2R.

5.4.3 Samples preparation for TEM analyses

Two zones of interest were spotted in the same fragment at 0.8R for TEM analyses, both containing a grain boundary in the scanning area. The two TEM lamellae were obtained using the FIB mode see Figure 56).

5.5 TEM observations

The lamella referred as lamella 1 in Figure 56 is located in a restructured area, with the presence of various small grains and presents a crooked grain boundary. On the contrary, lamella 2 does not correspond to a restructured area and exhibits only two grains, with a straight grain boundary.

Unfortunately, due to a too large thickness in some areas originating from the preparation, only the thinner zones of the lamellae, located mainly close to the edge of the lamellae, could be studied by TEM.

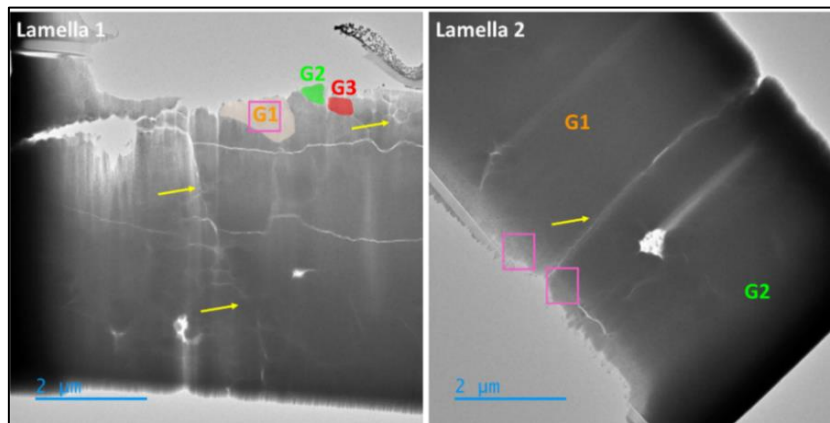


Figure 56 – TEM images of the two lamellae and positions of the grains and grain boundaries (yellow arrows). The pink rectangles correspond to the areas studied by diffraction.

5.5.1 Lamella 1 (restructured area)

5.5.1.1 Diffraction and TEM images

Electronic diffraction was performed on the grain 1 (see Figure 56, pink rectangle) by TEM. This technique allows gaining information on the crystal structure of the studied area at the nanometric scale. Examples of diffraction patterns are presented on Figure 57 for this grain, as well as the resulting stereographic representation.

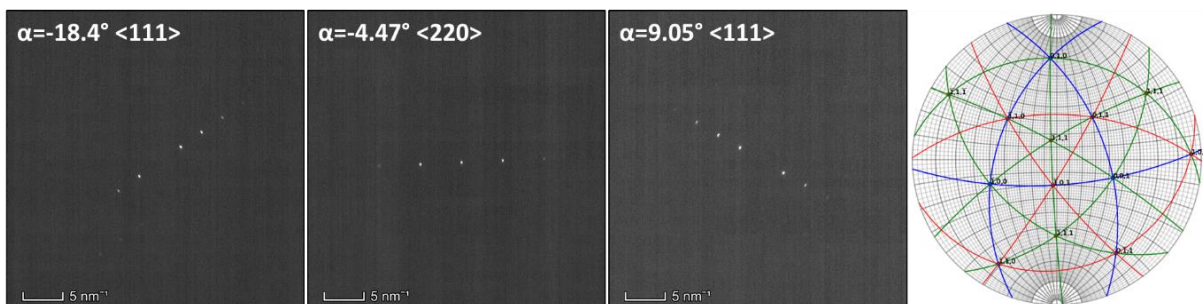


Figure 57 – Examples of diffraction patterns obtained for the grain G1 of lamella 1 and resulting stereographic representation.

The diffraction patterns exhibit diffraction spots corresponding to the interplanar spacing of the UO_2 lattice (face centred cubic crystal structure), highlighting that no U_3O_8 phase is present in this restructured area, confirming the optical and SEM observations. Indeed, if U_3O_8 would be present (under its orthorhombic form, i.e. $\alpha\text{-U}_3\text{O}_8$ at room temperature [6]), super-structures would be visible on the diffraction patterns as well as a shorter distance between the diffraction spots. This is due to the bigger lattice parameter of U_3O_8 ($a=4.136 \text{ \AA}$, $b=11.816 \text{ \AA}$, $c=6.822 \text{ \AA}$) compared to the one of UO_2 ($a=5.470 \text{ \AA}$).

The presence of bubbles was also studied by TEM, as it can be seen in Figure 58.

These images were obtained using the Fresnel contrast, consisting in varying slightly from the focus $f = 0$ in order to observe black or white fringes around the cavities. Indeed, in over-focused conditions, the bubble appears as a black spot surrounded by a white fringe, while in under-focused conditions, it appears as a white spot surrounded by a black fringe.

Two areas are given as an example in Figure 58, with the over-focused image on the left and the under-focused one on the right. Bubbles of various sizes can be observed on these images, ranging from less than 1 nm to few nanometers, as indicated by the yellow arrows. On the bottom images, a bubbles network is visible and indicated by the green arrows, which may be corresponding to a grain boundary. Indeed, on the upper images, a grain boundary is visible, indicated by the red arrows. With the contrast difference, it can be stated that this boundary is open and is constituted of a network of bubbles.

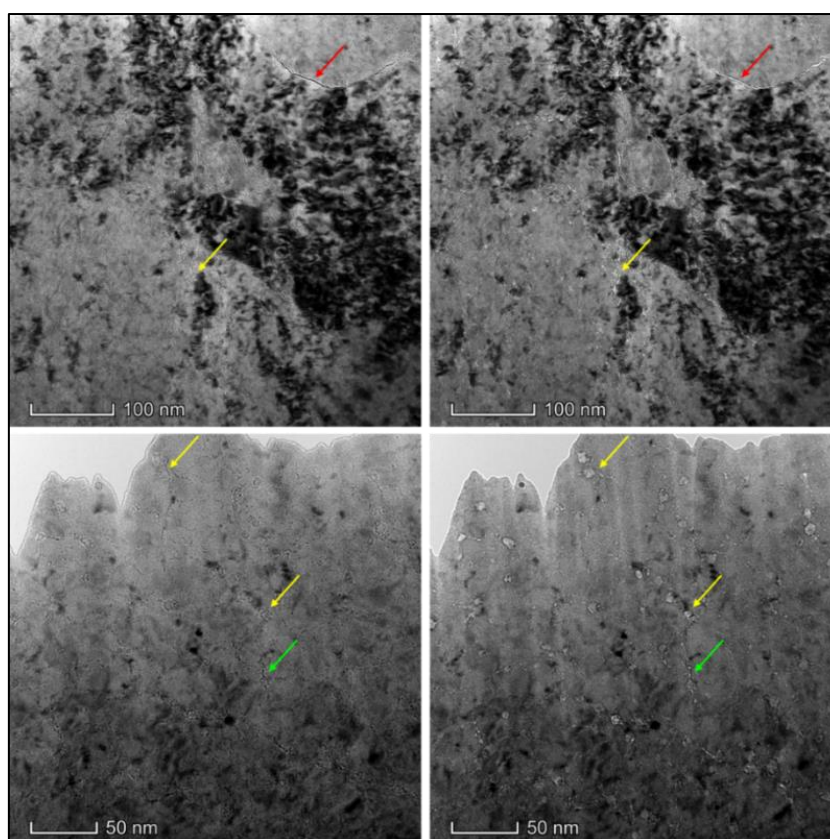


Figure 58 – TEM images of bubbles (examples indicated by yellow arrows), bubbles network (green arrow) and grain boundary (red arrow), in over-focused on the left ($f = +1 \mu\text{m}$) and under-focused condition on the right ($f = -1 \mu\text{m}$).

5.5.1.2 EDX analyses

Energy Dispersive X-ray analyses (EDX) were performed on various areas of the lamellae to determine the chemical elements present in these regions. An example of EDX maps is presented in Figure 59 with a studied zone located in the grain G1 (see Figure 56). The HAADF (High-Angle Annular Dark Field) image is also given, allowing seeing the different phases, precipitates or porosities with different chemical contrasts.

In this figure, the most common metallic precipitates for UO₂ fuels were observed, such as Mo, Ru, Rh, Pd and Tc. Agglomerates with higher concentrations of Mo, Pd and Ru are present, whereas the concentration of Rh and Tc is steady throughout the entire studied area. It can be noticed that uranium is less/not present in the agglomerates of metallic elements. A particularity of these maps is the presence of areas with higher concentrations of xenon, representative of the gaseous fission products. These areas correspond to bubbles, also visible on the HAADF image (red circles), and are located mainly close to the metallic precipitates. Large Xe bubbles can be observed on the Xe EDX maps (red circles), with a size of approximately 10 nm. In addition, similarities can be noticed when comparing the Xe and Mo EDX maps as these two elements are usually close to each other in UO₂ fuels.

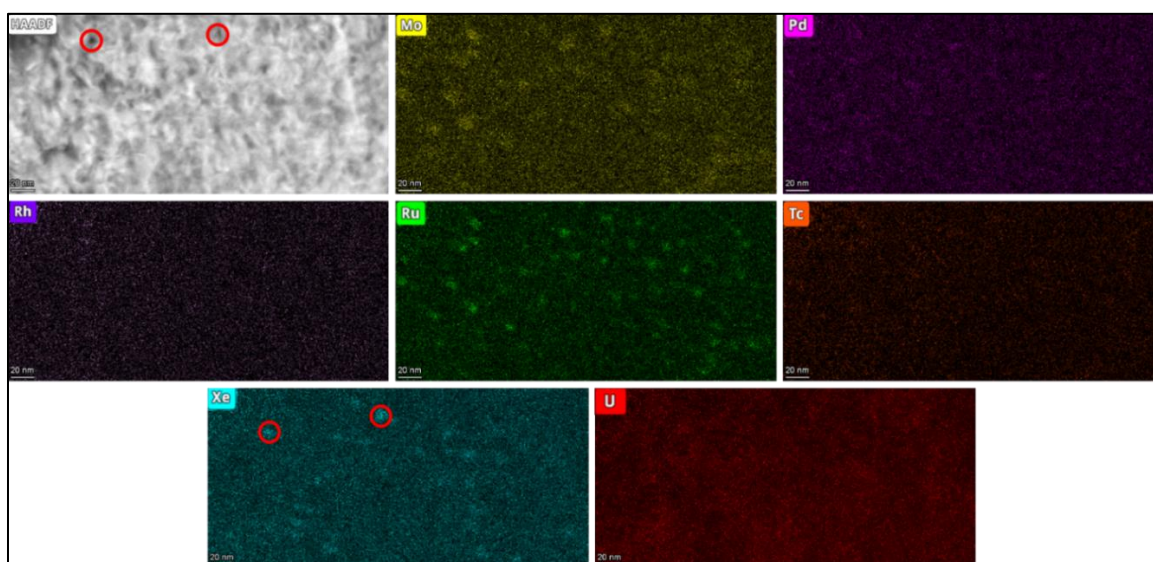


Figure 59 – EDX maps of Mo, Pd, Rh, Ru, Tc, Xe and U in the grain G1 of the restructured area (in at.%).

5.5.2 Lamella 2 (non-restructured area)

Another lamella was studied by TEM as it is representative of a non-restructured area, with only the presence of two grains and one grain boundary.

5.5.2.1 Diffraction and TEM images

Electronic diffraction was performed on the two grains (see positions of the scanned areas on Figure 56) and examples of the recorded patterns are presented in Figure 60, as well as the resulting stereographic representation.

This figure presents diffraction patterns obtained for the grains 1 and 2 for a specific tilt angle α , for which the most intense diffraction vector is along the $\langle 200 \rangle$ direction. Additional diffraction patterns (not illustrated here) were recorded at other tilt angles to build the corresponding stereographic representation of the grains. All the diffraction spots of the patterns of Figure 60 can be indexed with the lattice parameter of UO_2 in a face centred cubic crystal structure. The same observations as for the restructured area on lamella 1 can be made concerning the absence of U_3O_8 on the diffraction patterns.

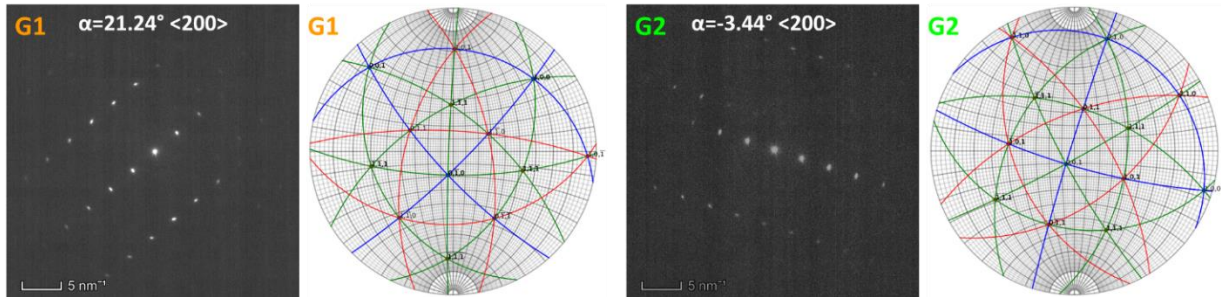


Figure 60 – Examples of diffraction patterns obtained for the grains G1 (up) and G2 (bottom) and resulting stereographic representations.

The presence of bubbles was also studied by TEM in the grain 1 and grain 2, as it can be seen in Figure 61.

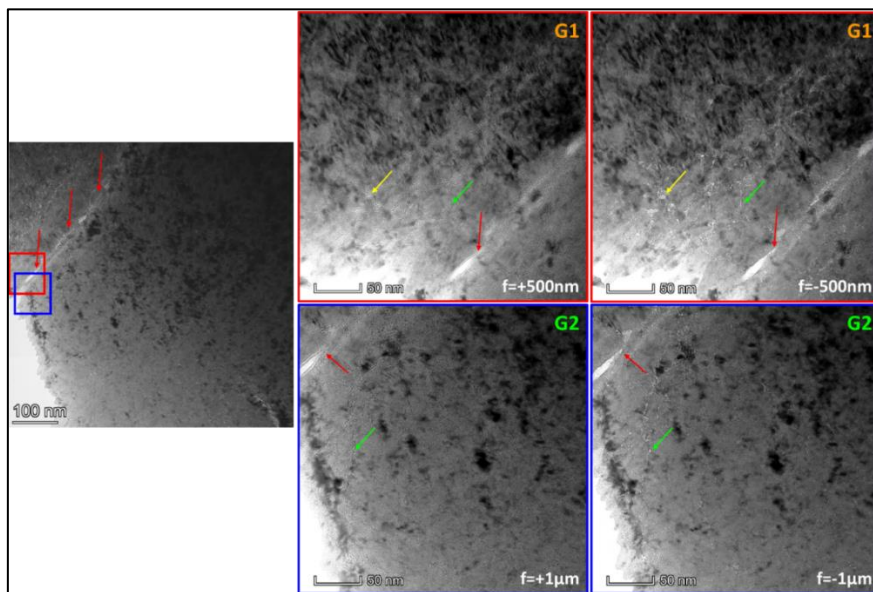


Figure 61 – TEM images of bubbles (examples indicated by yellow arrows), bubbles network (green arrow) and grain boundary (red arrow), for grains G1 and G2 in over-focused and under-focused conditions.

Bubbles of various sizes can be observed on these images, ranging from less than 1 nm to few nanometers, as indicated by the yellow arrows. Red arrows indicate the grain boundary. As it can be seen from the differences in the over- and under-focused conditions, this grain boundary is constituted by a network of bubbles of different sizes, evidencing an open grain boundary. Bubbles networks are

also visible and indicated by the green arrows in Figure 61. These networks appear to originate from the grain boundary before propagating throughout the grains.

5.5.2.2 EDX analyses

EDX analyses were performed close to the grain boundary, as it can be seen on Figure 62.

In this figure, the most common metallic precipitates for UO₂ fuels were observed, such as Mo, Ru, Rh, Pd and Tc. In this region, no xenon was present or in too low quantity to be detected.

As it can be seen, precipitates with higher concentrations of these metallic elements are present. It can be noticed that uranium and oxygen are less/not present in the agglomerates of metallic elements. These maps reveal thus the presence of metallic precipitates at the grain boundary.

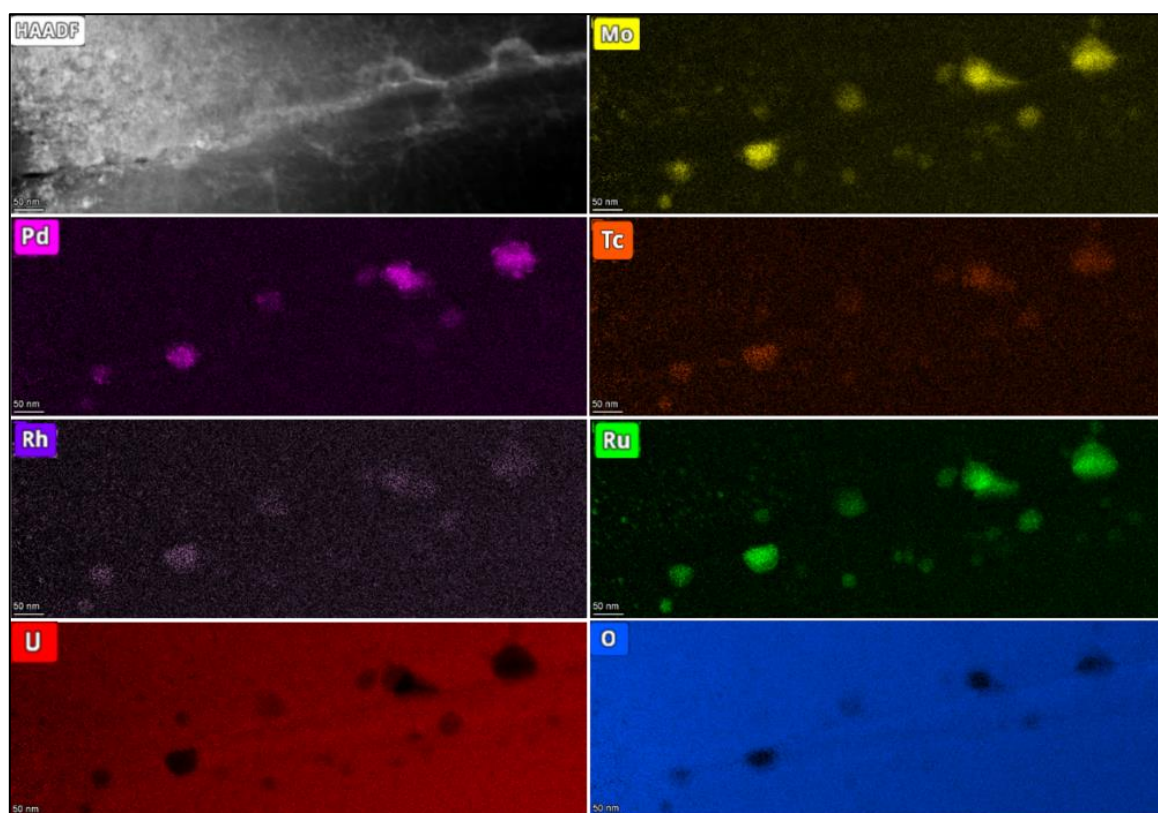


Figure 62 – EDX maps of Mo, Pd, Tc, Rh, Ru, U and O at the grain boundary in a non-restructured area (in at.%).

Another area of the non-restructured lamella was studied by EDX, corresponding to a zone with several cracks in the grain 2. The results are presented in Figure 63.

Dislocations can be seen on the HAADF image, with networks of veins visible in lighter contrast. The image also reveals the presence of precipitates, indicated by the round-shaped light contrasts. Metallic precipitates of Mo, Pd, Ru, Tc and Rh can be observed on the EDX maps, with few or no oxygen present in them, depending on the precipitate. When looking at the oxygen and uranium maps, two different behaviours can be noticed. Indeed, on Figure 63, for the crack located on the left part of the image (vertical crack), an increase in the oxygen concentration is noticed, while a decrease of the uranium concentration occurs. On the contrary, for the crack on the right (horizontal crack), an increase in the

uranium concentration is observed, associated to a decrease of the oxygen concentration. Apart from these two cracks and the precipitates, the uranium and oxygen concentrations are homogeneously distributed within the scanned area.

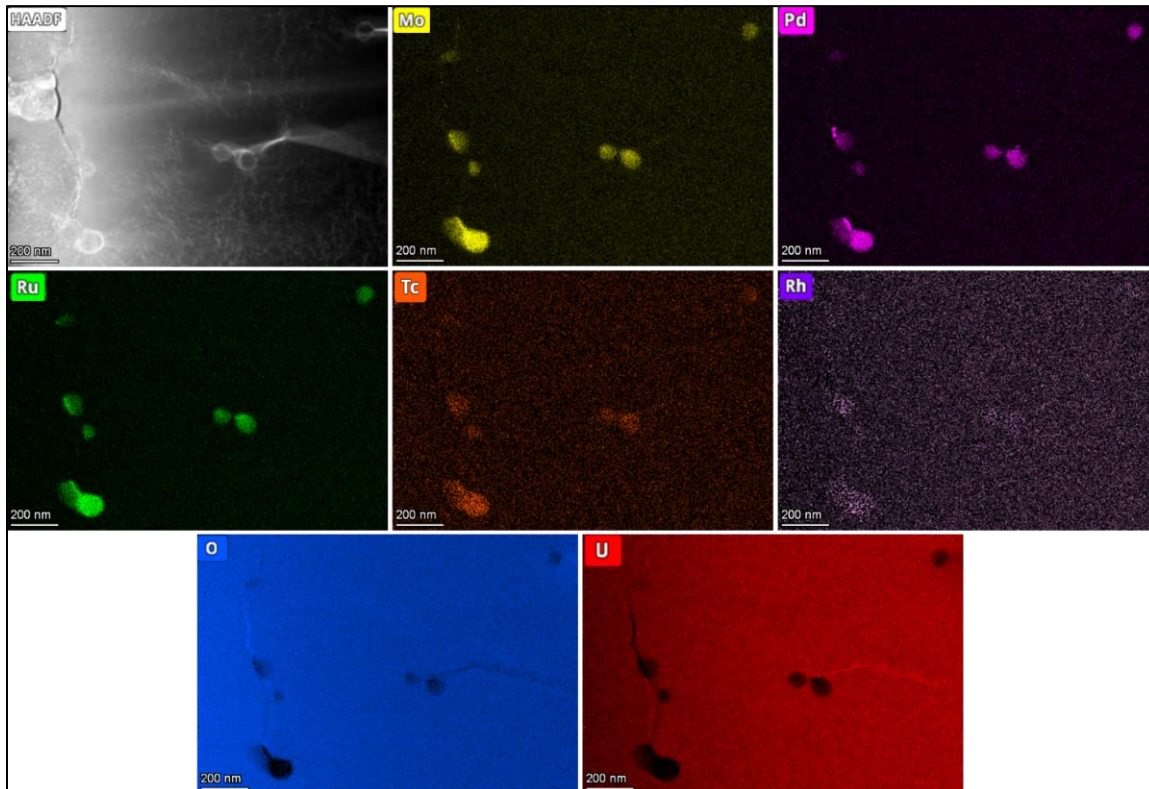


Figure 63 – EDX maps of Mo, Pd, Ru, Tc, Rh, O and U at cracks in a non-restructured area (in at.%).

5.5.3 Comparison between restructured and non-restructured areas

Electron diffraction performed by TEM revealed the presence of a UO_2 crystal structure for both lamellae, independently of the grains studied. Differences in orientation of the grains were also observed with this technique. The same features were noticed on TEM images for the two areas, i.e. dislocation loops, bubbles and precipitates. The presence of open grain boundaries and bubbles networks was evidenced in both lamellae. EDX maps revealed the most common metallic elements of spent UO_2 fuel (Mo, Pd, Ru, Rh and Tc), agglomerated in some areas as precipitates. These precipitates are mainly located close to porosities, grain boundaries, restructured areas and cracks. The main difference between the two areas lies in the presence of xenon close to the metallic precipitates in the restructured area, whereas it was not observed/detected in the non-restructured area. In both cases, no U_3O_8 phase was evidenced in the fuel.

5.6 Conclusion

Within the framework of a research project in the tripartite institute gathering EDF, CEA and Framatome, oxidation tests were performed under air at 200 °C on sections of UO_x and MO_x fuel with Zy-4 or M5 claddings for 12,900 to 13,640 hours. A rupture of the Zy-4 cladding occurred between 8,000 hours and the end of the experiment in most cases. The follow-up of the weight change recorded during the oxidation tests did not suggest the formation of a U_3O_8 phase, which could have explained a swelling of

the fuel and thus the rupture. In order to study this phenomenon, several characterisations, such as optical observations, SEM or TEM, were performed for example here on a UO_x section with Zy-4 cladding, presenting a rupture of the cladding.

The metallographic and SEM observations revealed the presence of radial and circumferential cracks in the fuel, located between 0.70R and the pellet/cladding interface. Optical observations of the cladding indicated the presence of radial cracks in it. Small pieces of fuel attached to the cladding were seen, as well as layers of internal and external zirconia. The typical microstructure of the HBS was observed at the periphery of the pellet. This feature is visible along the whole pellet radius, with this subdivision occurring mainly at the grain boundaries. Inter- and intragranular bubbles of different sizes and shapes (oval, stripes, round with dendrites...) were also visible along the whole pellet radius, as well as grain boundaries. The opening of the grain boundaries within the fuel were also noticed, with the presence of bubbles inside them. 3D imaging was performed at 0.2 and 0.8R and similar results were obtained for the two positions. The grain boundaries were found to contain bubbles but not forming a continuous network. 3D reconstruction allowed extracting the shapes of the intragranular bubbles. Isolated chip-shaped bubbles and more complex networks of bubbles were found at 0.2R, whereas spheres, draped bubbles or an interconnection of spherical and chip objects were observed at 0.8R. The main difference between the two positions concerns the intergranular bubbles. Indeed, at 0.8R, a draped effect was obtained with the 3D reconstruction, showing some continuous networks. At 0.2 and 0.8R, it appeared that the bubbles were strongly oriented in preferential orientations, which could not be determined. The presence of U₃O₈ within the fuel was not evidenced with these observations.

Two lamellae prepared by FIB-SEM were studied by TEM, both at 0.8R but one corresponding to a restructured area with several grains and the other representative of a non-restructured area with only two grains. Electron diffraction confirmed the crystal structure of UO₂ for the grains contained in both lamellae, rejecting the hypothesis of a U₃O₈ phase. Dislocation loops and bubbles were evidenced for both lamellae. Networks of bubbles were also observed, mainly at the grain boundaries. Metallic precipitates of Mo, Pd, Ru, Rh and Tc were found in both areas, mainly located close to porosities, grain boundaries, restructured areas and cracks. The presence of xenon bubbles at the proximity of the precipitates was noticed only in the restructured area.

This work evidenced that no U₃O₈ phase was formed during the oxidation test but an opening of the grain boundaries with the presence of network bubbles inside them was observed. This feature could explain the rupture of the cladding, by a release of the fission gases through the grain boundaries, causing constraints to the cladding.

This study helps understanding the behaviour of nuclear fuel rods, both in nominal or defective conditions, under interim storage conditions. Further work would be needed to understand this phenomenon and comparison with the initial rod without oxidation test and irradiation history could help understanding the different mechanisms.

5.7 References

- [1]L. Desgranges *et al.*, 'Bilan des expériences d'oxydation à 200 °C sous air menées au LAMA sur des fragments de combustible irradié', NT DEC/SA3C/056, 2004, Personal Communication.
- [2]L. Desgranges, M. P. Ferroud-Plattet, H. Giacalone, I. Aubrun, and J. M. Untrau, 'Bilan des expériences d'oxydation ménagées à 200 °C menées au LECA et au LAMA dans le cadre du programme PRECCI', NT SA3C/L2EC/006, 2007, Personal Communication.
- [3]A. Fournet *et al.*, 'Expérimentations d'oxydation à 200 °C sous air sur des fragments et tronçons de combustible irradié UOx et MOx', NT DEC/SA3C/087, 2005, Personal Communication.
- [4]L. Brunaud, L. Fayette, C. Pozo, and H. Giacalone, 'Bilan des expériences d'oxydation ménagée à 200 °C menées au LECA entre 2008 et 2012', NT CEA/DEN/CAD/DEC/SA3C/013, 2012, Personal Communication.
- [5]L. Fayette, X. Pujol, and P. Delion, 'Expérience "oxydation ménagée": examens destructifs (métallographie et MEB) de tronçons UOx gainés Zy-4 rompus après essai de chauffe à 200 °C sous air pendant une durée cumulée de 13500 heures', NT CEA/DEN/CAD/DEC/SA3C/012, 2014, Personal Communication.
- [6]B. O. Loopstra, 'Neutron diffraction investigation of U₃O₈', *J. Phys.*, vol. 25, no. 5, pp. 429–430, 1964, doi: 10.1051/jphys:01964002505042900.

6. Conclusions

This report provides a comprehensive analysis of potential accident scenarios in interim storage and packaging facilities for spent nuclear fuel (SNF), along with an assessment of fuel performance under these conditions. The findings and methodologies presented here are crucial for enhancing the safety and reliability of SNF storage systems.

6.1 Key findings

The analysis identified various potential accidents, including dry storage system tip-over, drops, fire, explosion, and flooding. Among these, the tip-over of the dry storage cask was highlighted as the most critical scenario, posing significant risks to both the dry storage system (DSS) and the SNF.

The mechanical performance of Pressurised Water Reactor (PWR) spent fuel assemblies was studied using finite element analysis, focusing on their behaviour under accident conditions. The transition from small-scale rodlet models to full-scale assemblies emphasised the importance of computational efficiency. Failure criteria were derived based on rod plastic strain, and larger-scale models were developed to assess structural response under flexural loading conditions.

A stochastic methodology integrating FRAPCON-xt, HYDCLAD, and DAKOTA was developed to estimate the probability of fuel rod failure. This approach, tested on a hypothetical drop accident scenario, demonstrated significant safety margins with zero failure probability. The methodology underscored the need for further research in modelling irradiation damage recovery to enhance the robustness of safety assessments.

Oxidation studies conducted at 200°C on irradiated UO_x and MOX fuel sections with Zy-4 and M5 claddings provided critical insights into cladding rupture mechanisms. A possible mechanism for the cladding failure was proposed with internal stress from gas release and swelling, rather than the formation of U₃O₈. Detailed analyses using metallography, SEM, and TEM revealed the formation of radial and circumferential cracks and gas accumulation at grain boundaries, offering a deeper understanding of these failure mechanisms.

6.2 Recommendations and future work

To improve the safety of SNF storage systems, it is recommended to incorporate probabilistic risk assessments and detailed accident scenario analyses into the design and certification processes. Specific safety improvements should be implemented based on identified critical parameters, such as enhancing the structural integrity of storage casks to mitigate tip-over risks. Additionally, continuous monitoring and data collection programs should be established to refine models and methodologies, with a particular focus on irradiation damage recovery and long-term oxidation behaviour.

Future efforts should aim to expand the scope of accident scenarios and incorporate advanced modelling techniques. Collaboration with industry partners and regulatory bodies will be essential to integrate these methods into standard safety practices and ensure the continued safety of SNF storage and transport systems.